(12)

RADC-TR-77-338
In-house Report
October 1977

SEEK IGLOO RADAR CLUTTER STUDY

William L. Simkins
Vincent C. Vannicola
James P. Ryan

Approved for public release; distribution unlimited.

ROME AIR DEVELOPMENT CENTER
Air Force Systems Command
Griffiss Air Force Base, New York 13441

This report has been reviewed by the Office of Information, RADC, and approved for release to the National Technical Information Service (NTIS). At NTIS, it will be releasable to the general public, including foreign nations.

This report has been approved for publication.

APPROVED: Frank J Rehm

FRANK J. REHM
Chief, Technology Branch
Surveillance Division

APPROVED: Joseph L Ryerson

JOSEPH L. RYERSON
Technical Director
Surveillance Division

FOR THE COMMANDER: John P. Huss

JOHN P. HUSS
Acting Chief
Plans Office

If your address has changed, if you wish to be removed from the RADC mailing list, or if the addressee is no longer employed by your organization, please notify RADC (OCTS) Griffiss AFB NY 13441. This will assist us in maintaining a current mailing list.

Do not return this copy. Retain or destroy.

UNCLASSIFIED

SECURITY CLASSIFICATION OF THIS PAGE (When Data Entered)

REPORT DOCUMENTATION PAGE

READ INSTRUCTIONS BEFORE COMPLETING FORM

1. REPORT NUMBER: RADC-TR-77-338	2. GOVT ACCESSION NO.
3. RECIPIENT'S CATALOG NUMBER	
4. TITLE (and Subtitle): SEEK IGLOO RADAR CLUTTER STUDY	5. TYPE OF REPORT & PERIOD COVERED: In-house; 2 Aug-17 Sept 76
6. PERFORMING ORG. REPORT NUMBER: N/A	
7. AUTHOR(s): William L. Simkins, Vincent C. Vannicola, James P. Ryan	8. CONTRACT OR GRANT NUMBER(s): N/A
9. PERFORMING ORGANIZATION NAME AND ADDRESS: Rome Air Development Center (OCTS), Griffiss AFB NY 13441	10. PROGRAM ELEMENT, PROJECT, TASK AREA & WORK UNIT NUMBERS: 12326F, 968RIGLO
11. CONTROLLING OFFICE NAME AND ADDRESS: Same	12. REPORT DATE: Oct 1977
	13. NUMBER OF PAGES: 132
14. MONITORING AGENCY NAME & ADDRESS (if different from Controlling Office): Same	15. SECURITY CLASS. (of this report): UNCLASSIFIED
	15a. DECLASSIFICATION/DOWNGRADING SCHEDULE: N/A

16. DISTRIBUTION STATEMENT (of this Report)

Approved for public release; distribution unlimited.

17. DISTRIBUTION STATEMENT (of the abstract entered in Block 20, if different from Report)

Same

18. SUPPLEMENTARY NOTES

None

19. KEY WORDS (Continue on reverse side if necessary and identify by block number)

Clutter
Ground Clutter
Sea Clutter
Weather Clutter
Angels

20. ABSTRACT (Continue on reverse side if necessary and identify by block number)

This report presents the procedures and results of a clutter measurement program conducted in Alaska during the summer of 1976. Both amplitude and spectral density functions were modeled from the data taken from land, sea, weather, and other forms of clutter. Sectors over which clutter was measured varied in size and in roughness, and, consequently, gave rise to density functions, ranging from log-normal, where major shadowing did not occur, to heavily contaminated-normal with large regions of shadowing. Reflectivity for 50 to 84

(over)

DD FORM 1 JAN 73 1473 EDITION OF 1 NOV 65 IS OBSOLETE

UNCLASSIFIED

SECURITY CLASSIFICATION OF THIS PAGE (When Data Entered)

20.

percentile characterizing the worst case terrain features are also presented.

ACKNOWLEDGMENT

It is difficult to credit appropriately the numerous contributors to the success of this effort. Those who especially merit acknowledgment are the data collection team from RADC, ESD and 4754th RADES (ADC), Mr. Floyd Myers of the 4754th RADES (ADC), Mr. Ralph George of AAC/LGMK, the search radar personnel at the AAC sites, Major David B. Johnson and Captain William J. Kaveny from RADC/WE and the innumerable members of the RADC staff who provided assistance and encouragement.

TABLE OF CONTENTS

LIST OF FIGURES

LIST OF TABLES

LIST OF SPECTRUM ANALYZER PHOTOGRAPHS

LIST OF SPECTRUM ANALYZER PHOTOGRAPHS (CONTINUED)

I. INTRODUCTION:

This report presents the clutter information obtained during the clutter measurement task performed in support of the SEEK IGLOO Radar Development Program. The SEEK IGLOO Program is directed toward the implementation of minimally-attended radar systems at the Alaskan Air Command surveillance radar sites. The successful implementation of unattended radars would significantly reduce the high cost of maintaining personnel at each site. However, such systems require automatic detection schemes with low false alarm rates and moderate probabilities of detection in all clutter environments. Therefore, accurate knowledge of the clutter environment is necessary to obtain a properly designed radar.

The primary purpose of the clutter measurement task was to determine the worst case amplitude statistics and spectra of land clutter. Radar backscatter was measured from range-azimuth locations characterized by three terrain types: valleys (muskeg), hills and mountains. Both high-sited and low-sited radars were used in the measurement. Other measurements performed include sea clutter amplitude and spectra, weather clutter spectra, and angel spectra.

This report begins with a background discussion on the measurement team composition and the general procedure at each site. The measurement technique and equipment is discussed in Section III followed by the presentation and discussion of the measured amplitude clutter in Section IV and spectral data in Section V.

II. BACKGROUND:

The measurement team was comprised of individuals from the Electronic Systems Division (ESD), 4754th Radar Evaluation Squadron (RADES), Rome Air Development Center (RADC), and Alaskan Air Command (AAC). The functions and members of each organization are given in Figure 1.

The clutter data was collected at five (5) selected AAC radar sites during the period 2 August through 17 September 1976. These sites were selected for their severe or unusual clutter environments. Table I gives the location of the sites and the reason for selection.

The schedule at each site is given in Figure 2. During the first three days, the RADES and AAC teams calibrated the radar. This procedure was performed to assure properly operating equipment prior to the measurements and to provide a check of the critical antenna electrical tilt and other system parameters for use in the measurement analysis. These calibrations typically included the following:

Antenna System

Mechanical Checks
Solar Measurements (except for Tatalina, Cape Newenham)

Transmitter System

PRF
Pulse Shaping
Power Output
Frequency

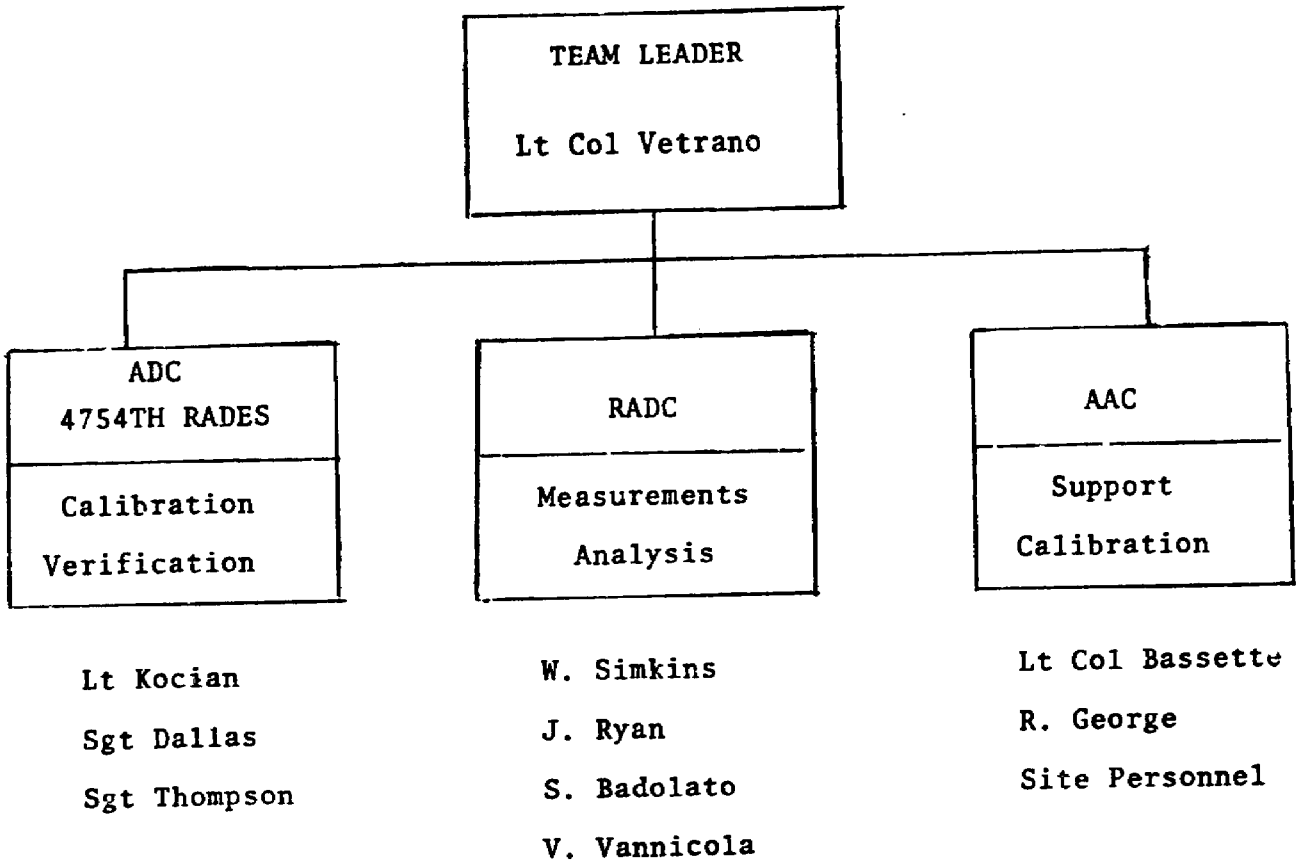

FIGURE 1: Team Composition

TABLE I: Measurement Sites

SITE	DATE	TOPOGRAPHY	SELECTION REASON
Fort Yukon	5 - 13 Aug	Muskeg Mountains Hills	Angels
Indian Mt.	13 - 20 Aug	Mountainous Muskeg Hills	Heavy Ground Clutter
Tatalina	20 - 27 Aug	Muskeg Hills Mountainous	Heavy Ground Clutter
Cape Newenham	1 - 9 Sept	Hills Bering Sea	Sea Clutter Anomalous Propagation
Cold Bay	10 - 16 Sept	Volcanic Mts Sea	Sea Clutter Heavy Clutter Anomalous Propagation

DAYS	ADC - AAC	RADC
1 Thru 3	Antenna Mechanical Solar Checks Receiver Checks Transmitter Checks PPI and Misc. Checks	Equipment Set Up and Calibration Site Familiarization Clutter Observation
4 Thru 7	Assistance in Measurements	PPI Clutter Photos Clutter Amplitude Measurements Spectral Measurements Time Period - 1800 - 0600 Downtime - 9 to 12 hours Pack Equipment

FIGURE 2: Schedule

Receiver (Normal and MTI)

Bandwidths
Center Frequencies
MTI System
Video Levels

Plan Position Indicator (PPI)

Focus and Stability
Azimuth Orientation
Range Mark Accuracy

In addition, the RF losses between the receiver/transmitter to the antenna feed and the mixer-preamplifier dynamic range were measured.

Various measurements were performed during the last four days. These included PPI clutter photos, amplitude cumulative distribution measurements, and spectral measurements. Due to operational considerations, nearly all measurements were performed between 1800 - 0600 local time and the operational downtime allowed for spectral measurements was typically 9 to 12 hours.

III. MEASUREMENT EQUIPMENT AND METHODOLOGY:

A. Amplitude Measurements:

The clutter parameters measured were the effective radar cross-section σ_c' and the effective coefficient of reflection σ_o' as defined in Table II. The term "effective" is used because the measured parameter contains an unknown propagation factor F which was not factored out. The equipment used in obtaining the amplitude cumulative distribution function of these parameters was an implementation of the radar range equation. Briefly, the equipment had the following features:

1. R^{-4} (or R^{-3}) range normalizing thresholds were available.
2. σ_c' (or σ_o') reference could be related to the threshold using the radar parameters.
3. σ_c' (or σ_o') amplitude profiles could be obtained by inserting attenuation.
4. The range-azimuth measurement interval was programmable.
5. Threshold crossings were sampled at an interval equal to or greater than once per pulse width.
6. A sample pulse width of 100 NS was used to increase independence between adjacent samples.
7. Threshold crossings were counted using an electronic counter.
8. A threshold output for PPI display was available for pictures.

TABLE II: Definition of σ_c' and σ_o'

$$\sigma_c' \triangleq \sigma_c F^4 = \frac{P_r R^4 (4\pi)^3 L_s}{P_t G_t G_R \lambda^2} \quad (1)$$

$$\sigma_o' \triangleq \frac{\sigma_c'}{A} = \frac{\sigma_c F^4}{A} = \left[\frac{P_r R^3 L_s (4\pi)^3}{P_t G_t G_R \lambda^2}\right]\left[\frac{\sqrt{2}}{\frac{c\tau}{2} \sin\theta_\beta \sec \phi_g}\right] \quad (2)$$

where σ_c' = Effective Radar cross-section

σ_c = Radar cross-section

F = Propagation factor

P_r = Received power at input to receiver

P_t = Transmitter peak power

R = Range

G_t = Gain of transmitting antenna

G_r = Gain of receiving antenna

λ = Wavelength

L_s = System RF loss = $L_T L_R L_p L_{RA}$

σ_o' = Effective coefficient of reflection

σ_o = Coefficient of reflection

A = Resolution area = $R \left(\frac{c\tau}{2}\right) \sin\theta_\beta \sec\phi_g \left(\frac{1}{\sqrt{2}}\right)$

c = Speed of propagation

τ = Pulse width

θ_β = Antenna beamwidth (One Way)

L_T = Transmitter RF loss

L_R = Receiver RF loss

L_p = Propagation loss

L_{RA} = Radome loss

9. One measurement per antenna scan of one area could be taken.

A generalized block diagram of the clutter amplitude analyzer (CAA) is shown in Figure 3. A block diagram of the threshold generator and comparator is given in Figure 4. The RF log amplifier had a dynamic range of over 80 dB with a log accuracy within $\pm$ 1 dB. The DC log amplifier had a dynamic range over 80 dB with a maximum log conformity error of 1%. The linear ramp had a peak deviation from linear of less than 5% over the range used. By varying the slope a, gain γ, DC bias B, and time delay Z, the threshold was adjusted to give the desired threshold-versus-time curve such as those shown in Figure 5. The reference parameters $\sigma'_{c\ ref}$ and $\sigma'_{o\ ref}$ were related to the thresholds by the equations derived in Appendix A.

The methodology used was straightforward. Areas of strong clutter were located on the PPI and correlated with terrain type using topographic maps. Regions with range and azimuth extents within the terrain type were outlined and converted into the programmable parameters of the measurement equipment (Figure 6). Received signals were amplified and compared to the threshold. Since the threshold represents a constant clutter parameter value for the given radar parameters, those signals exceeding the threshold represent regions with a higher clutter parameter value. The threshold comparator output was then sampled at a rate of once per

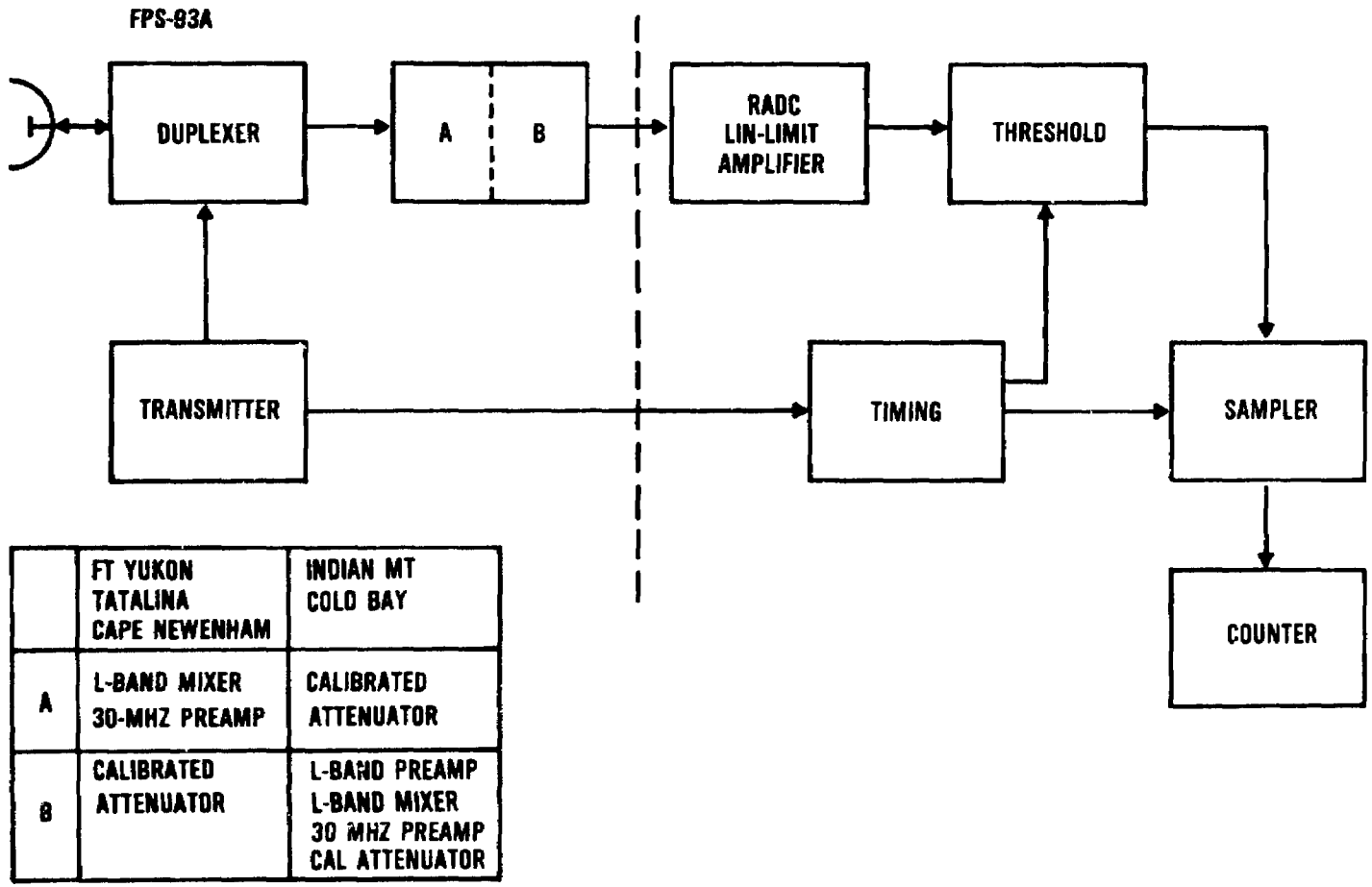

	FT YUKON TATALINA CAPE NEWENHAM	INDIAN MT COLD BAY
A	L-BAND MIXER 30-MHZ PREAMP	CALIBRATED ATTENUATOR
B	CALIBRATED ATTENUATOR	L-BAND PREAMP L-BAND MIXER 30 MHZ PREAMP CAL ATTENUATOR

FIGURE 3: Block Diagram of CAA Interface with FPS-93A

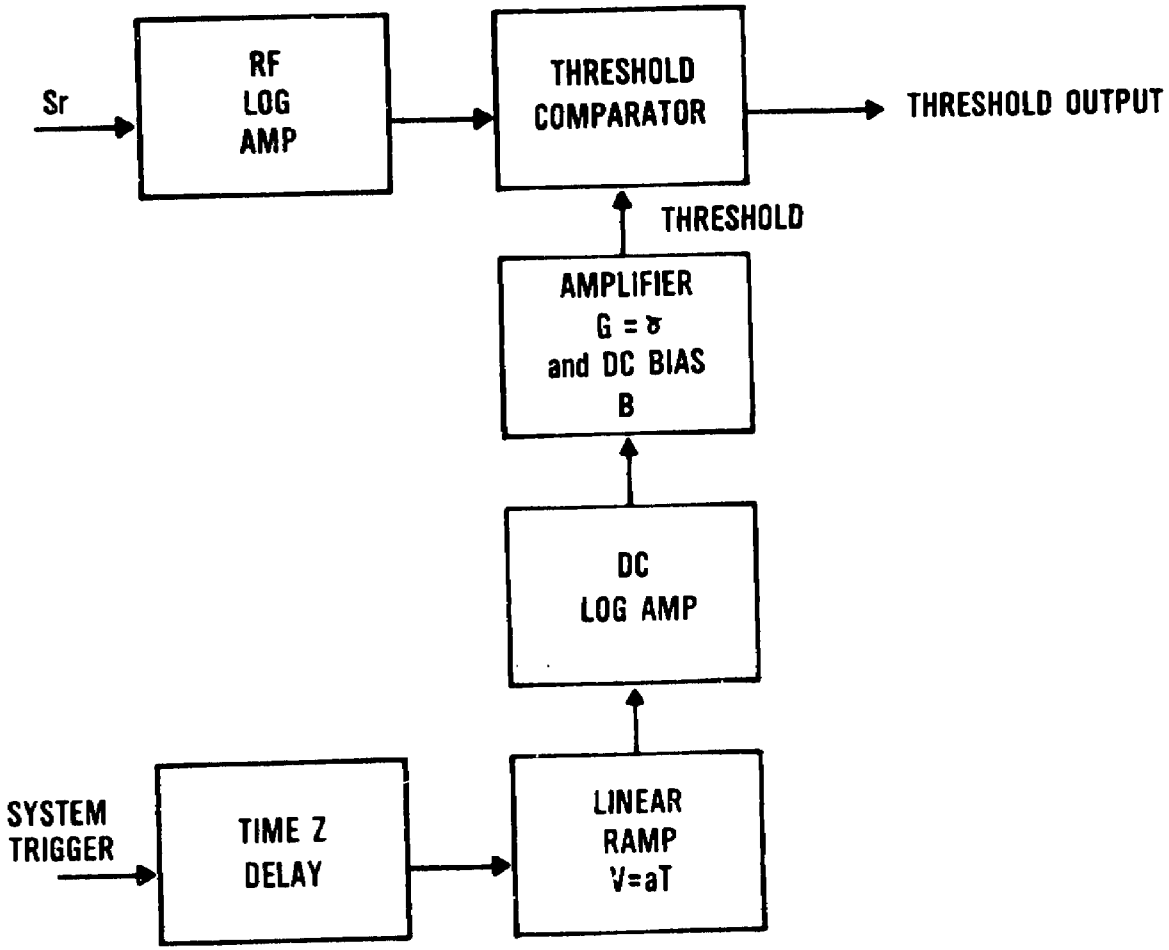

FIGURE 4: Threshold Generator and Comparator

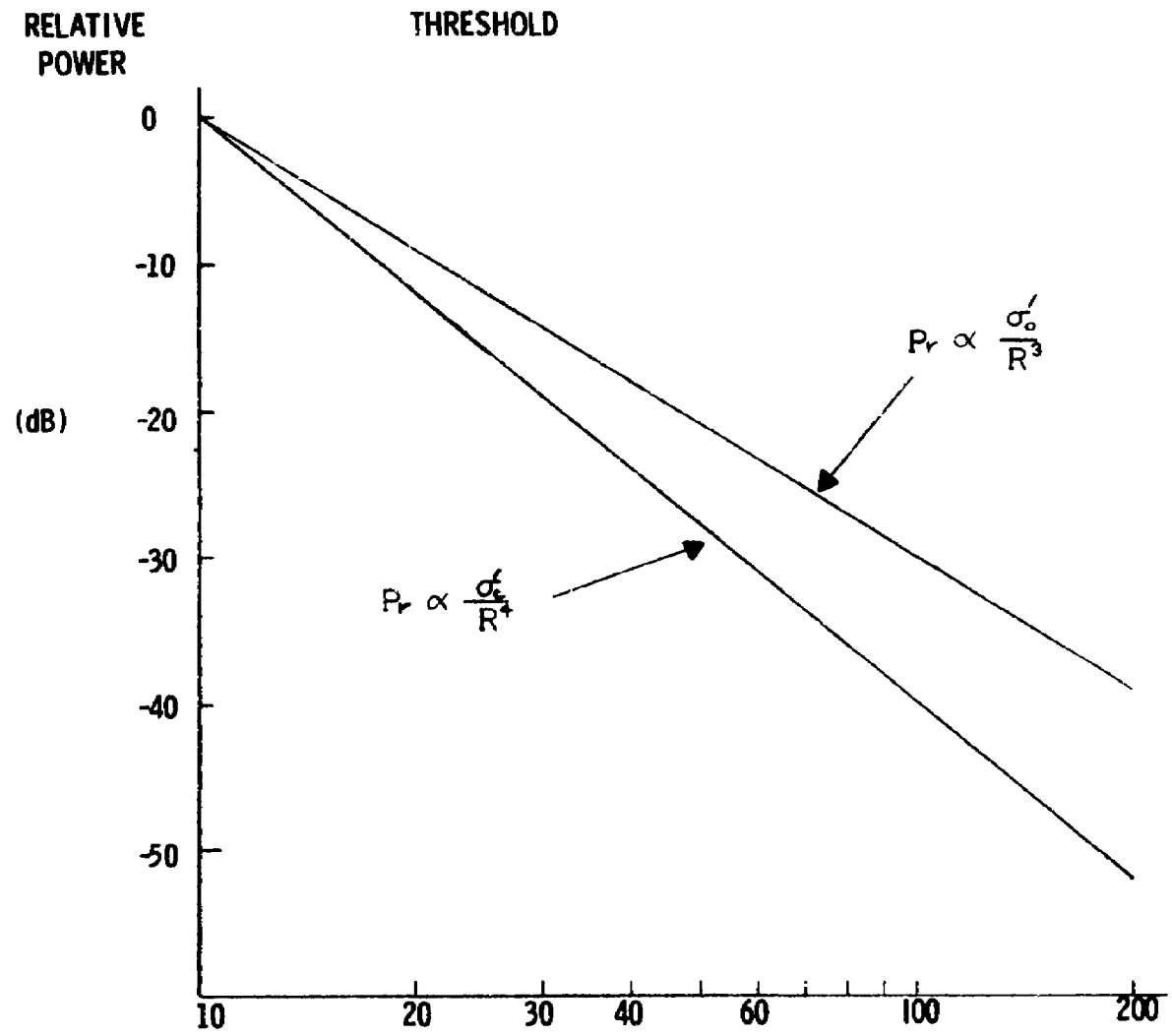

FIGURE 5: Threshold-Vs-Time (Range) Curve

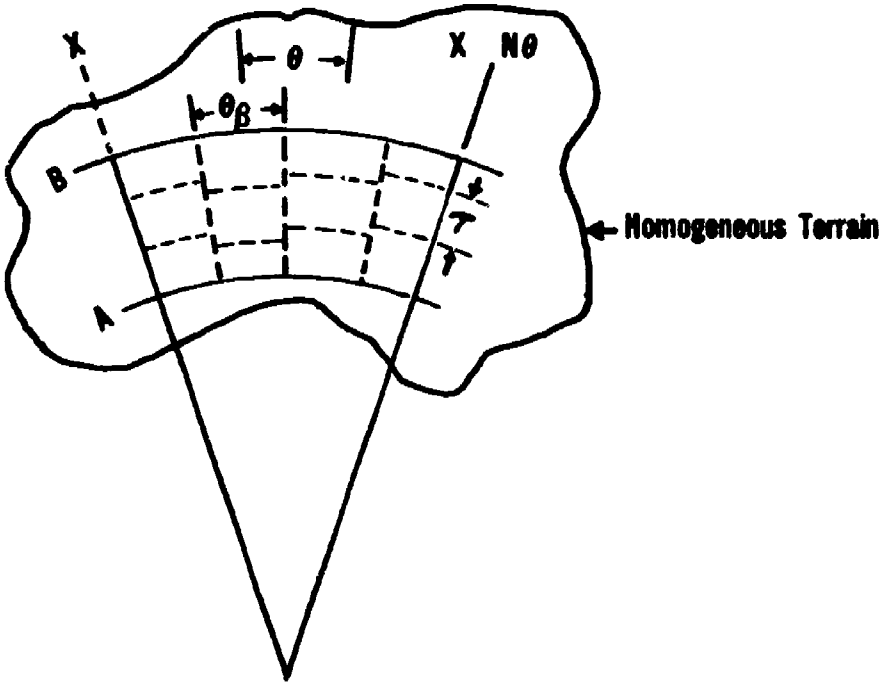

θ = Azimuthal distance between samples = $N_\theta \frac{\theta}{PRF} \geq \theta_\beta$

A = Start Range = $N_{A\tau_X}$

B = Stop Range = $N_{\beta\tau_X}$

R = B - A = $(N_B - N_A)\ \tau_X$ = Range Extent of Samples

τ_X = Distance in range between samples $\geq N_\tau$ (.1 usec) $\geq \tau$

ϵ = Total azimuth extent of samples = $N\theta$

$(N_B - N_A)N$ = Total number of samples taken

R, $\overline{PRF}$, ϵ, τ, θ_β are known constants for a given measurement and N_θ, N_A, N_B, N_τ, N are programmable parameters. The sampling interval is started manually or automatically at azimuth x.

FIGURE 6: Example of CAA Operation

independent range-azimuth cell for the programmed number of samples corresponding to the range-azimuth extent of the area being measured. The sampled outputs that exceed the threshold were counted. Then the probability that a radar return from the measured area will be greater than the threshold was estimated as

$$P\ (\sigma' > \sigma'_{th}) \simeq \frac{\text{Total No. of Threshold Crossings}}{\text{Total No. of Samples}}$$

By taking such measurements with increments of attenuation inserted, thereby changing σ'_{th}, a cumulative distribution function was easily plotted for each area of interest.

The typical pulse widths used in the measurements were 0.5, 1, 3 and 6 microseconds. All amplitude measurements were taken using an IF bandwidth of approximately 2 MHz to provide information usable for certain pulse compression systems (i.e., 13 bit Barker coded 6 usec pulse) as well as a bounding value for non-pulse compression 0.5 - 6 usec designs. To give more statistical significance to the measurements, ten measurements of each measured sector were performed at each 5 dB attenuation level and averaged to obtain each plotted value. All measurements were made with threshold-to-rms noise ratios of 10 dB or more within the measurement range to reduce the contamination caused by noise. Finally, the average antenna gain, which varies as a function of terrain and distance, was calculated for each measurement to reduce the

error. A detailed error analysis of the measurements is presented in Appendix B.

B. Spectral Measurements:

The purpose of the spectral measurements was to obtain information on the intrinsic radar clutter spectra of land, sea, weather and if possible, angels. The spectrum analysis equipment consisted of a model 440 Mini-Ubiquitous Portable Spectrum Analyzer (Nicolet Scientific Corp.) and radar interface equipment as shown in Figure 7. This analyzer performs an FFT on 1024 time samples and displays 400 frequency points on a display. The resolution and maximum display frequency was selectable from .025 Hz at 10 Hz to 50 Hz at 20 KHz. Other useful features of the analyzer include 4 averaging modes and a choice of linear or log displays. The information was recorded on oscillographs of the spectrum analyzer output. The spectrum analyzer oscillograph annotation is given in Figure 8. The interface was designed primarily for analyzing frequencies less than 50 Hz (∿12 knots) but could be extended up to one-half of the PRF by accounting for the low pass filter and sample-and-hold attenuation given in Figure 9.

The methodology used was straightforward. Areas were chosen for examination thru observation of the MTI PPI display. These areas were correlated with a topographic map to determine the terrain type. The antenna was stopped and set to the chosen

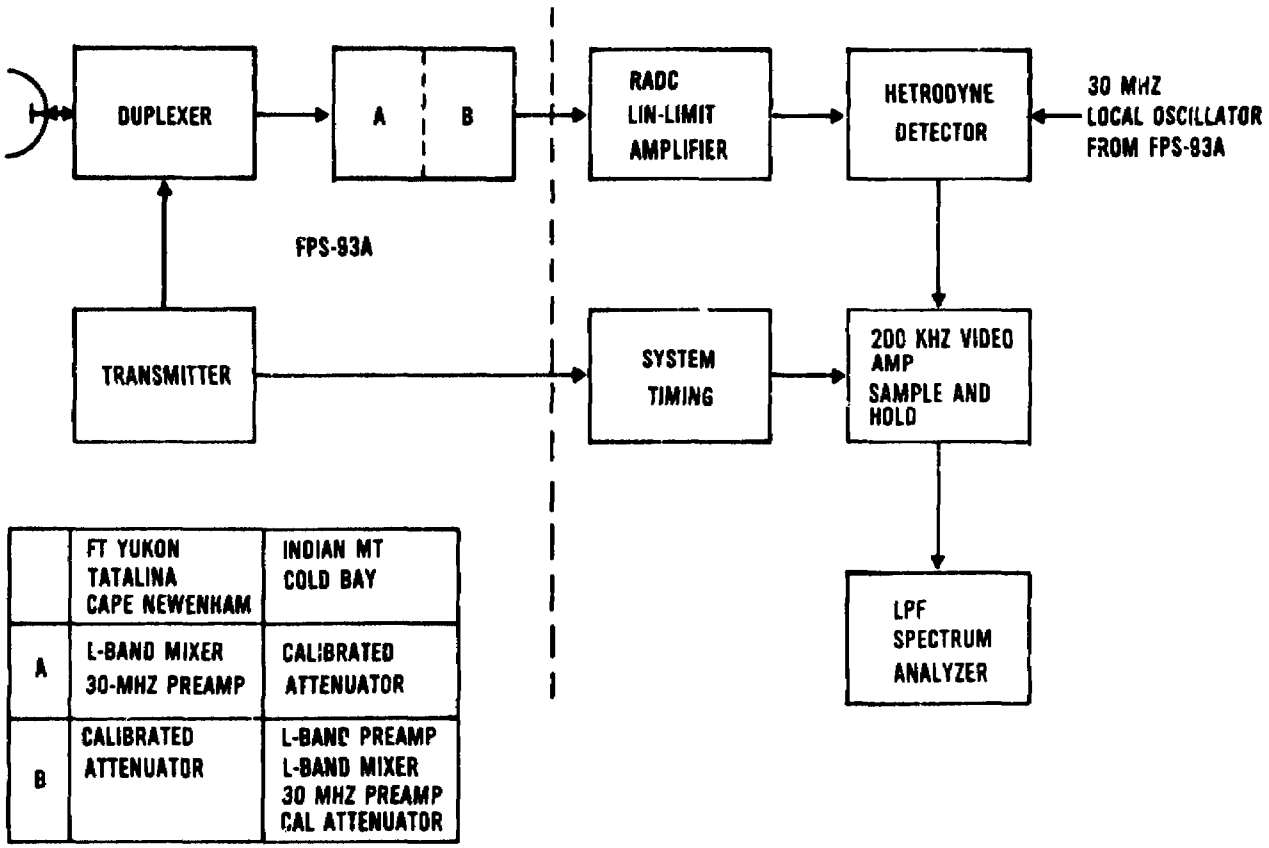

	FT YUKON TATALINA CAPE NEWENHAM	INDIAN MT COLD BAY
A	L-BAND MIXER 30-MHZ PREAMP	CALIBRATED ATTENUATOR
B	CALIBRATED ATTENUATOR	L-BAND PREAMP L-BAND MIXER 30 MHZ PREAMP CAL ATTENUATOR

FIGURE 7: Block Diagram of Spectrum Analyzer Interface

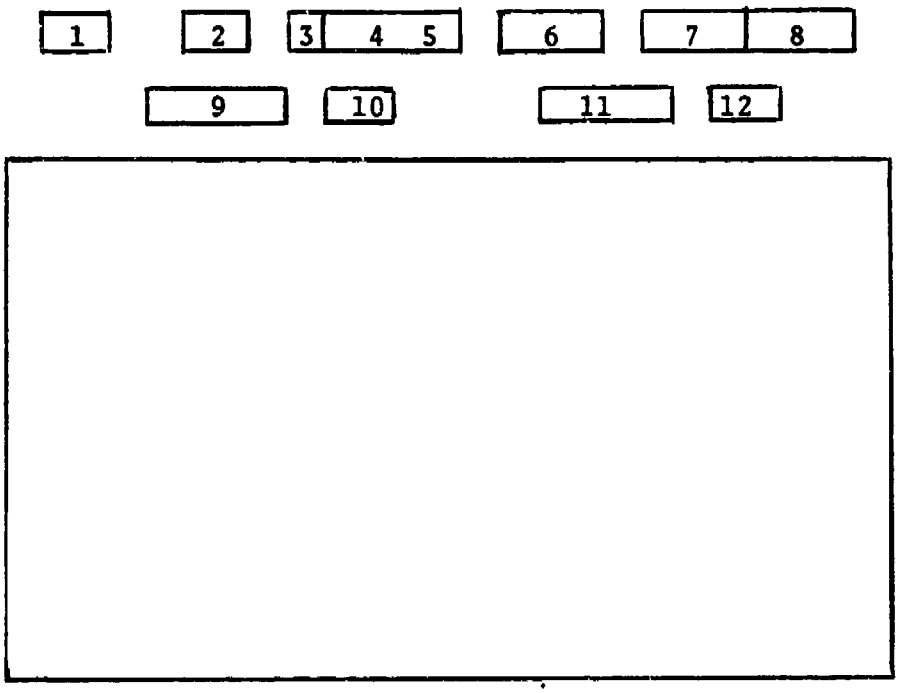

The above template is provided to decode the photographs that follow:

1. Amplitude Controls (dB)
2. Max Frequency Displayed
3. Display Mode:

   S = Averaging Mode
   I = Instantaneous Mode
   T = Time Display
4. Number of Spectra Averaged
5. Data Weighting: W - Hanning
   U - Uniform
6. Frequency Scale:

   HLN - Linear
   HLG - Log
7. Amplitude Scale:

   VLN - Linear
   VLG - Log
8. Amplitude Display Max (dB)
9. Cursor Frequency
10. Hz
11. Amplitude of Display at Cursor Frequency
12. dB

FIGURE 8: Spectrum Analyzer Annotation Identification

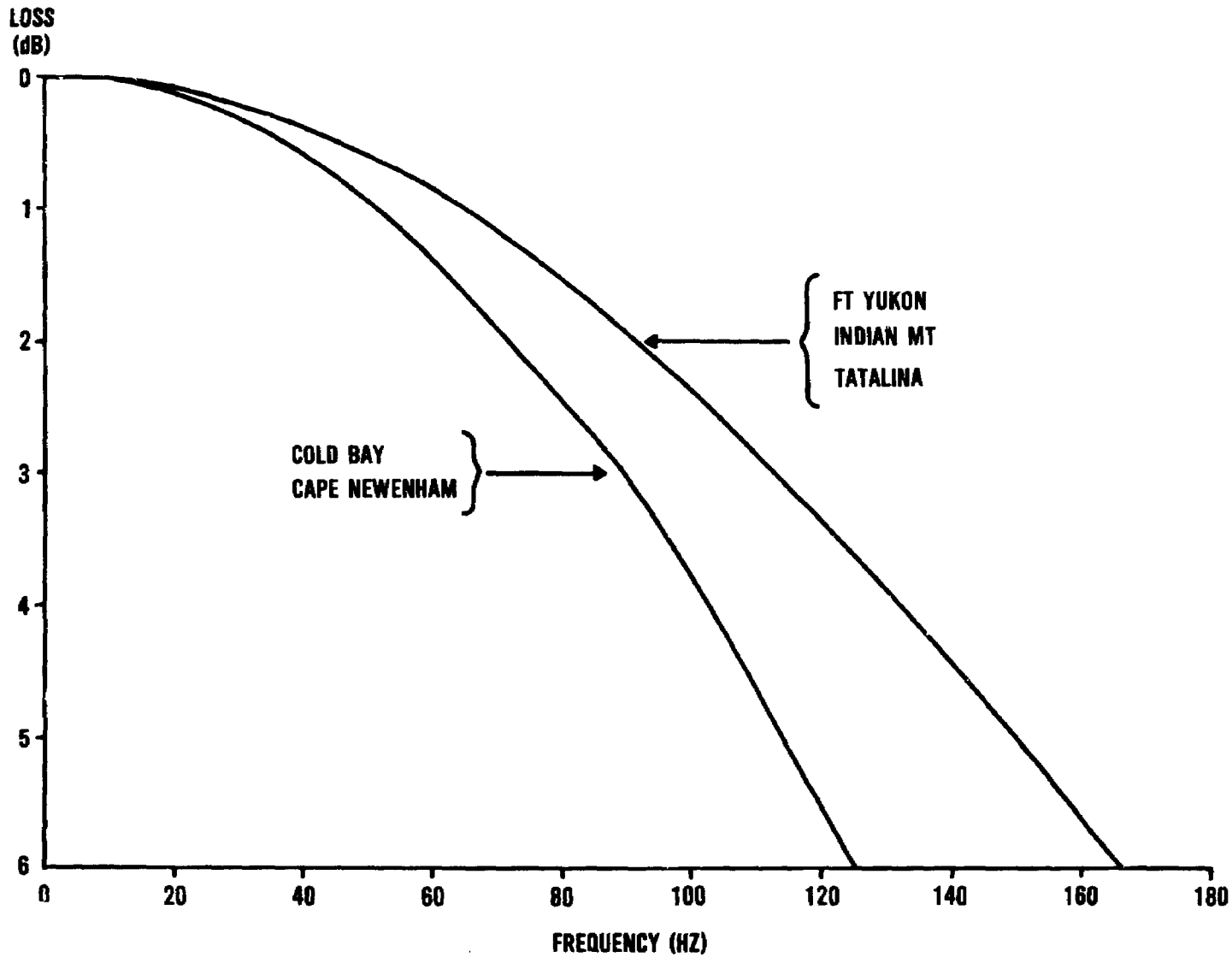

FIGURE 9: Cascaded Sampler-And-Hold and LPF Transfer Function

azimuth, "searchlighting" the clutter area to be examined. The received signals were heterodyned to baseband, amplified and filtered. A chosen range cell within the linear range of the receiver was boxcarred, providing an audio signal for the spectrum analyzer.

First, the degree of spectral contamination caused by transmitter noise and system instability was bounded by examining the spectra of several "stable" clutter returns from fixed point targets at different ranges. Then chosen clutter areas at the same or lesser ranges were examined and recorded.

IV. SPATIAL AMPLITUDE DISTRIBUTIONS OF TERRAIN AND SEA CLUTTER:

The probability distributions for land clutter are shown in Figures 10 through 32. The presentation of this data is broken down into five (5) categories:

a. Flat lands, such as swamps, muskeg, plains, Figures 10-11.
b. Hills and mountains, partially wooded - Figures 13 - 23.
c. Volcanic mountains - Figures 24 - 26.
d. The composite distribution of all terrain features over a 360° azimuth from 15 to 50 and 15 to 100 nautical miles range - Figures 27 and 28.
e. Comparative distributions of different locations of flat lands, hills, and mountains - Figures 29 - 32.

One (1) sea clutter distribution is presented in Figure 33.

These figures show the percentage of the samples in which the reflectivity exceeds the amplitude in dB shown on the abscissa.

Also shown on each graph is the site, date, time, pulse width and a description of the terrain feature which the data represents. Except when noted, each figure shows a family of curves with pulse width as a parameter. Since each site is currently part of the Alaskan early warning system, area codes are given in lieu of the range-azimuth locations of each measurement.

All the figures indicate that the distribution functions range between log normal[1,2] and contaminated normal[2,3]. Examples of

these distributions are shown in Figure 34 with a Rayleigh distribution for comparison and the medians of each normalized to zero dB.

From an examination of the data, the distributions tend toward log-normal as the sample areas became uniform or homogeneous. This is brought out by the straight line nature of the distribution for muskeg backscatter. The effect is shown particularly in the tails of Figures 10 through 13. Also note that for this type of terrain at low grazing angles, such as at Fort Yukon (Figure 10) and Cape Newenham (Figure 12), the log-normal spread[4] between the median and the 84 percentile is large, from 11 to 16 dB. For the higher grazing angles, such as at Tatalina, Figure 11, overlooking a sloping wooded area broadside, the spread is lower, about 7 dB. This is perhaps due to less shadowing[4]. Note the spread also tends to be larger for shorter pulse widths. The spread for the predicted log-normal distribution was scaled from the curves by extrapolating the bottom (lower percentile) end toward the top (50 percentile) end.

For hilly terrain with average elevation increasing with range, the curves begin to deviate from a straight line and appear as contaminated-normal. This begins to occur in the curves for Cape Newenham (Figure 12), Indian Mountain (Figure 13), and at Tatalina (Figure 21). All three of these areas have hills rising in the direction away from the radar and have relatively uniform granularity.

As larger areas of shadowing and attendant facing slopes are observed, a pronounced knee appears in the curves. This is brought out by the sector observed at Tatalina (Figure 22) where approximately 20% of the area is shadowed and about 50% of the area is sloped such that the radar grazing angle is large.

Extreme cases of contaminated-normal are seen in sectors observed at Indian Mountain (Figure 15) where deep valleys and rising mountain faces extend over large portions of the sector. The two (2) curves in this figure are very irregular suggesting large differences in the contaminated-normal parameters[3].

As one observes high mountains over very large sectors such as at Indian Mountain (Figures 16 and 17) and at Tatalina (Figure 23), the irregular effects in the curve appear to decrease. This can be due to the large areas under observation and the averaging of the reflectivity.

The composite curves, Figures 27 and 28, show a very large difference in slope between the 50 percentile and the low percentiles but the transition is smooth. Here the averaging effects described in the preceding paragraph are occuring over the entire curve. For example, the averaging of the individual curves in Figures 29 to 31 would tend toward this result.

The conclusions which can be drawn from the data and discussion are that:

1. Homogeneous clutter whose scatterers are larger than a carrier wavelength and much less than a resolution cell has a log-normal (straight line) distributed reflectivity. The smaller the grazing angle the larger the spread between the 50 and 84 percentile.

2. The more heterogeneous the data becomes, where large areas within a sector become shadowed and large exposed areas become eminent, the more contaminated-normal like the distribution becomes with very irregular knees and bends. Note we are citing large areas of shadowing and exposure, not numerous small areas.

3. As the areas of shadowing and exposure become numerous by observing larger and larger sectors, the distribution takes on a smooth transition from a low slope at the 50 percentile to a high slope at the low percentiles.

4. For the worst case conditions at the tails of the distribution curve we may assume a log-normal function according to Table III. This will give an upper bound for low false alarm thresholds. An approximate per cent occurrence of the three terrain types, obtained from contour maps of several sites, are also given.

TABLE III: Worst Case Land Clutter Model

(Extrapolated from the Tails of Distributions)

TERRAIN TYPE	VEGETATION	HEIGHT (FT)	PER CENT OCCUR-RENCE	EXTRAPOLATED REFLECTIVITY DISTRIBUTION AT TAILS OF CURVES	
				MEDIAN	84TH PERCENTILE
Mountains	Bare	4000	13	-20	-14
Wooded	Grass-Moss	4000	53	-19	-12
Hills	Small Trees	1000	--	---	---
Valleys/	Heavily Wooded	1000	34	-20	-13
Muskeg	Spruce, Birch	----	--	---	---
Everything (Composite: 15-100 NM)	----------	----	--	-23.5	-17.5

CURVE NO.	PLACE	DATE	τ usec	TERRAIN TYPE	AREA NO.
1	FORT YUKON	12 AUG	6.2	MUSKEG	1
2	FORT YUKON	12 AUG	3.0	MUSKEG	1
3	FORT YUKON	12 AUG	1.0	MUSKEG	1
4	FORT YUKON	12 AUG	0.5	MUSKEG	1

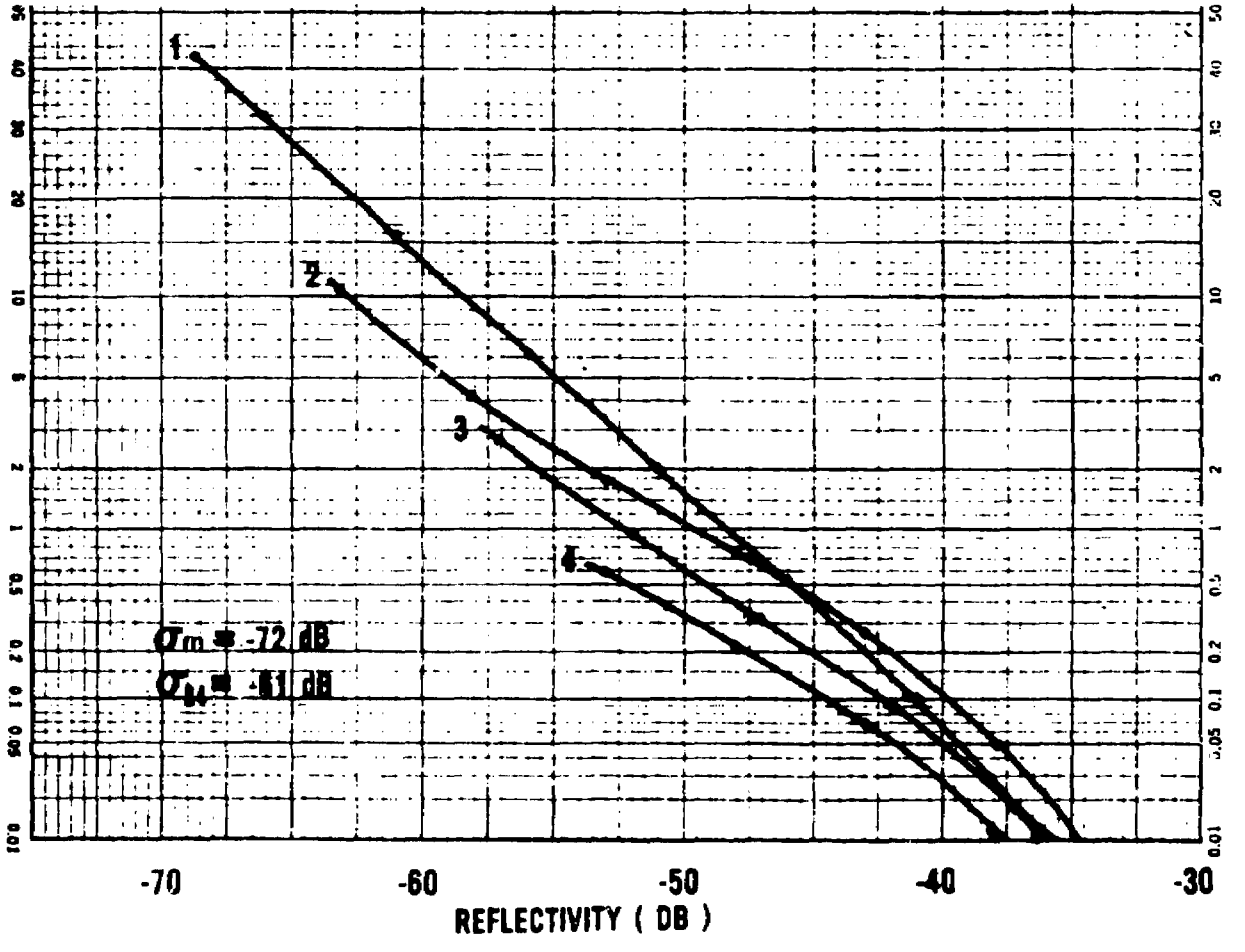

FIGURE 10: Muskeg (Fort Yukon)

CURVE NO.	PLACE	DATE	τ usec	TERRAIN TYPE	AREA NO.
13	TATALINA	25 AUG	6.0	SWAMP	7
16	TATALINA	25 AUG	3.0	SWAMP	7
21	TATALINA	25 AUG	1.0	SWAMP	7
23	TATALINA	25 AUG	0.5	SWAMP	7

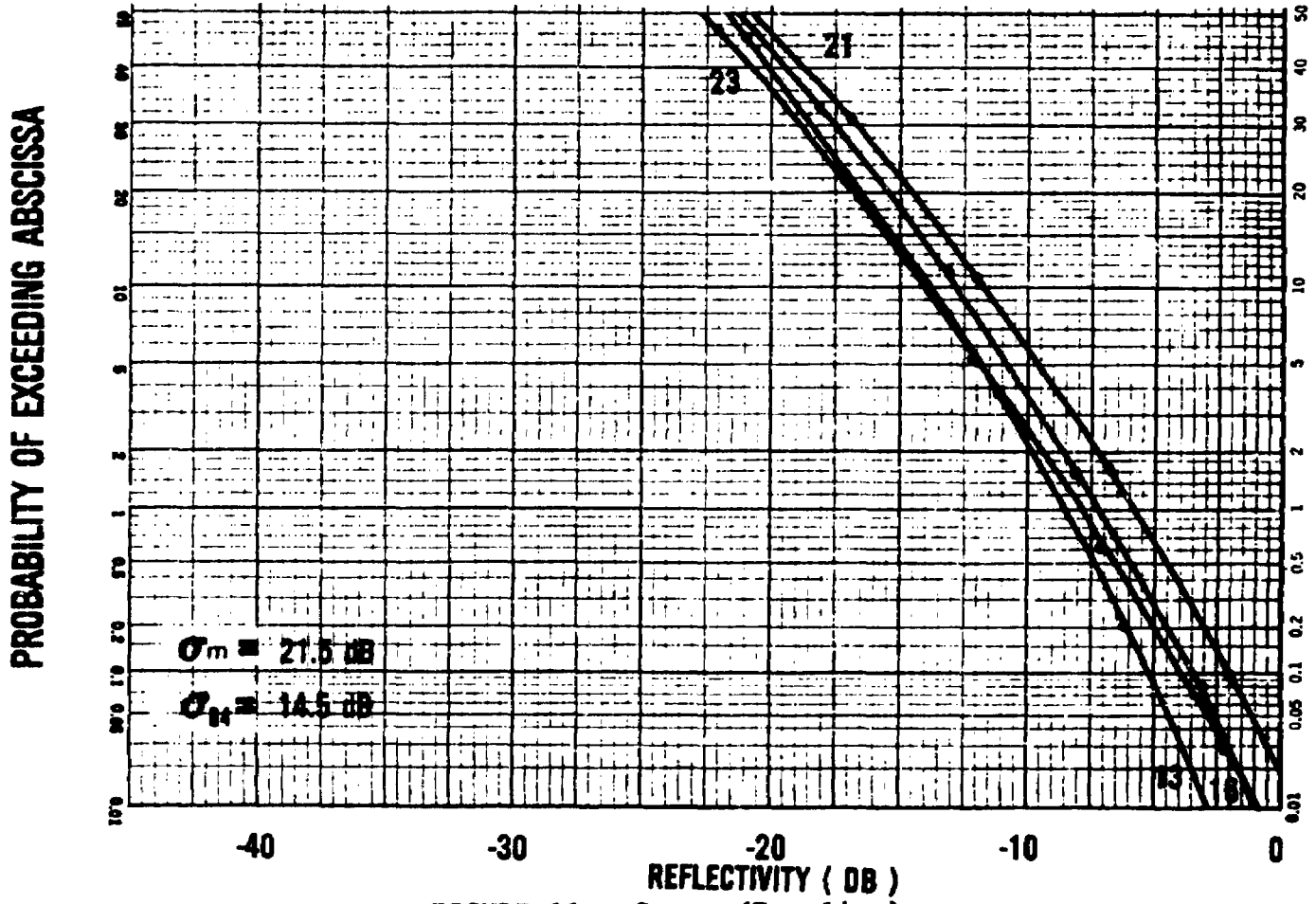

FIGURE 11: Swamp (Tatalina)

CURVE NO.	PLACE	DATE	τ usec	TERRAIN TYPE	AREA NO.
11	CAPE NEWENHAM	6 SEPT	6.0	HILLY ISLAND	5
12	CAPE NEWENHAM	6 SEPT	3.0	HILLY ISLAND	5
13	CAPE NEWENHAM	6 SEPT	1.0	HILLY ISLAND	5

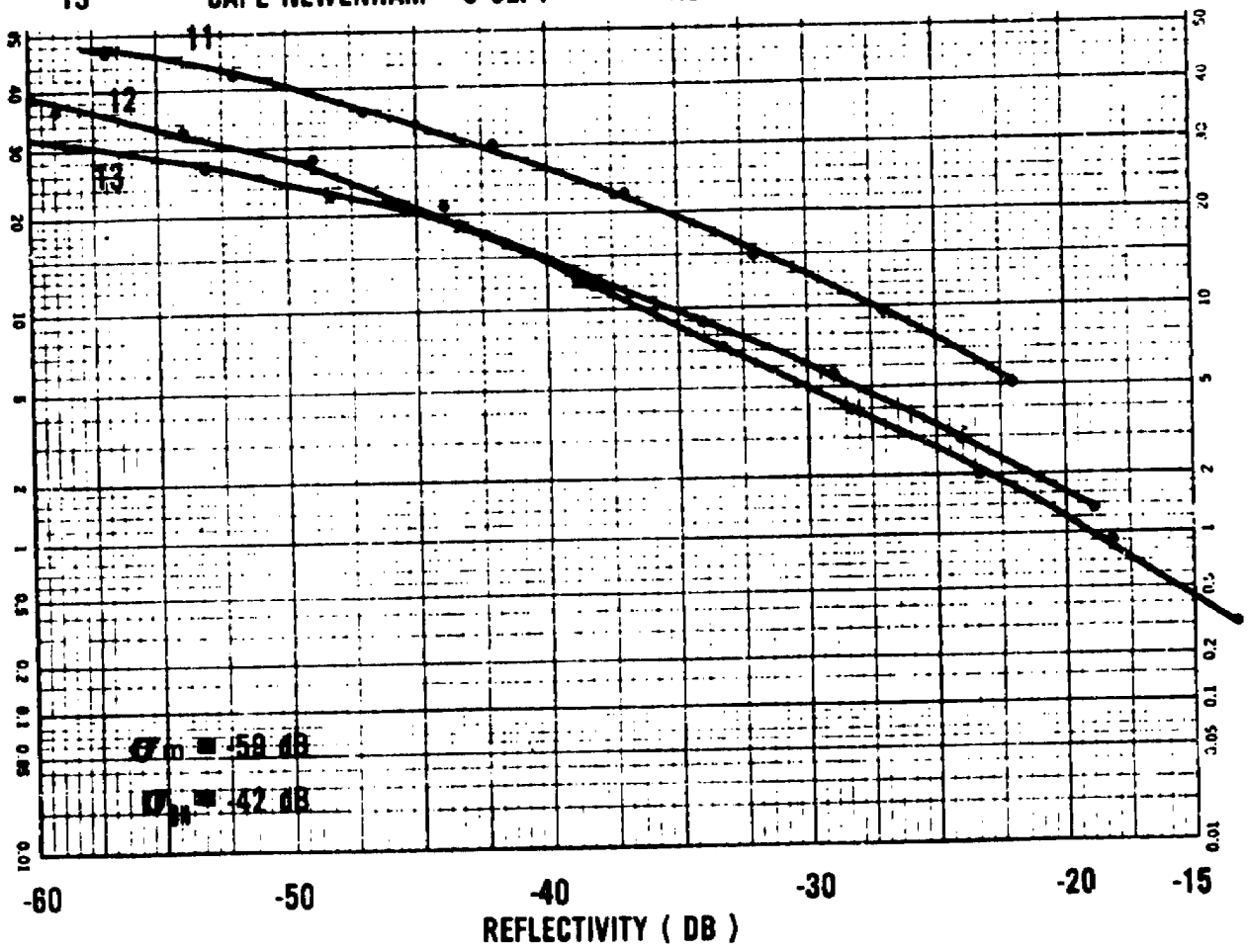

FIGURE 12: Hilly Island (Cape Newenham)

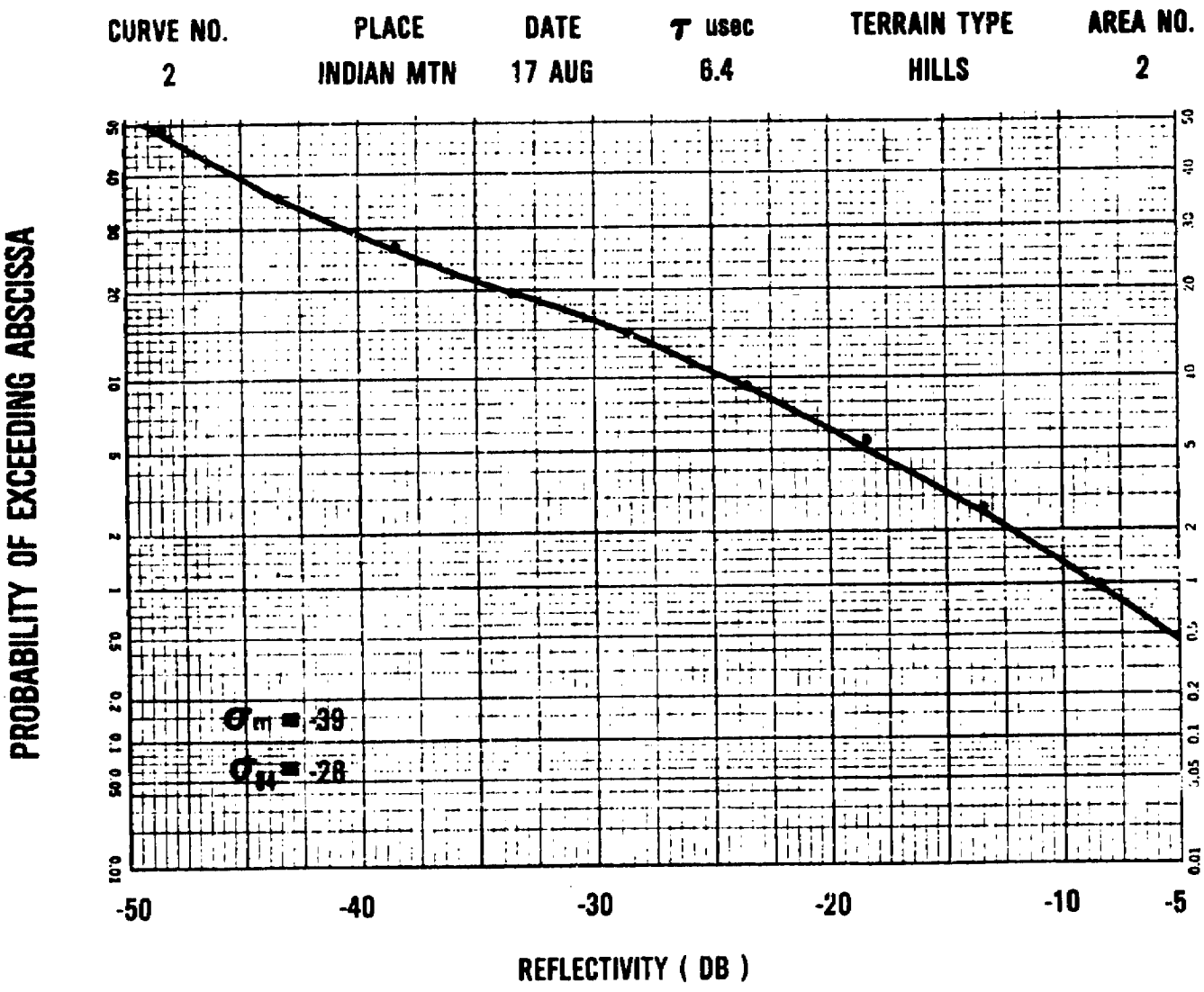

FIGURE 13: Hills (Indian Mountain)

CURVE NO.	PLACE	DATE	τ usec	TERRAIN TYPE	AREA NO.
3	CAPE NEWENHAM	4 SEPT	3.0	HILLS	3
4	CAPE NEWENHAM	5 SEPT	6.3	HILLS	3
5	CAPE NEWENHAM	5 SEPT	1.0	HILLS	3

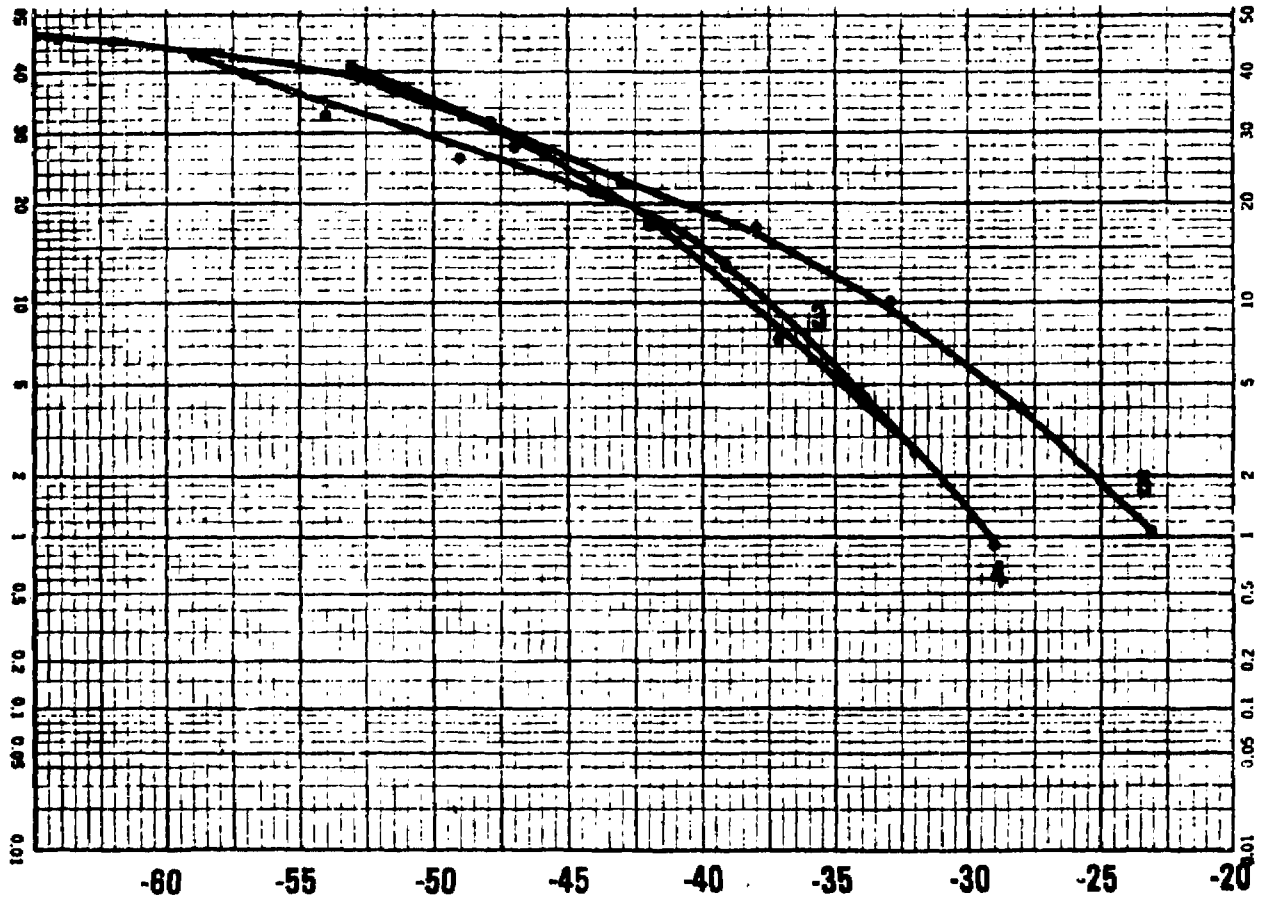

FIGURE 14: Hills (Cape Newenham)

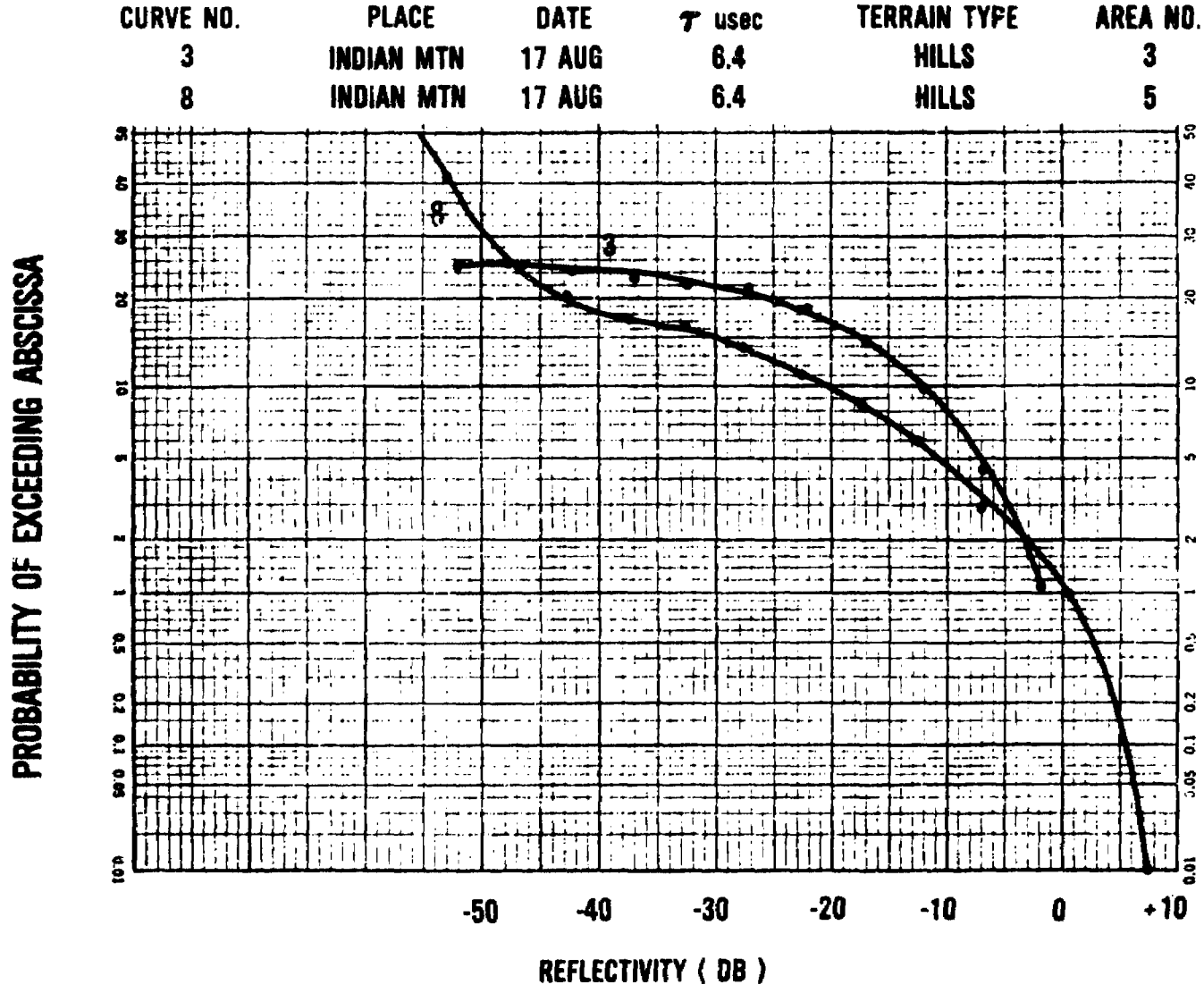

FIGURE 15: Hills (Indian Mtn)

CURVE NO.	PLACE	DATE	τ usec	TERRAIN TYPE	AREA NO.
4	INDIAN MTN	17 AUG	6.4	HILLS	4
5	INDIAN MTN	17 AUG	3.0	HILLS	4
6	INDIAN MTN	17 AUG	1.0	HILLS	4
7	INDIAN MTN	17 AUG	0.6	HILLS	4A ★

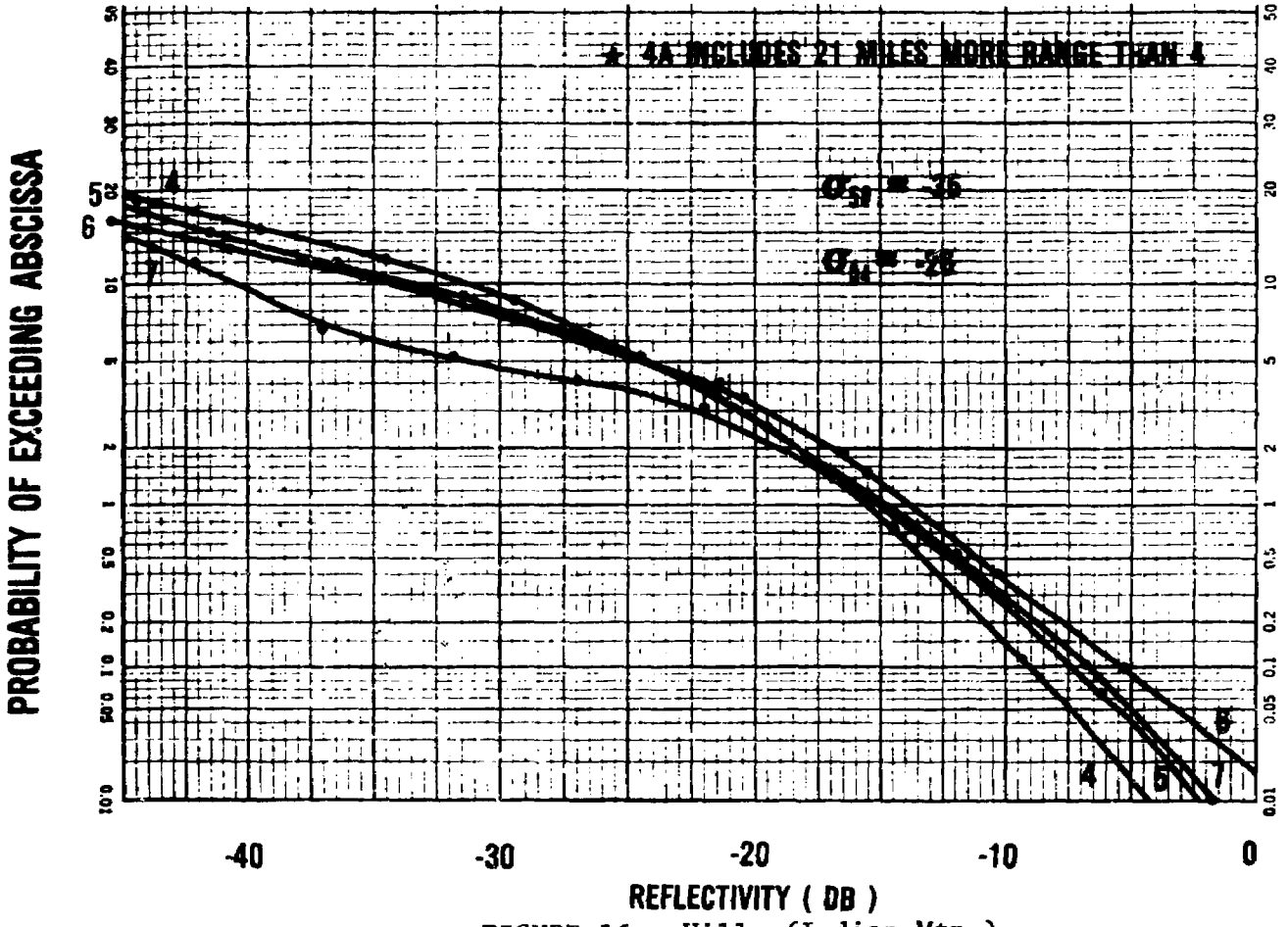

FIGURE 16: Hills (Indian Mtn.)

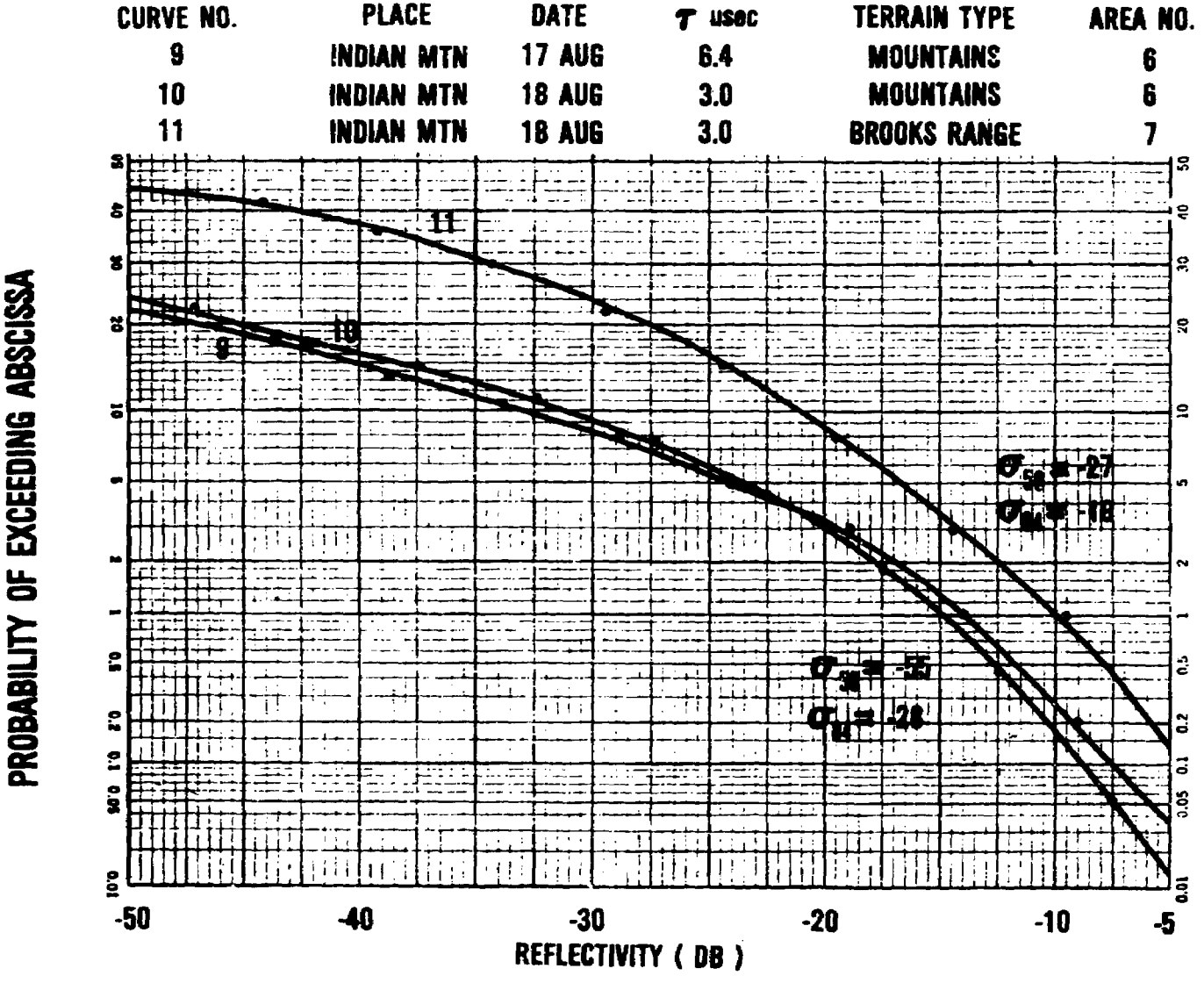

FIGURE 17: Mountains (Indian Mtn)

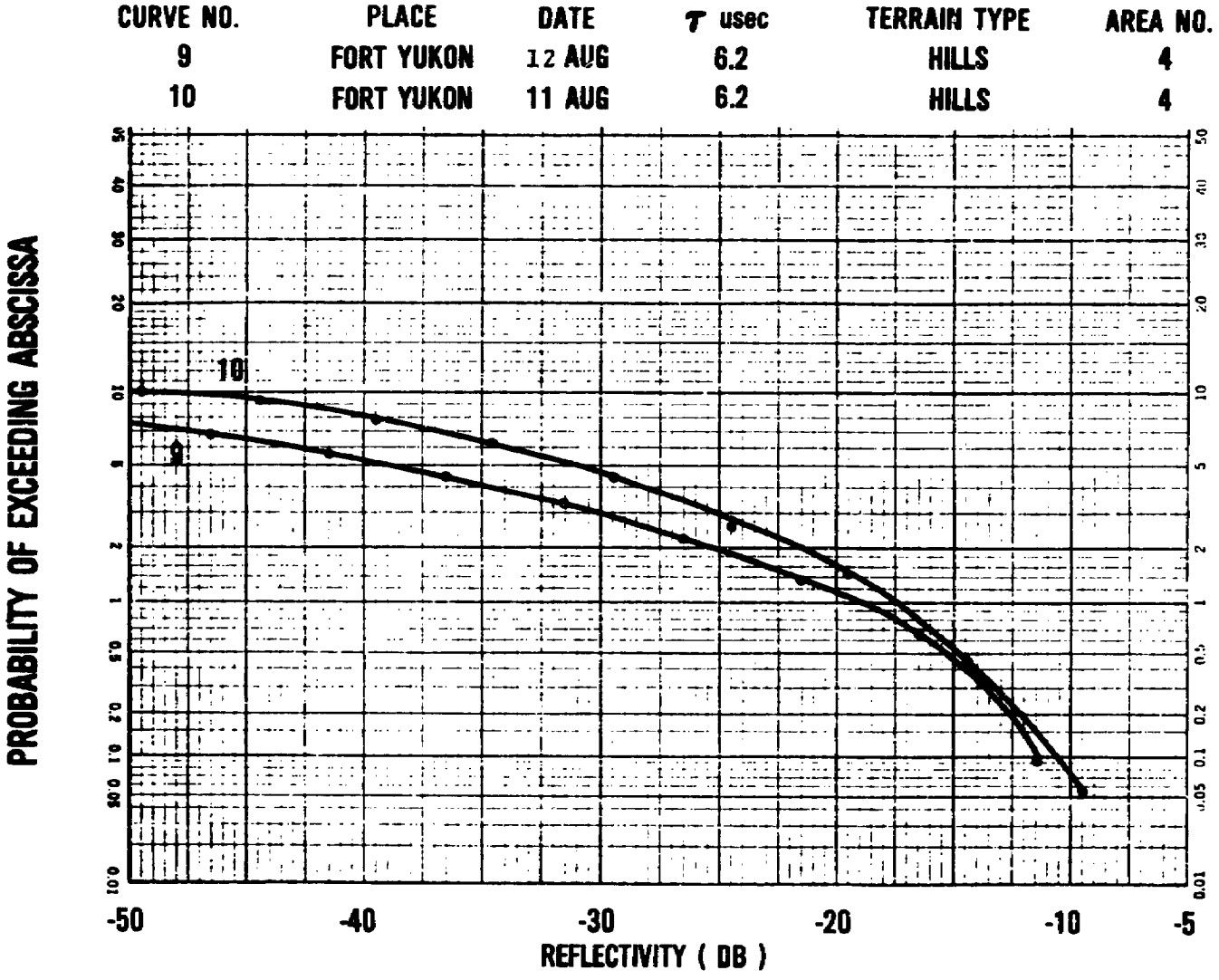

FIGURE 18: Hills (Fort Yukon)

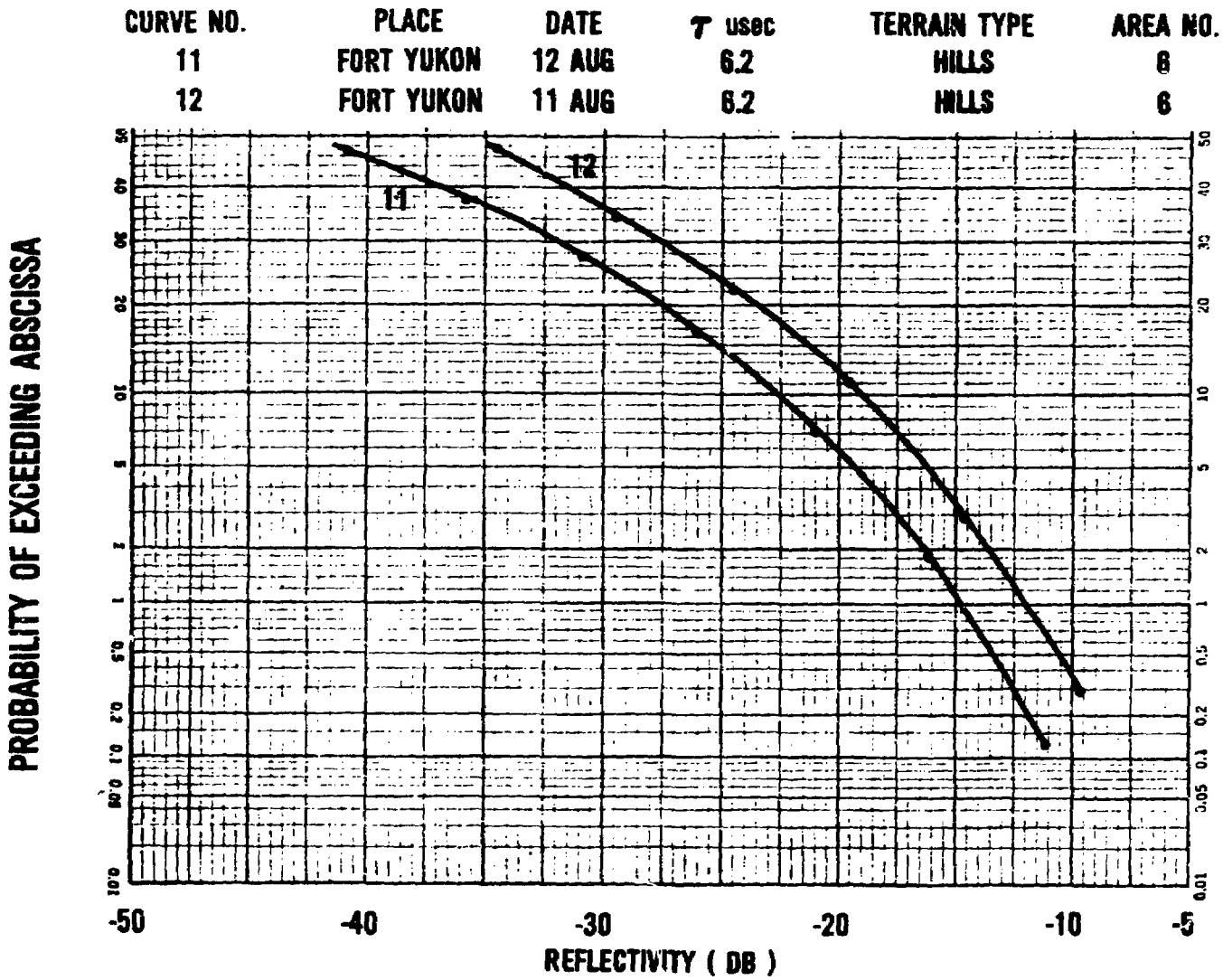

FIGURE 19: Hills (Fort Yukon)

CURVE NO.	PLACE	DATE	τ usec	TERRAIN TYPE	AREA NO.
5	FORT YUKON	12 AUG	3.0	HIGH HILLS, MTNS	3
6	FORT YUKON	12 AUG	1.0	HIGH HILLS, MTNS	3
7	FORT YUKON	12 AUG	0.5	HIGH HILLS, MTNS	3
8	FORT YUKON	11 AUG	6.2	HIGH HILLS, MTNS	3
13	FORT YUKON	9 AUG	6.2	HIGH HILLS, MTNS	3

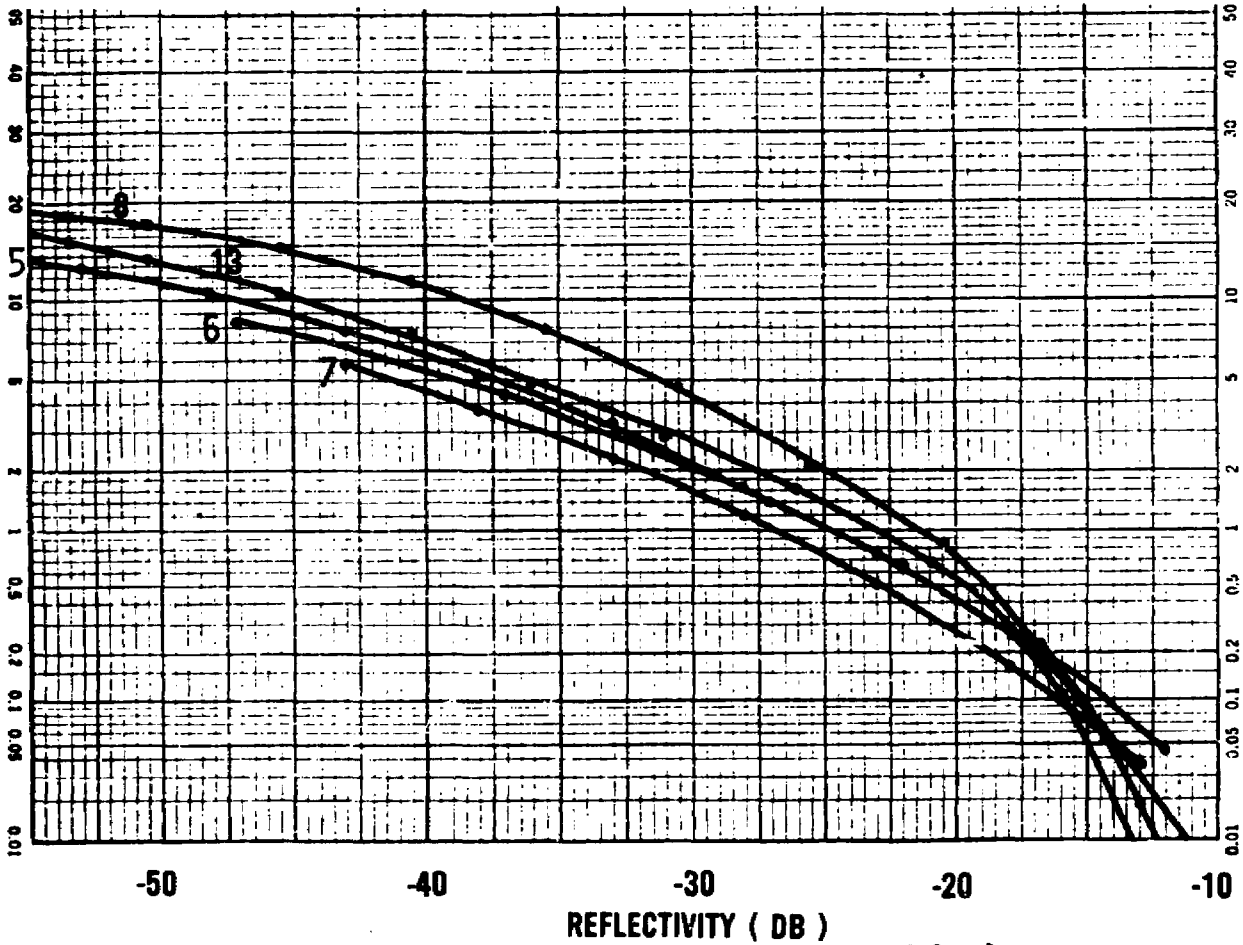

FIGURE 20: High Hills, Mountains (Fort Yukon)

CURVE NO.	PLACE	DATE	τ usec	TERRAIN TYPE	AREA NO.
15	TATALINA	25 AUG	6.0	LOW MTNS/HIGH HILLS	9
18	TATALINA	25 AUG	3.0	LOW MTNS/HIGH HILLS	9
19	TATALINA	25 AUG	1.0	LOW MTNS/HIGH HILLS	9
22	TATALINA	25 AUG	0.5	LOW MTNS/HIGH HILLS	9

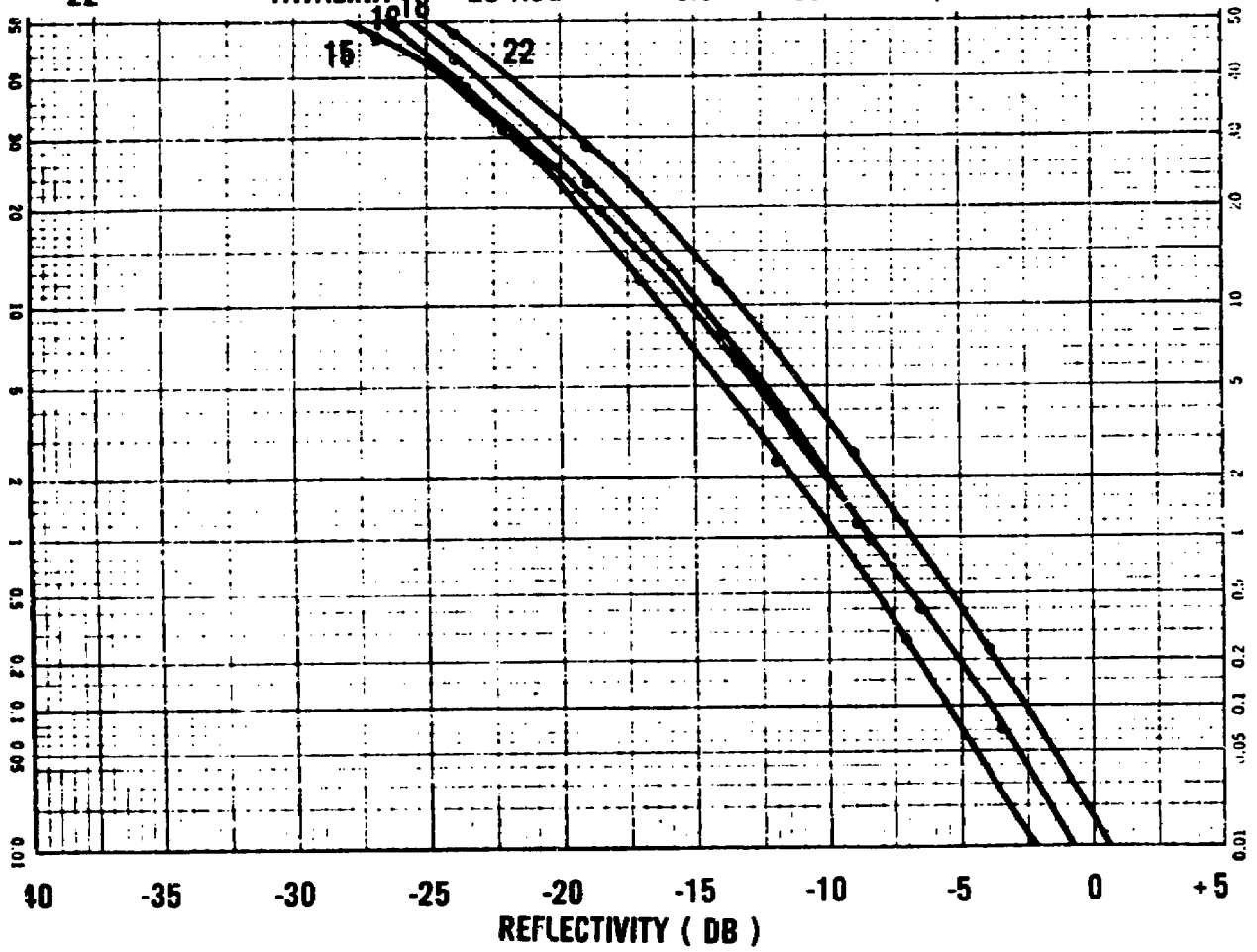

FIGURE 21: High Hills, Mountains (Tatalina)

CURVE NO.	PLACE	DATE	τ usec	TERRAIN TYPE	AREA NO.
12	TATALINA	25 AUG	6.0	HILLS	6
17	TATALINA	25 AUG	3.0	HILLS	6
20	TATALINA	25 AUG	1.0	HILLS	6
24	TATALINA	25 AUG	0.5	HILLS	6

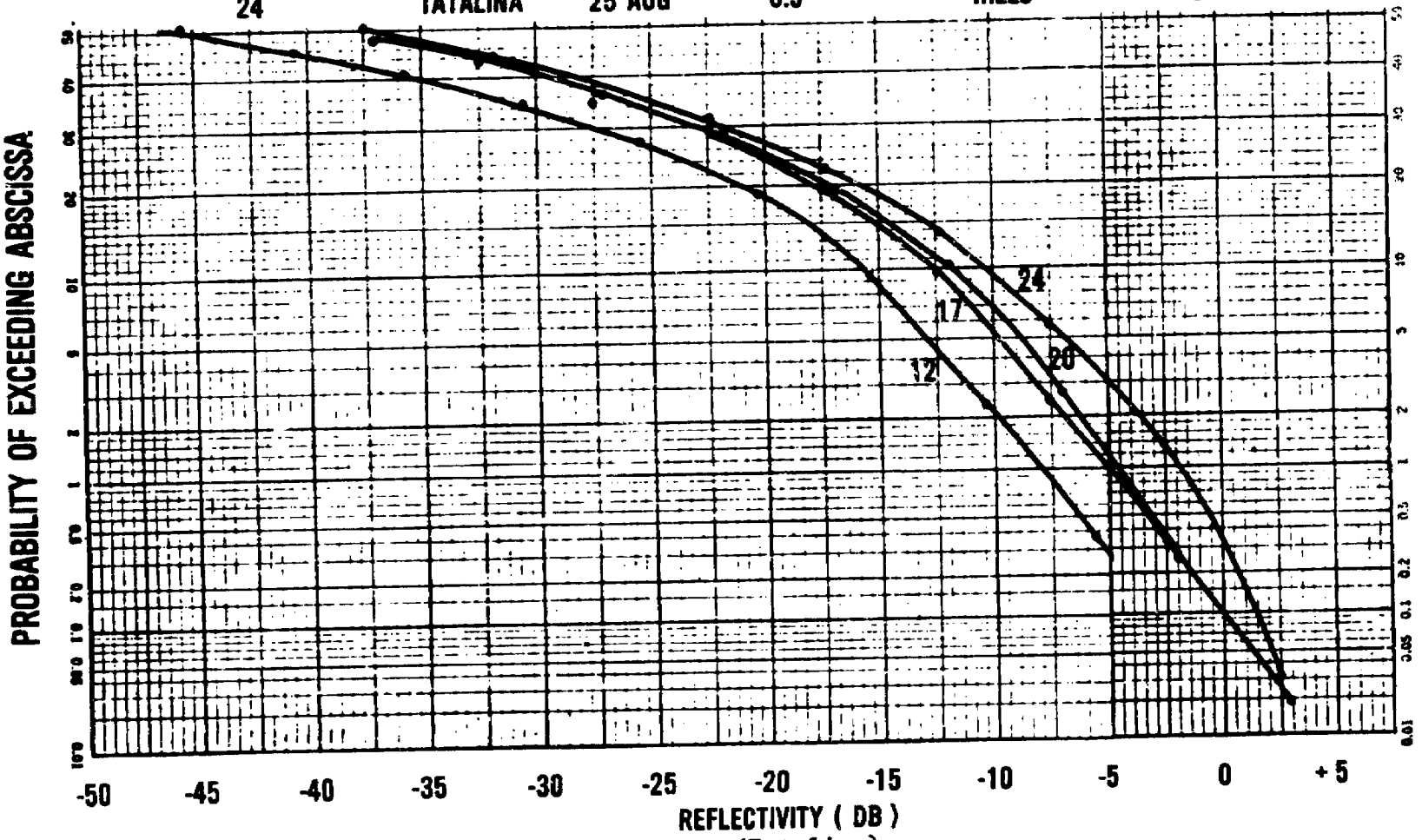

FIGURE 22: Hills (Tatalina)

CURVE NO.	PLACE	DATE	τ usec	TERRAIN TYPE	AREA NO.
8	INDIAN MTN	17 AUG	6	SEE CURVES	4
12	INDIAN MTN	17 AUG	6	SEE CURVES	7
14	TATALINA	25 AUG	6	SEE CURVES	8

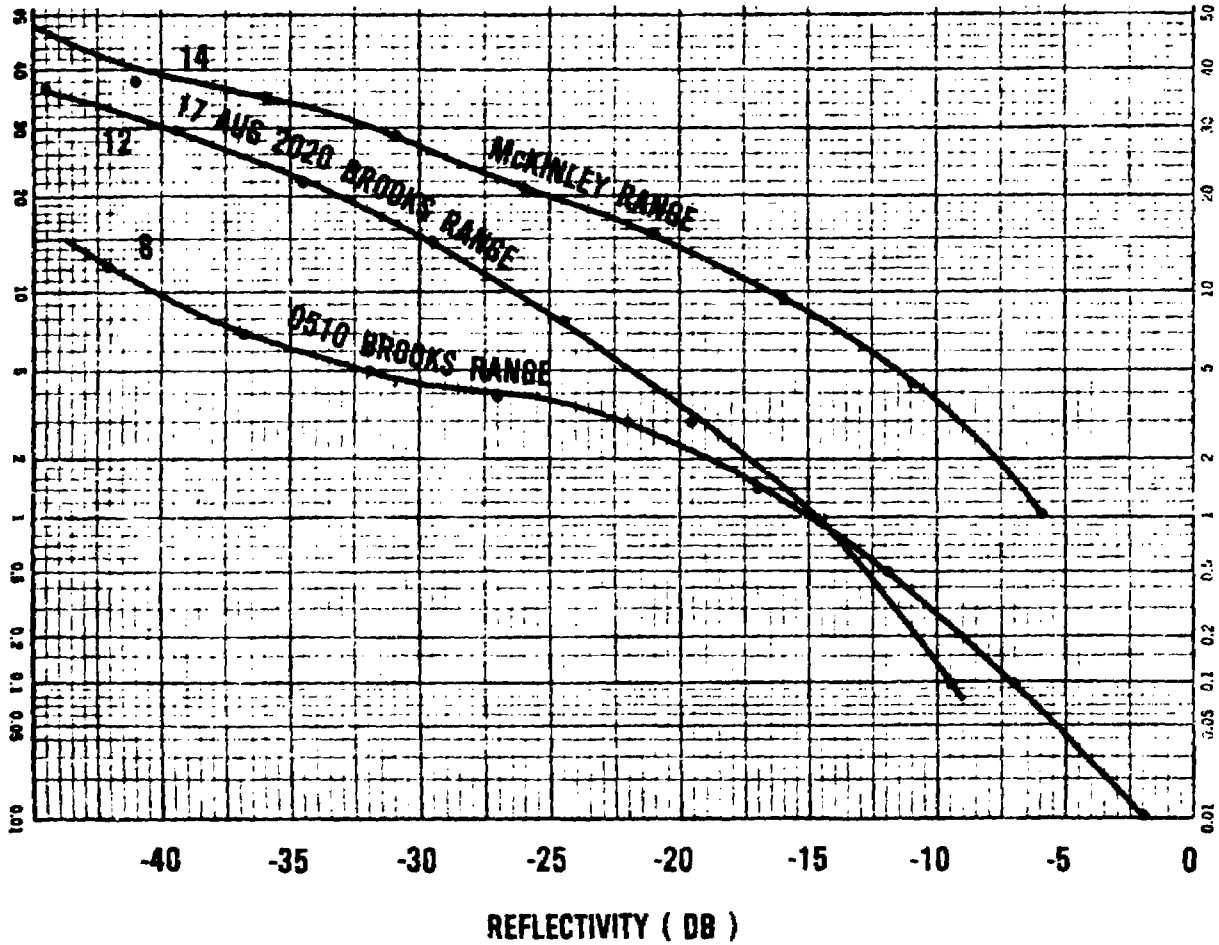

FIGURE 23: Mountains (Indian Mtn.)

CURVE NO.	PLACE	DATE	τ usec	TERRAIN TYPE	AREA NO.
1	COLD BAY	14 SEPT	5.7	VOLCANIC MOUNTAINS	1
3	COLD BAY	14 SEPT	5.7	VOLCANIC MOUNTAINS	1
5	COLD BAY	14 SEPT	3.0	VOLCANIC MOUNTAINS	1
8	COLD BAY	14 SEPT	1.0	VOLCANIC MOUNTAINS	1

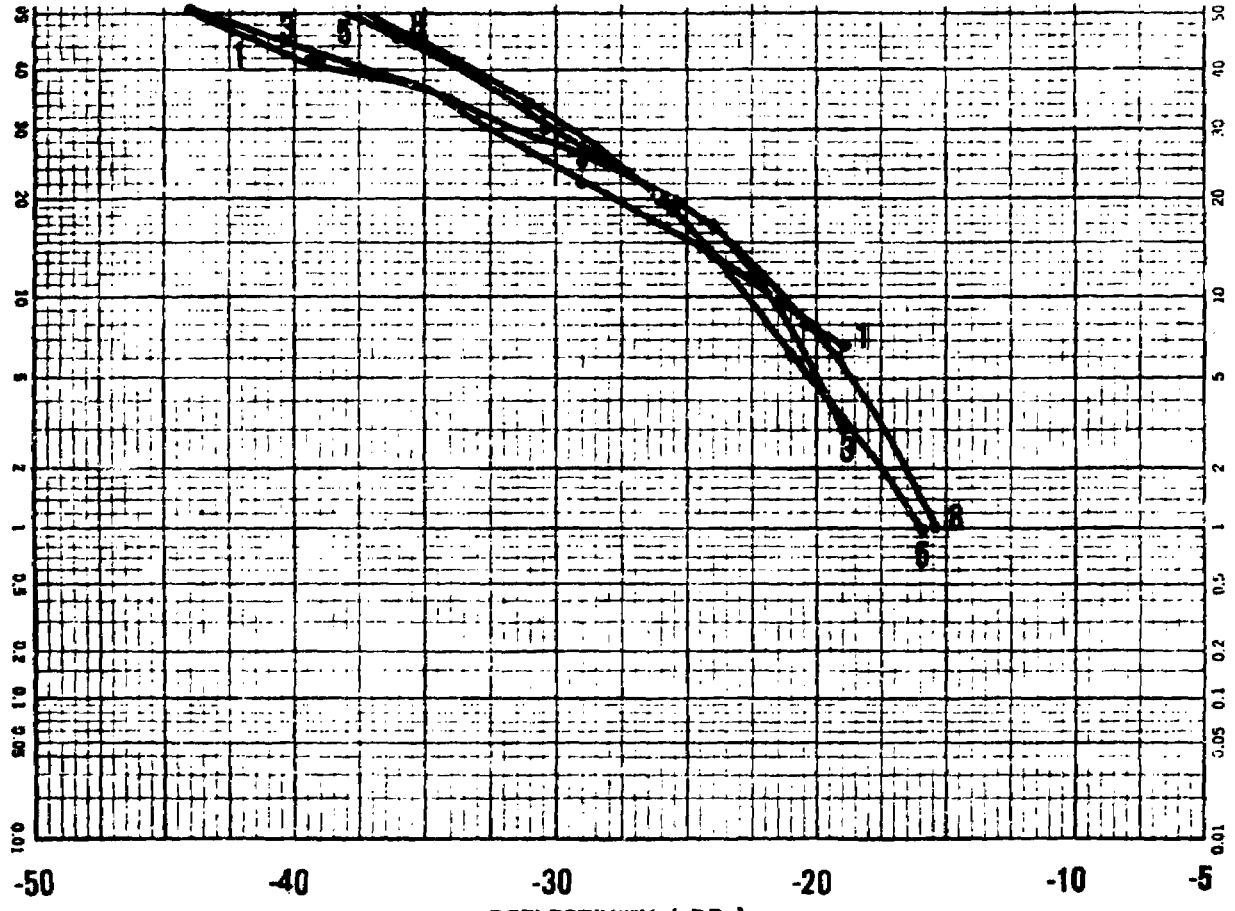

FIGURE 24: Volcanic Mountains (Cold Bay)

CURVE NO.	PLACE	DATE	τ usec	TERRAIN TYPE	AREA NO.
9	COLD BAY	15 SEPT	0.5	VOLCANIC MOUNTAINS	1
11	COLD BAY	15 SEPT	5.7	VOLCANIC MOUNTAINS	1
12	COLD BAY	15 SEPT	3.0	VOLCANIC MOUNTAINS	1
13	COLD BAY	15 SEPT	1.0	VOLCANIC MOUNTAINS	1
14	COLD BAY	15 SEPT	0.5	VOLCANIC MOUNTAINS	1

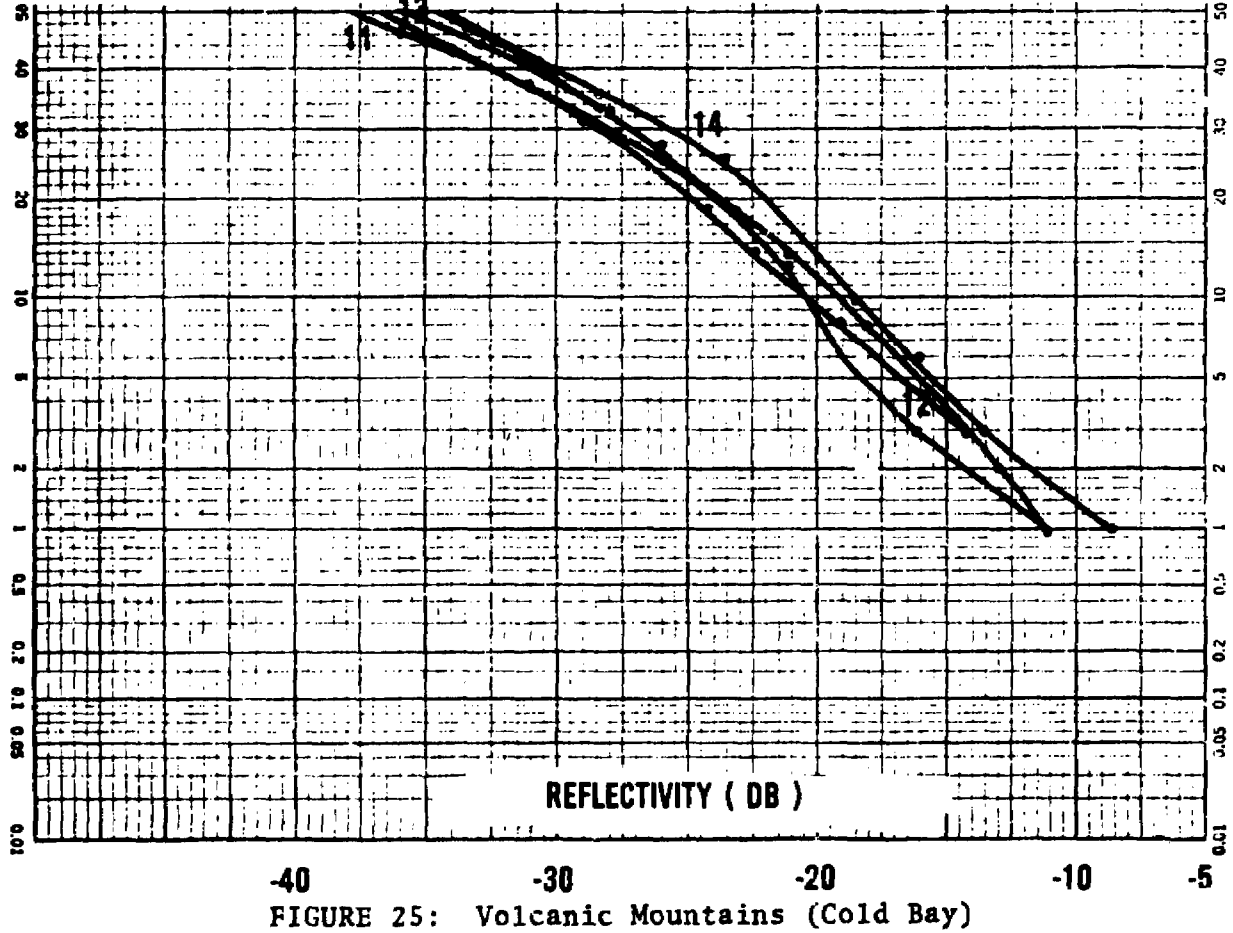

FIGURE 25: Volcanic Mountains (Cold Bay)

CURVE NO.	PLACE	DATE	τ usec	TERRAIN TYPE	AREA NO.
2	COLD BAY	14 SEPT	5.7	VOLCANIC MOUNTAINS	2
4	COLD BAY	14 SEPT	5.7	VOLCANIC MOUNTAINS	2
6	COLD BAY	14 SEPT	3.0	VOLCANIC MOUNTAINS	2
7	COLD BAY	14 SEPT	1.0	VOLCANIC MOUNTAINS	2
10	COLD BAY	15 SEPT	0.5	VOLCANIC MOUNTAINS	2

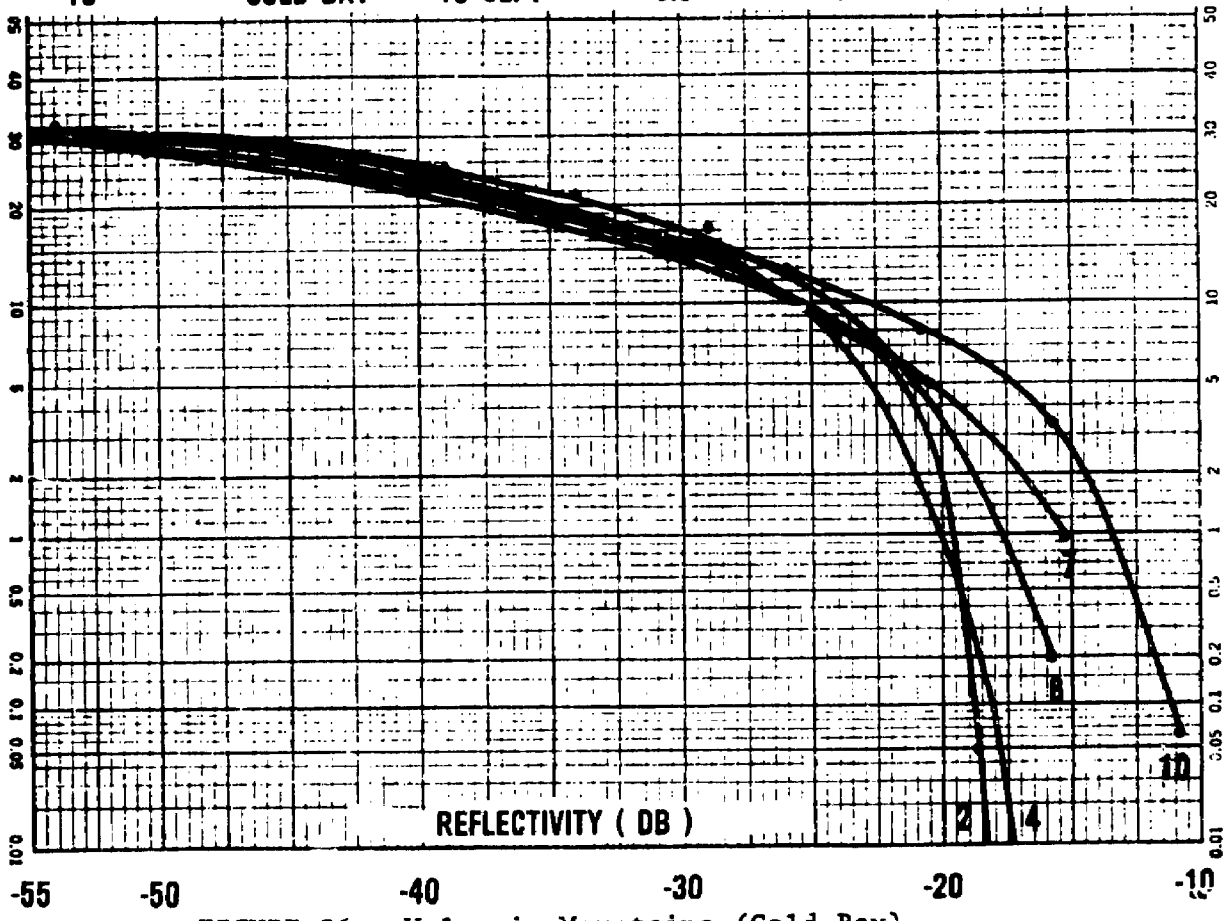

FIGURE 26: Volcanic Mountains (Cold Bay)

CURVE NO.	PLACE	DATE	τ usec	TERRAIN TYPE	AREA NO.
3	TATALINA	23 AUG	6	EVERYTHING	3
4	TATALINA	23 AUG	6	EVERYTHING	2

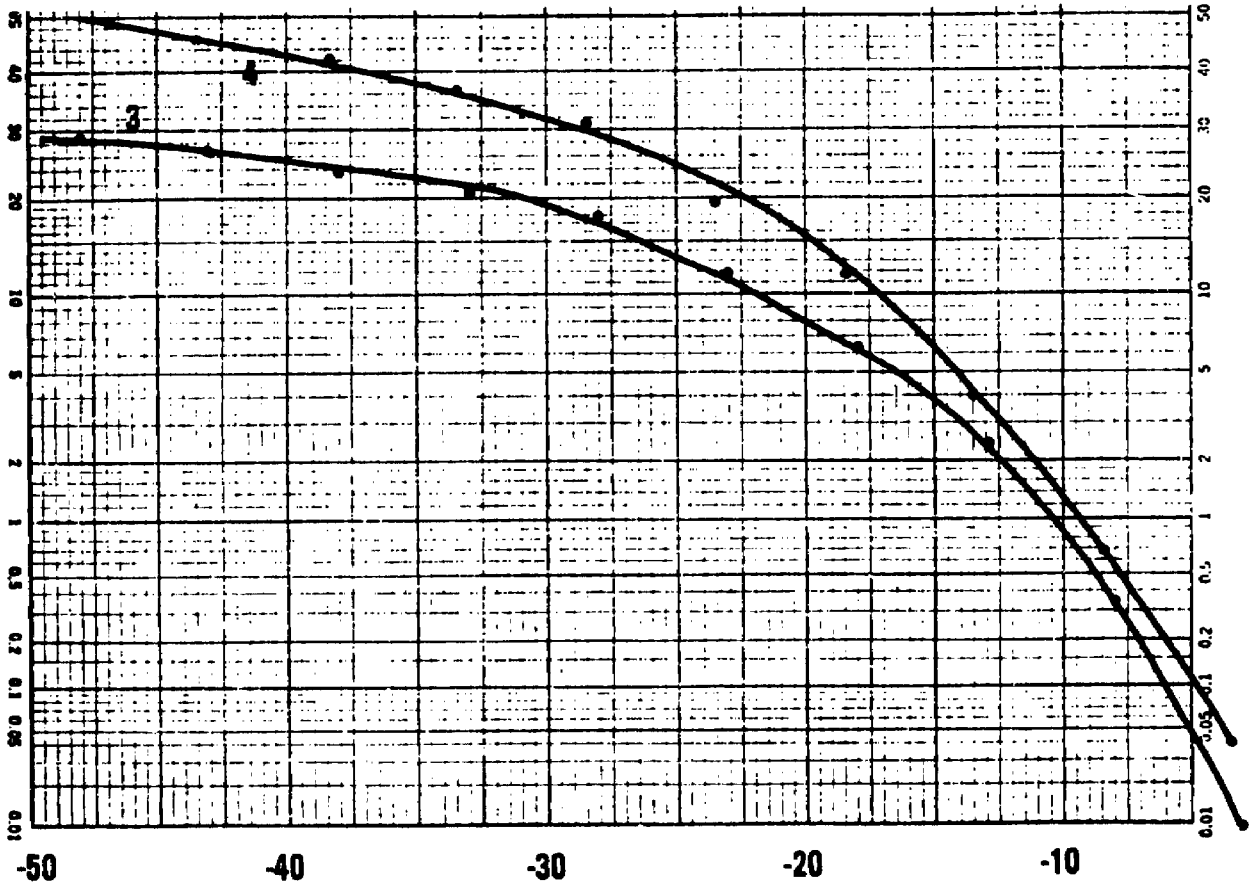

FIGURE 27: Composite Distributions (Tatalina)

CURVE NO.	PLACE	DATE	τ usec	TERRAIN TYPE	AREA NO.
5	TATALINA	24 AUG	3	EVERYTHING	3
6	TATALINA	24 AUG	1	EVERYTHING	3
7	TATALINA	24 AUG	0.5	EVERYTHING	3

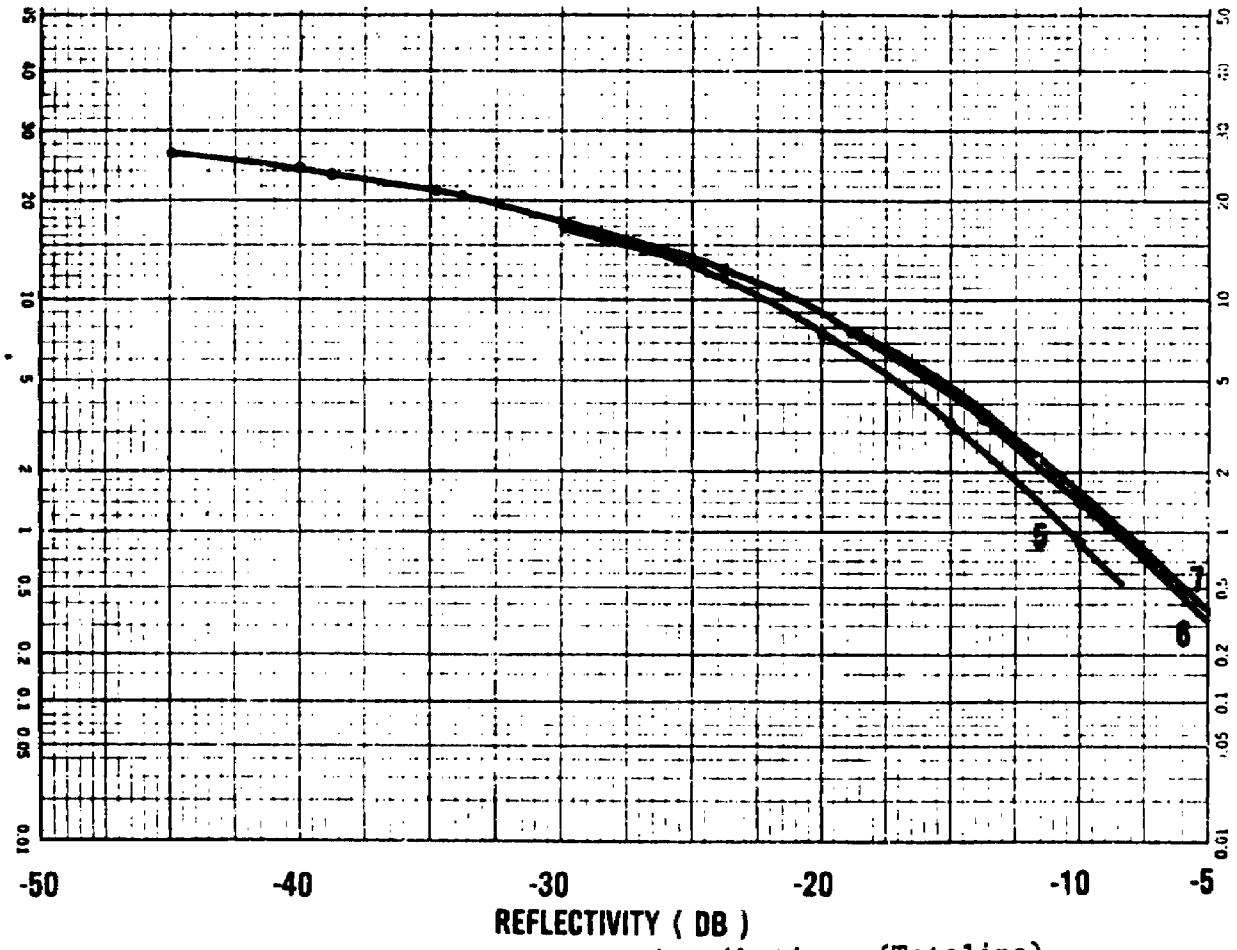

FIGURE 28: Composite Distributions (Tatalina)

CURVE NO.	PLACE	DATE	τ usec	TERRAIN TYPE	AREA NO.
12	TATALINA	25 AUG	6	HILLS	6
13	TATALINA	25 AUG	6	SWAMPS, RIVER BASINS	7
14	TATALINA	25 AUG	6	McKINLEY RANGE	8
15	TATALINA	25 AUG	6	LOW MTS/HIGH HILLS	9

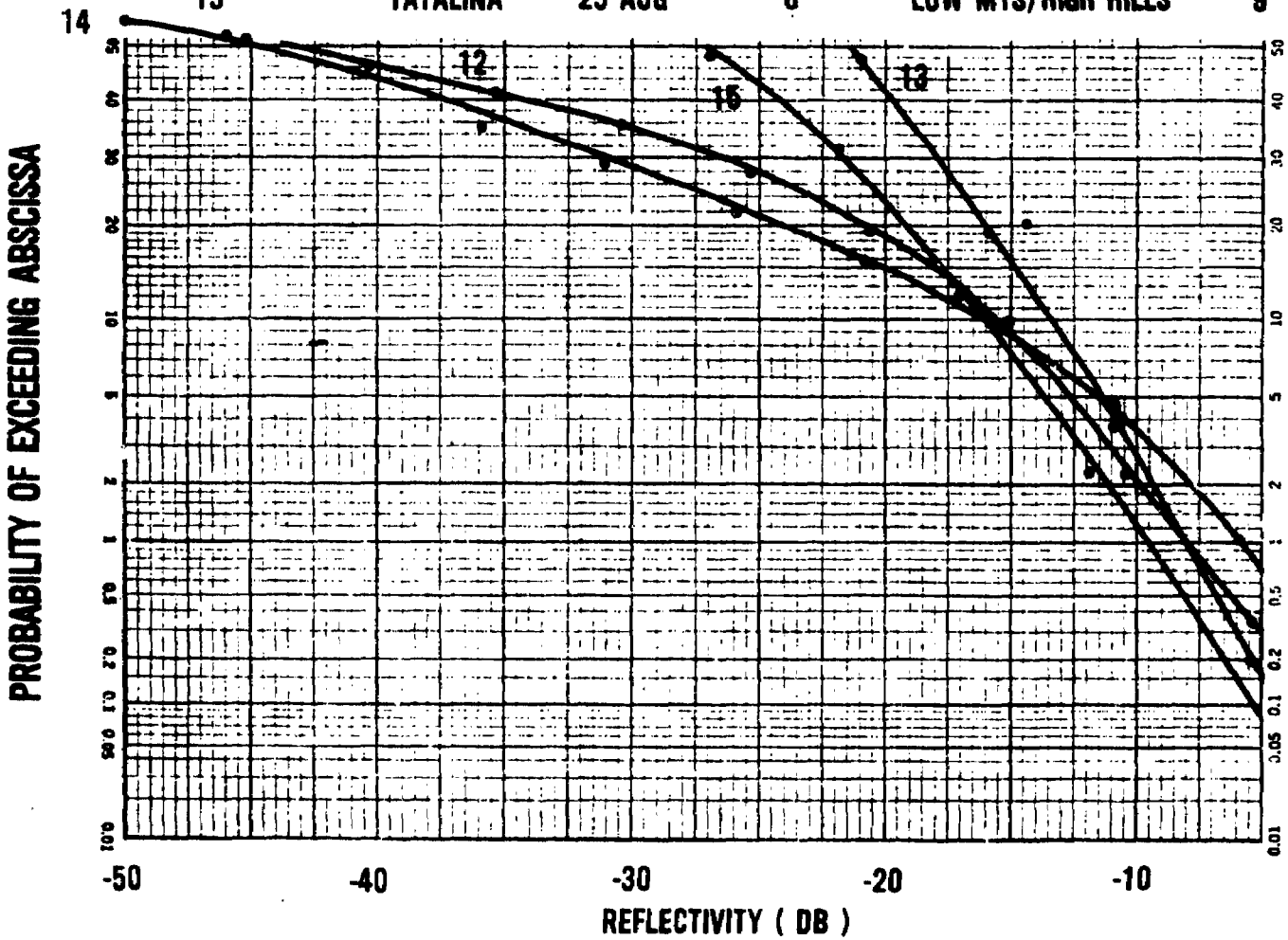

FIGURE 29: Comparative Distributions (Tatalina)

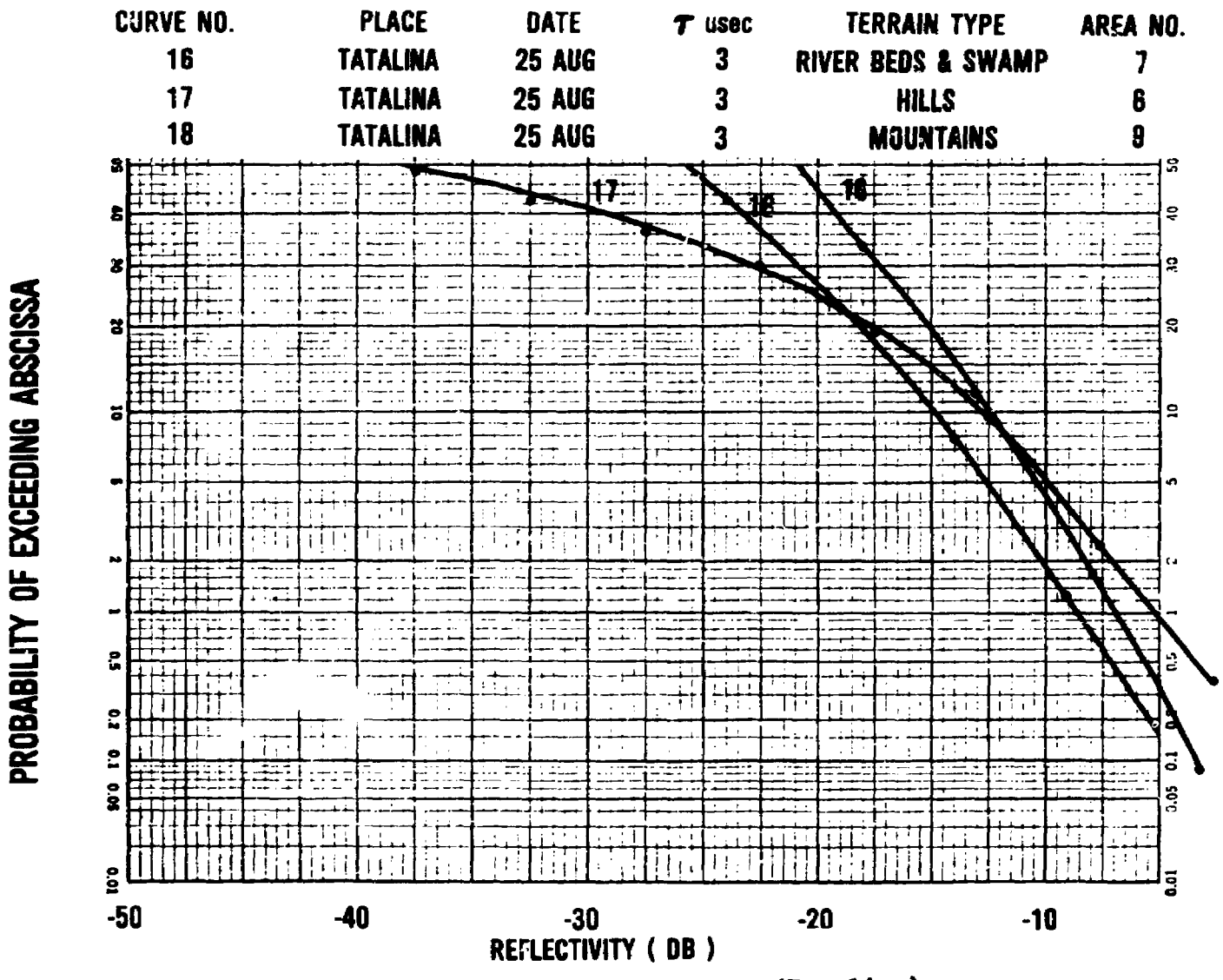

FIGURE 30: Comparative Distributions (Tatalina)

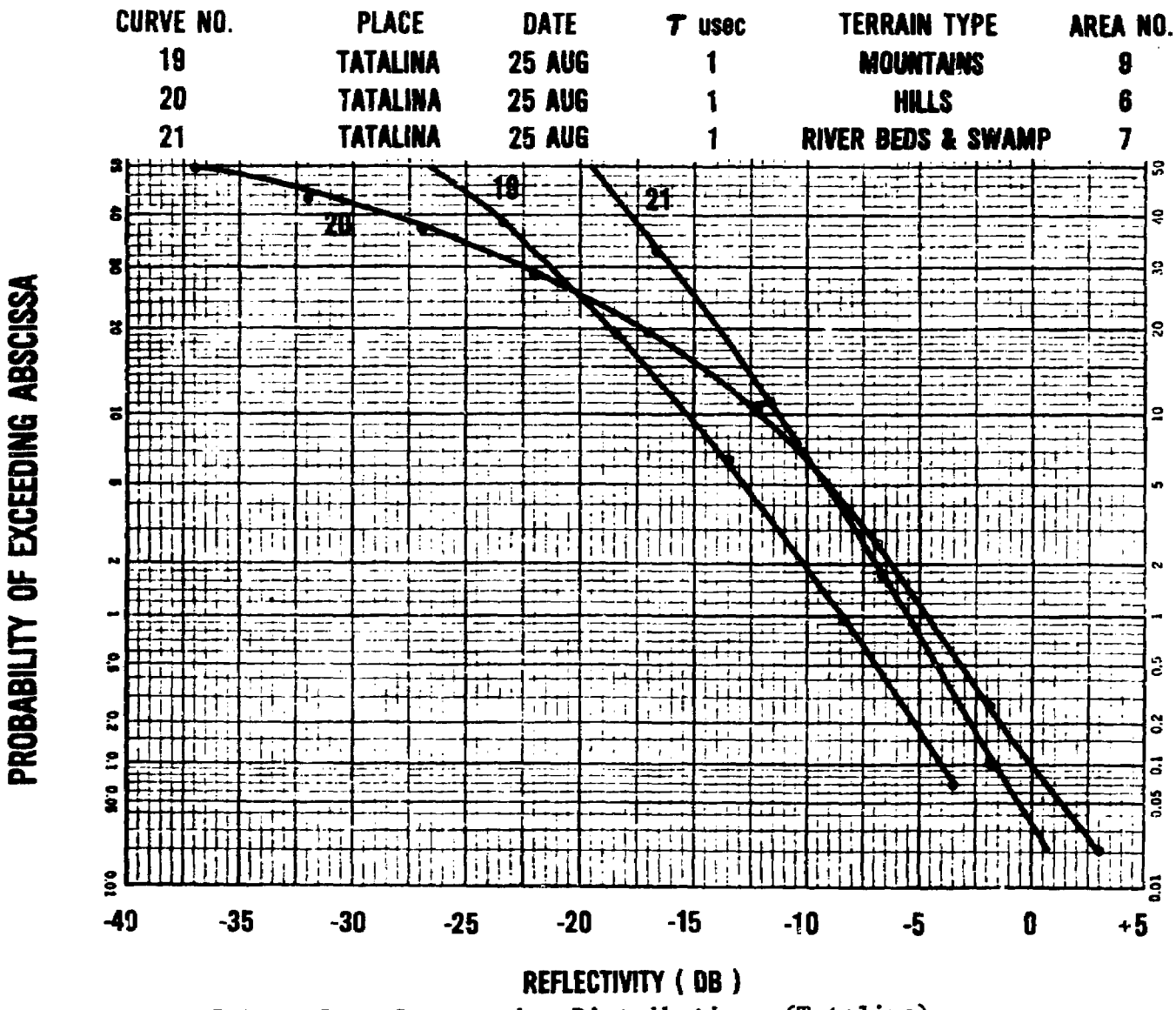

FIGURE 31: Comparative Distributions (Tatalina)

CURVE NO.	PLACE	-DATE	τ usec	TERRAIN TYPE	AREA NO.
22	TATALINA	25 AUG	0.5	MOUNTAINS	7
23	TATALINA	26 AUG	0.5	SWAMP	9
24	TATALINA	26 AUG	0.5	HILLS	6

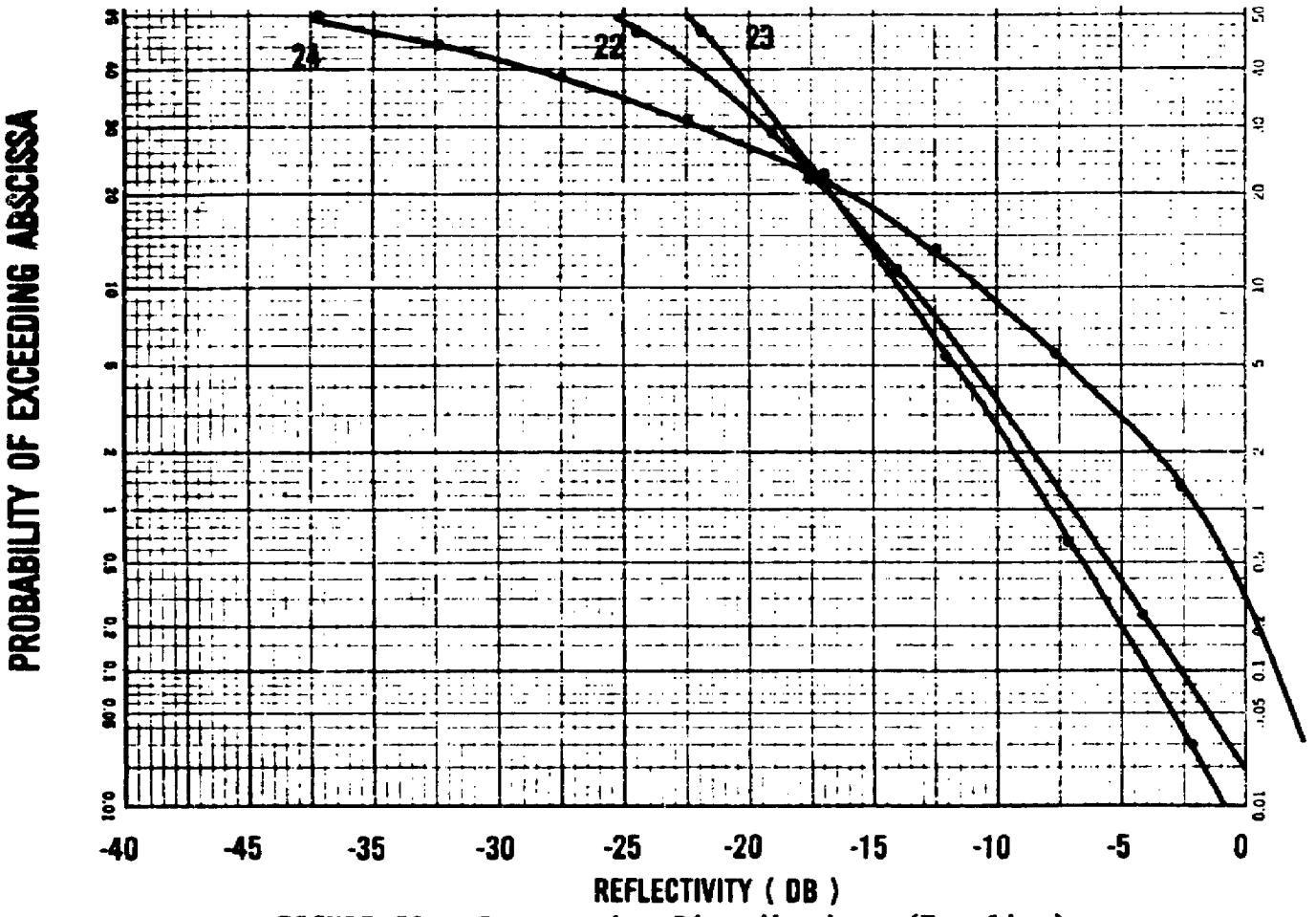

FIGURE 32: Comparative Distributions (Tatalina)

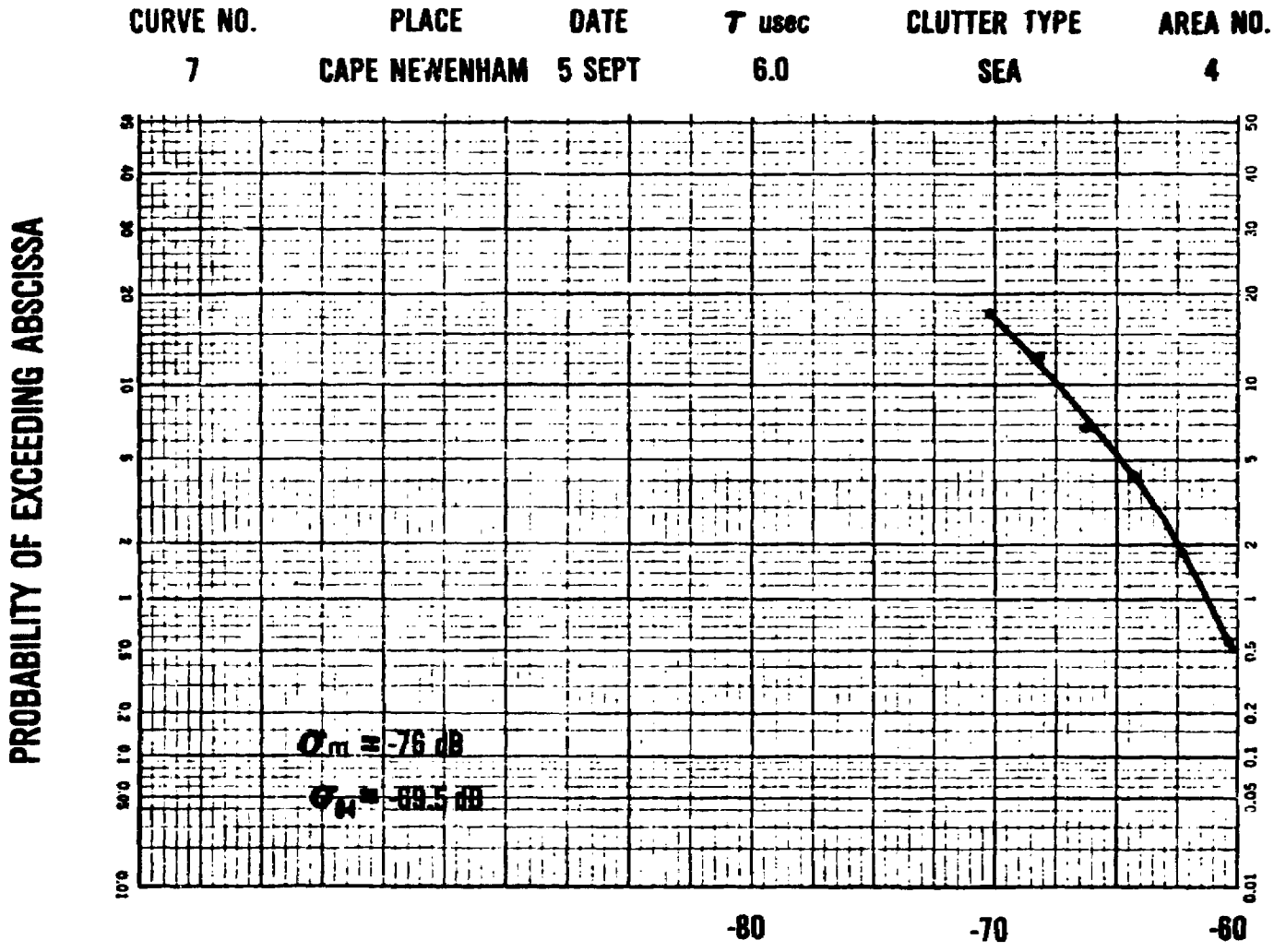

FIGURE 33: Sea Clutter (Cape Newenham)

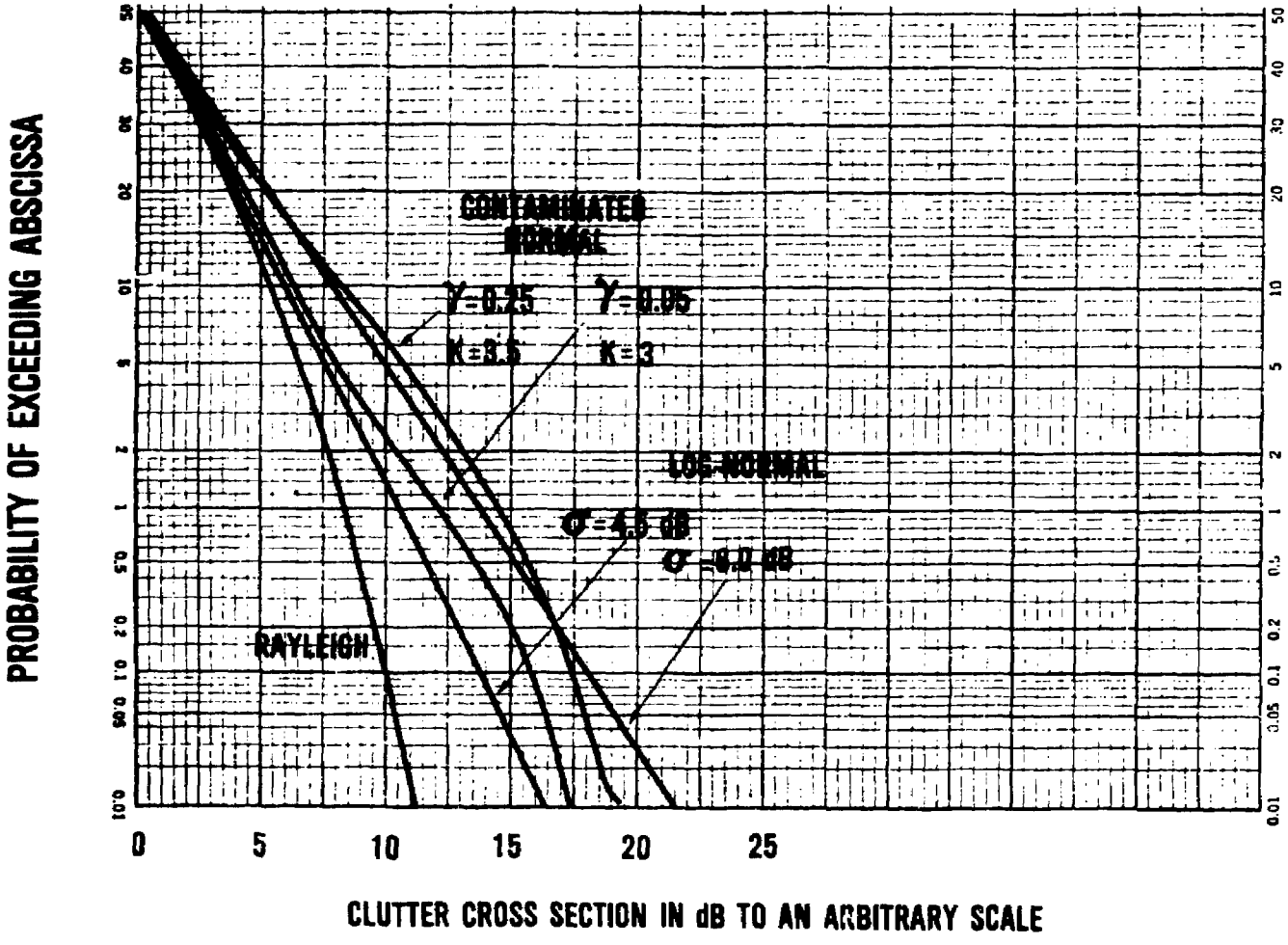

FIGURE 34: Comparison of Rayleigh, Log-Normal and Contaminated-Normal Distributions

V. SPECTRAL DENSITY MEASUREMENTS:

A. Terrain Clutter:

Measured spectral densities of land clutter returns are displayed in Photos 1 through 19. Photos 1 - 3 give a typical spectral density for mountains and the worst measured cases for partially-wooded hills and heavily-wooded valleys. For use in radar design, an attempt was made to describe or bound the worst case two-sided clutter spectra with idealized models defined by a DC impulse and a smooth AC function.

$$P_2(f) = A\delta_\varepsilon(f) + B\,G(f)$$

For mathematical convenience, the DC impulse is defined as

$$\delta_\varepsilon(f) = \frac{1}{\varepsilon}\,\pi\left(\frac{f}{\varepsilon}\right)$$

where $\pi\left(\frac{f}{\varepsilon}\right) \triangleq \begin{cases} 1, & |f| < \frac{\varepsilon}{2} \\ 0, & |f| > \frac{\varepsilon}{2} \end{cases}$

ε = normalizing bandwidth

In determining the DC impulse component, several assumptions were used. First, although the spectrum analyzer was DC coupled, it did not display DC. Therefore, all land clutter measurements were performed with the peak energy of each return adjusted to within 3 dB of the maximum input. Then, the energy within the filter centered at zero frequency was approximated by

$$V_{DC}^2 \simeq \left(1 - \int_{\Delta f}^{\frac{PRF}{2}} |V(f)|\,df\right)^2$$

Photo 1

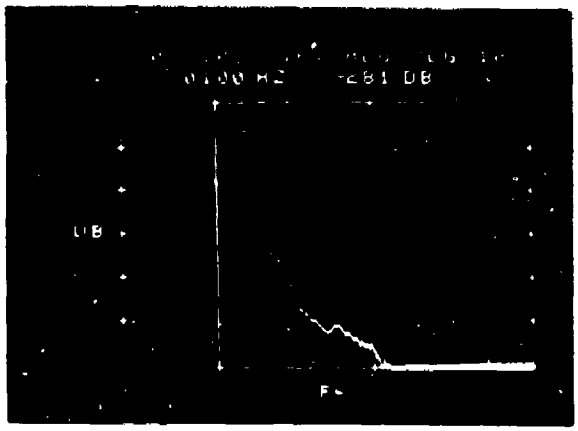

SPECTRAL RETURN FROM MOUNTAINS (TYP)

Photo 2

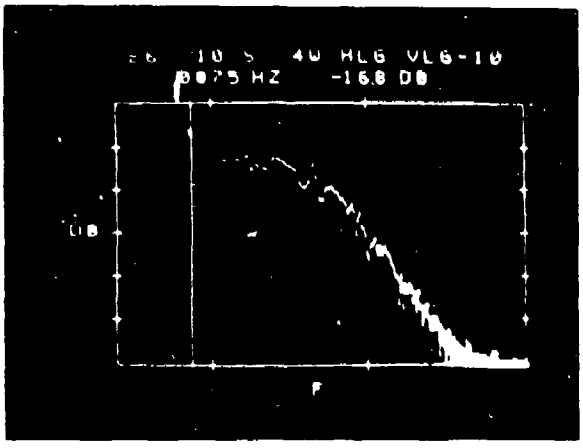

SPECTRAL RETURN FROM HILLS (WORST CASE)

Photo 3

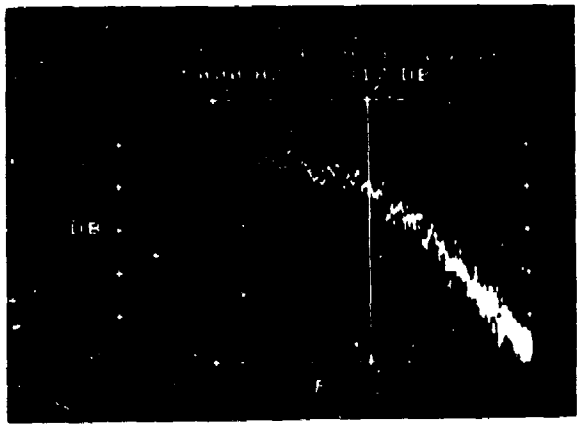

SPECTRAL RETURN FROM VALLEYS (WORST CASE)

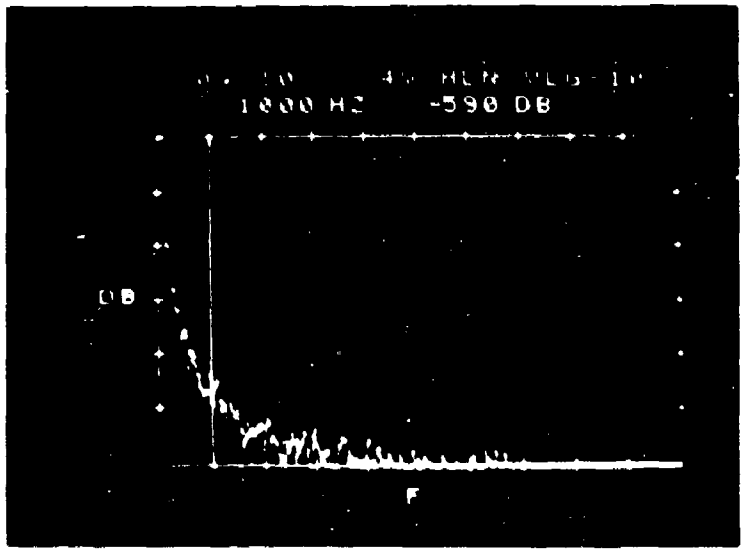

MOUNTAINS

Photo 4

Photo 5

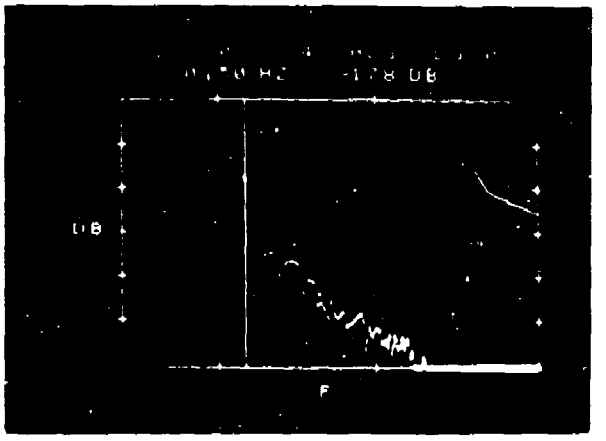

Photo 6

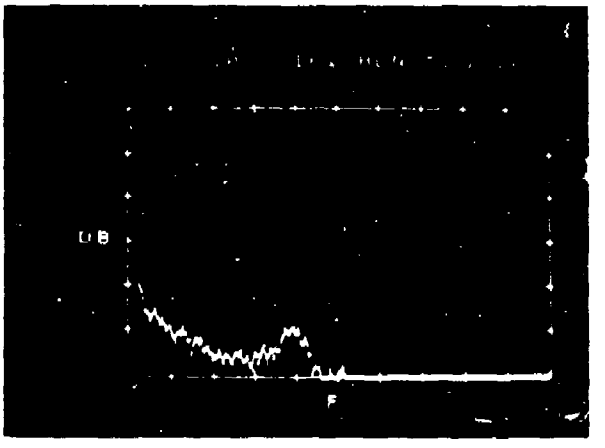

Photo 7

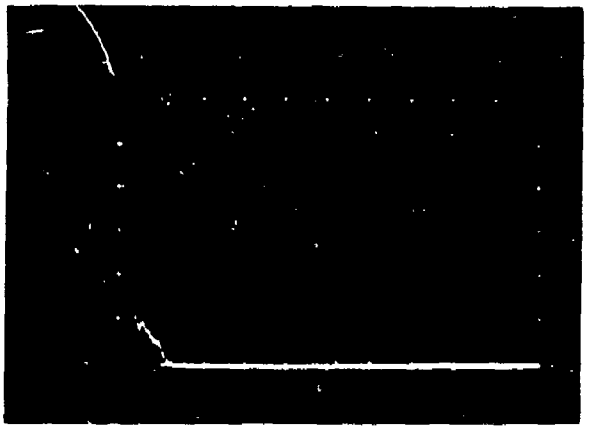

MOUNTAINS

Photo 8

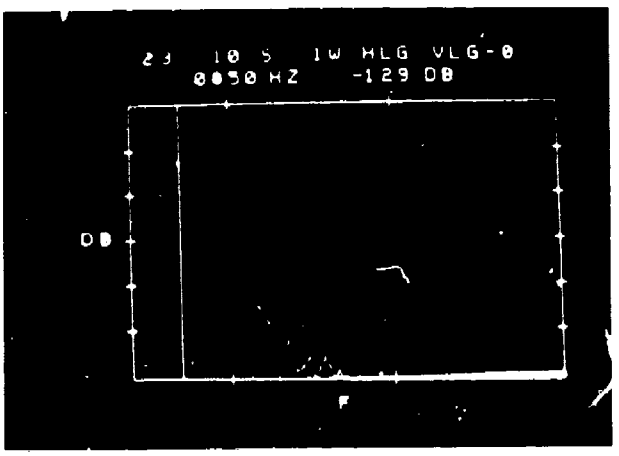

Photo 9

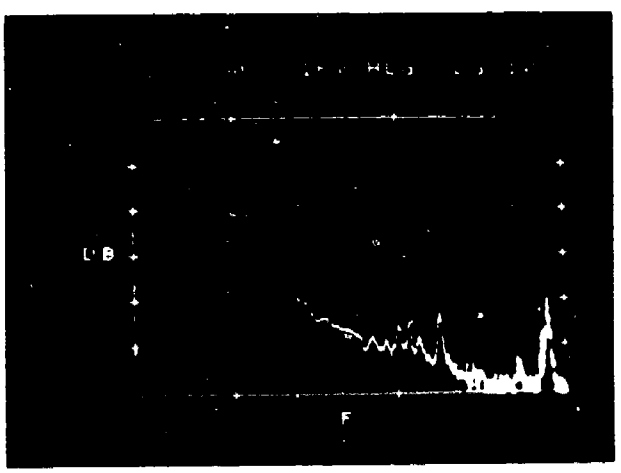

Photo 10

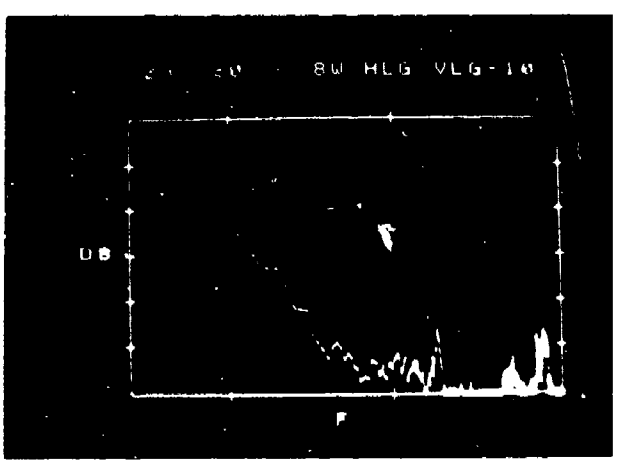

MOUNTAINS

Photo 11

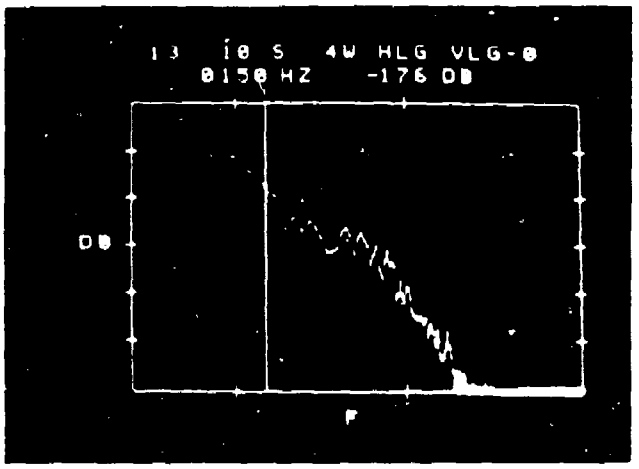

Photo 12

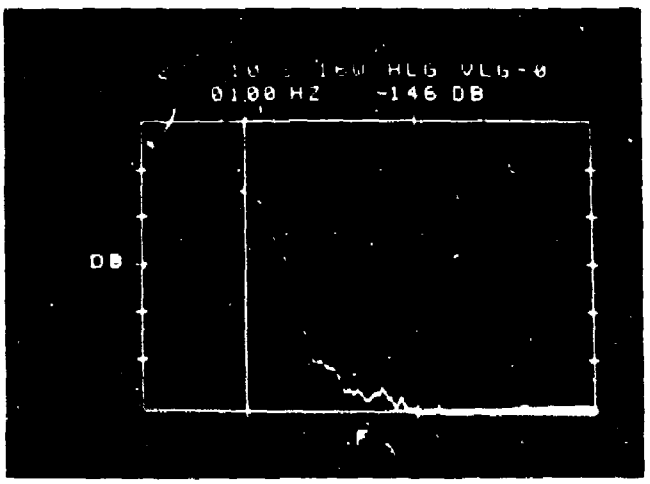

Photo 13

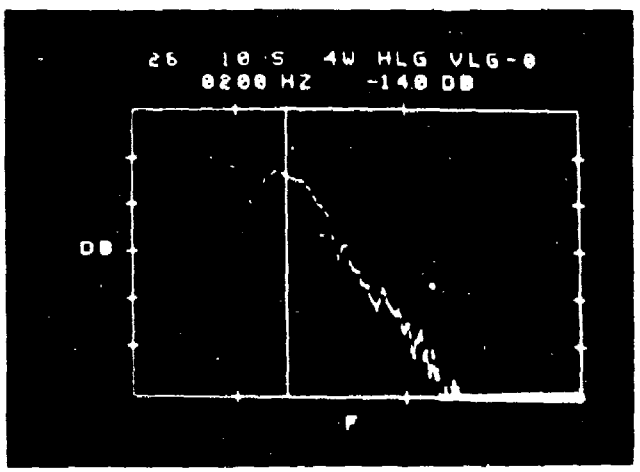

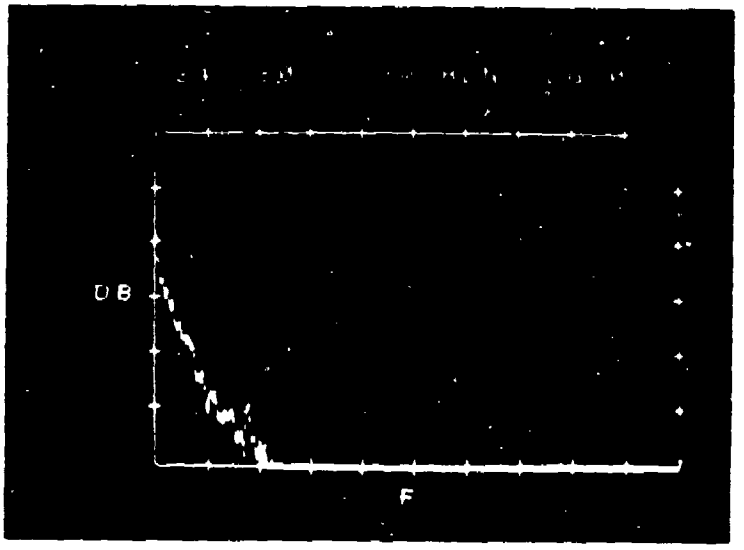

HILLS

Photo 14

Photo 15

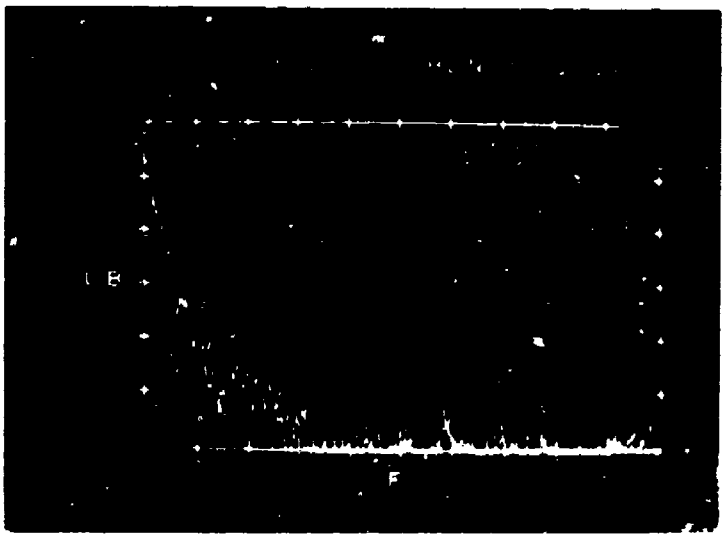

Photo 16

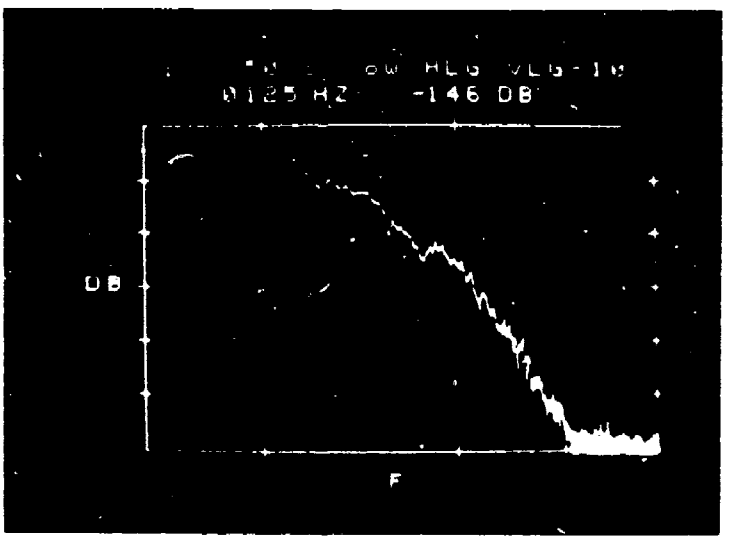

VALLEYS

Photo 17

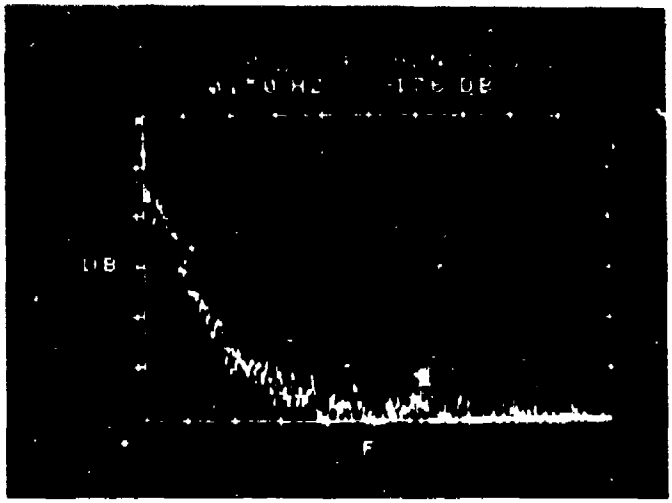

Photo 18

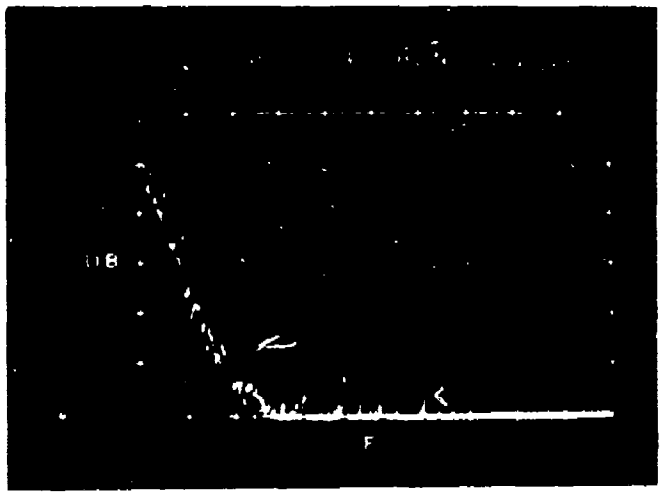

Photo 19

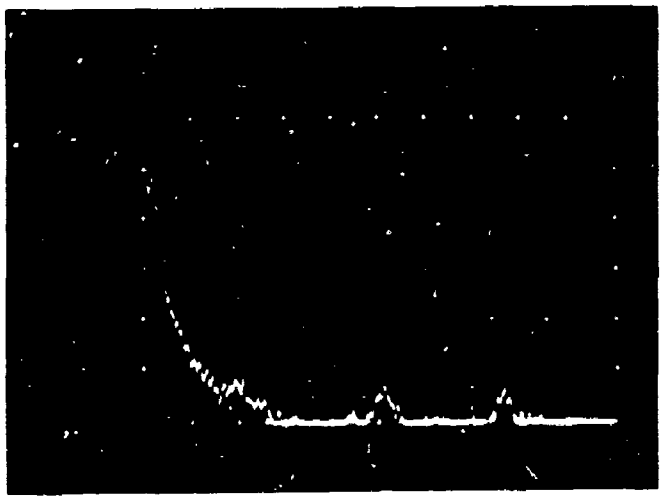

VALLEYS

where Δf = center frequency of the lowest frequency filter.

Secondly, the spectrum analyzer internally compensated for spectra amplitude when integration times were changed. Therefore, to allow a point-by-point comparison between the spectra oscillographs and plot ideal functions, the normalizing bandwidth was set at $\varepsilon = .025$ (the narrowest filter of the spectrum analyzer) and the total energy was normalized to

$$\int_{-\infty}^{\infty} P_2(f)df = .025$$

Finally, the measured spectral spread of fixed point targets was used to define the resolution of the measurement system. Since this resolution, which varied from .05 to .25 Hz, was often much larger than the .025 Hz resolution possible with the spectrum analyzer, the DC coefficient, A, would depend on the choice of two-sided DC filter bandwidth B_f. Therefore, Photos 1 - 3 were graphically analyzed to obtain a DC-to-AC ratio a^2 where

$$a^2 = \frac{V^2_{DC} + \int_{\Delta f}^{f_1} V^2(f)df}{\int_{f_1}^{\frac{PRF}{2}} V^2(f)df}$$

$$f_1 = \frac{B_f}{2}$$

Figure 35 presents a^2 versus filter width B_f for each photograph. The DC coefficient A can now be given as

$$A = \frac{a^2(.025)}{1 + a^2}$$

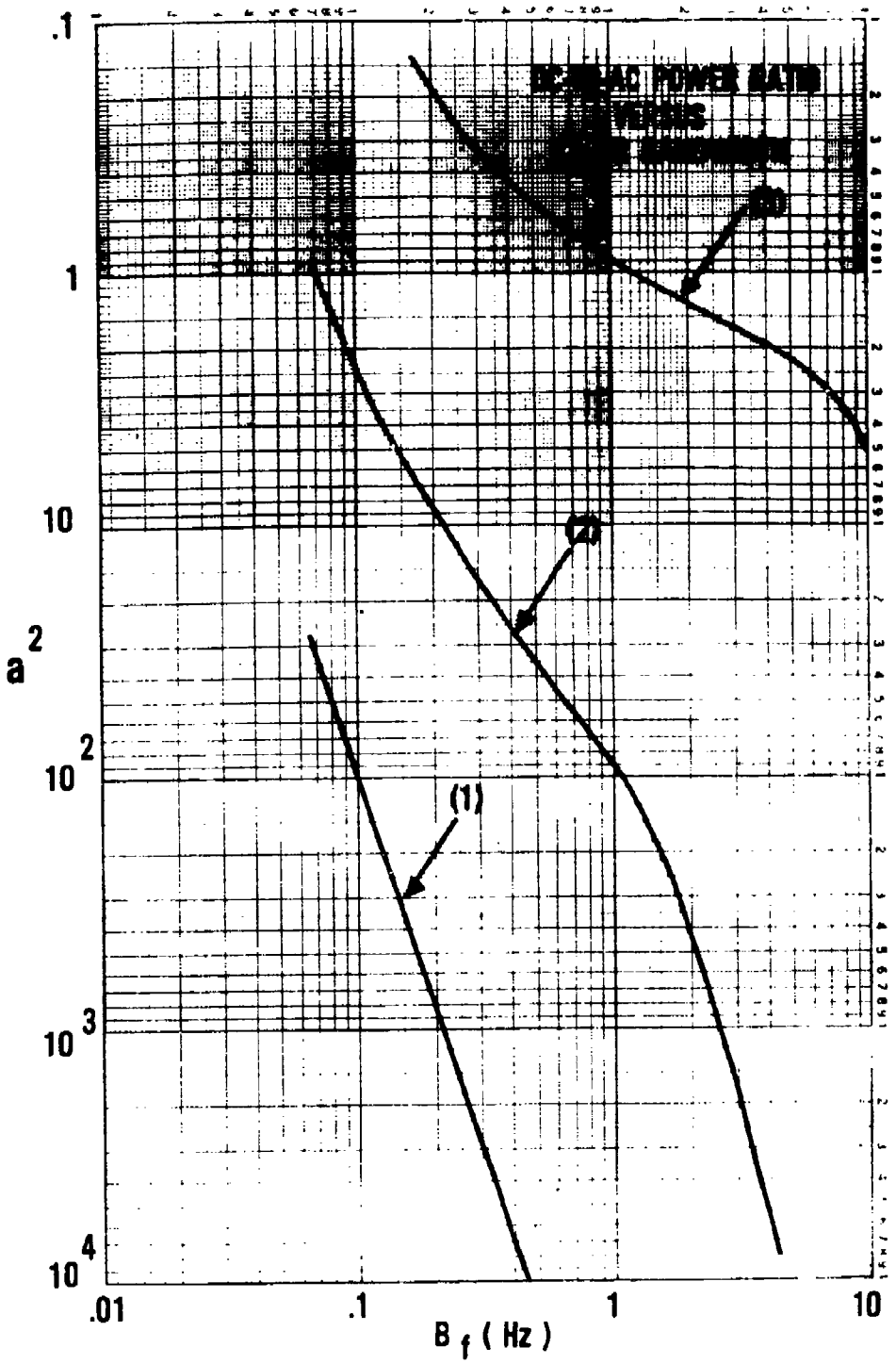

FIGURE 35: DC-To-AC Power Ratio
(of Worst Case Land Clutter Spectra)
Versus Filter Bandwidth

The high frequency tails were compared graphically with several standard functions. The Gaussian function, suggested by several radar publications, did not adequately describe the high frequency tails. Instead, a more descriptive function is of the form[5]

$$G(f) = \frac{1}{1 + \left(\frac{f}{f_c}\right)^N}$$

where N = a constant

f_c = -3 dB frequency.

The AC coefficient B can be given as

$$B = \frac{.025}{(1 + a^2)\ E}$$

where a^2 = DC-to-AC power ratio

$$E = \int_{-\infty}^{\infty} G(f)\,df$$

Descriptive or bounding spectral density functions for mountains, partially-wooded hills, and densely-wooded valleys are given in Figures 36 and 37. The typical return from mountains (peaks over 4,000 ft) in 10 - 20 knot winds is given by plot 1 (Δ). The shape of the measured spectral densities from mountains was uncertain due primarily to the unknown instability of the radar. However, the measured one-sided spectral density P_1(1 Hz) was always less than -50 dB relative to the maximum energy and typically less than -60 dB. A conservative two-sided spectral density which

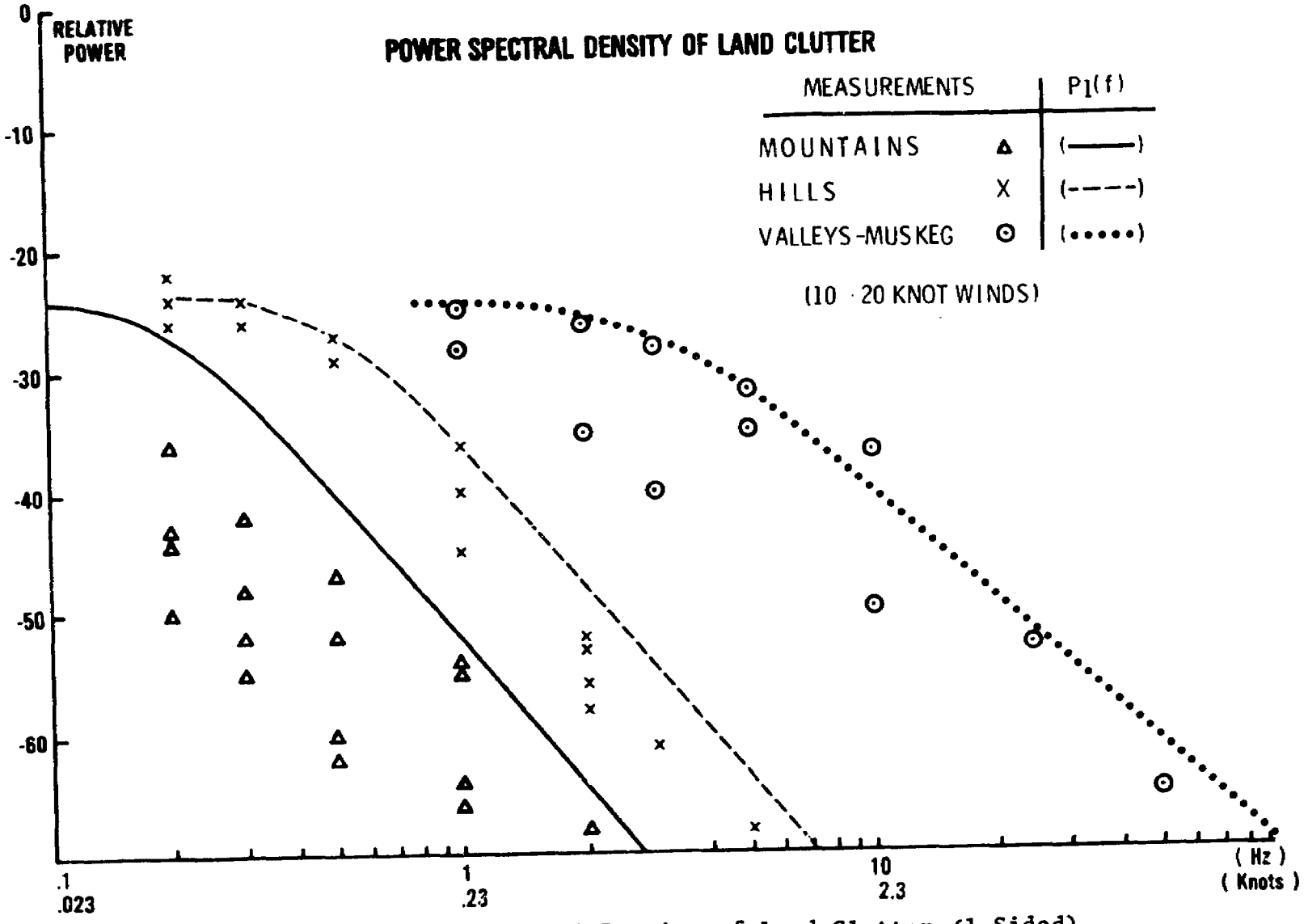

FIGURE 36: Power Spectral Density of Land Clutter (1-Sided)

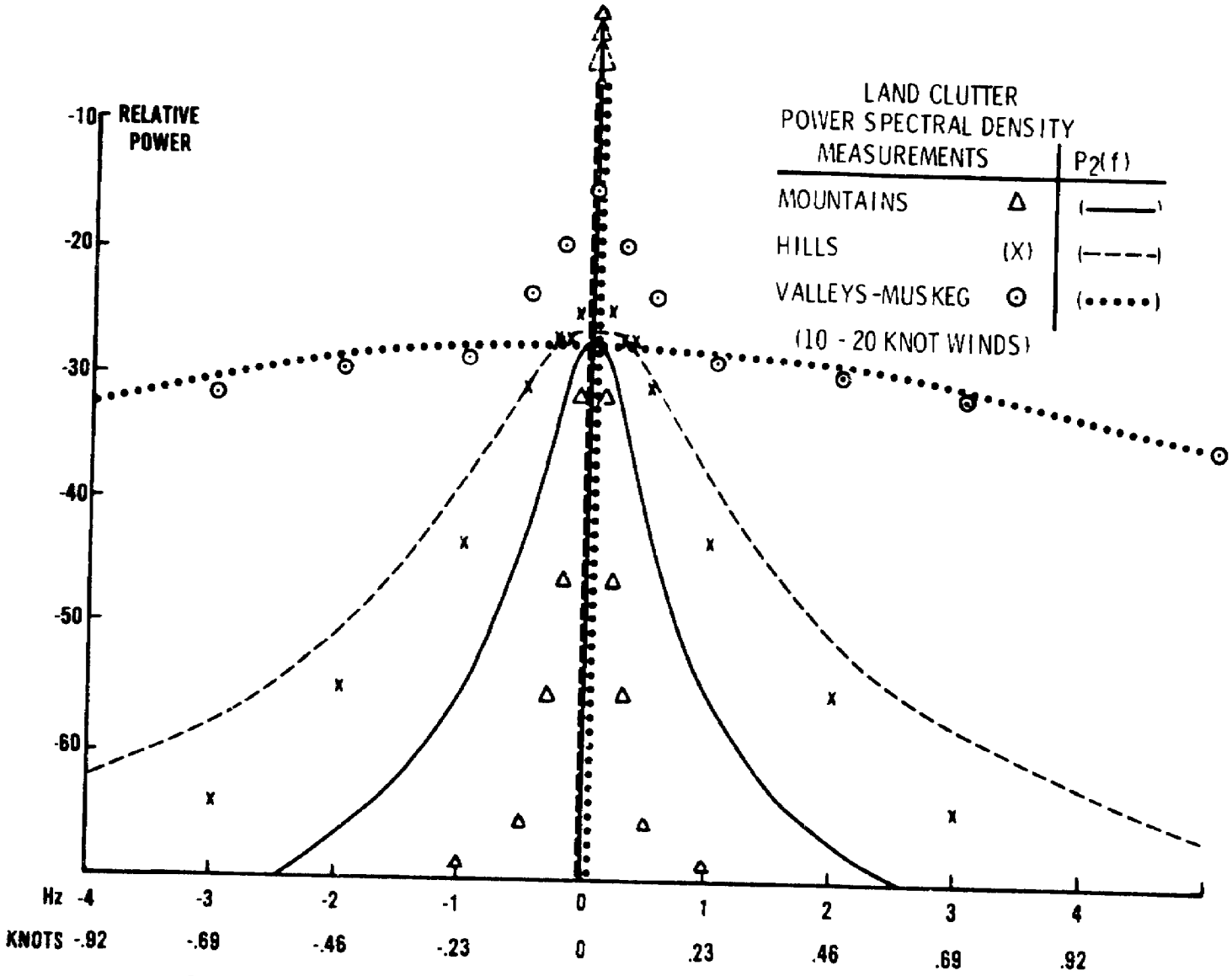

FIGURE 37: Power Spectral Density of Land Clutter (2-Sided)

bounds the observed values for mountains is

$$P_{2M}(f) = 0.964\Pi \left(\frac{f}{.025}\right) + \left(\frac{0.002}{1 + \left(\frac{f}{.2}\right)^4}\right)$$

where $B_f = .067$ Hz

$a^2 = 27$

$\int_{-\infty}^{\infty} G(f)df = 2.22\ f_c$

$f_c = .2$ Hz

The worst case spectra measured from partially-wooded hills (peaks between 1,000 and 4,000 feet) in 10 - 20 knot winds is given by plot 2 (X). The spectra from this terrain type had a narrow peak around the carrier and tails that decay as f^{-3} to f^{-5}. A conservative two-sided spectral density for partially-wooded hills is

$$P_{2H}(f) = .9\ \Pi \left(\frac{f}{.025}\right) + \left(\frac{0.00225}{1 + \left(\frac{f}{.5}\right)^4}\right)$$

where $B_f = .2$ Hz

$a^2 = 9$

$\int_{-\infty}^{\infty} G(f)df = 2.22\ f_c$

$f_c = .5$ Hz

The worst case spectra measured from densely-wooded valleys and hillsides (below 1,000 feet) in 10 - 20 knot winds is given by plot 3 (θ). The spectra had a broad peak about the carrier with

significant tails decaying as f^{-3} to f^{-5} and extending beyond 10 Hz. A conservative two-sided spectral density of the form

$$P_{2V}(f) = 0.46\,\Pi \left(\frac{f}{.025} \right) + \left(\frac{0.00186}{1 + \left(\frac{f}{3} \right)^3} \right)$$

(total normalized power = .025)

could be used for wooded valleys where

$B_f = 1$ Hz

$a^2 = .85$

$\int_{-\infty}^{\infty} G(f)df = 2.42\, f_c$

$f_c = 3$ Hz

B. Sea Clutter:

Of the few sea clutter spectra recorded, Photos 20 - 22 present the worst case sea clutter spectra. The mean doppler is at approximately 28 Hz (6.4 knots) and the 3 dB width is 19 Hz (4.4 knots). The locally measured wind conditions were 10 knots average at the 11th Weather Squadron Station and 15 - 20 knots, gusting to 25 knots, at the radar site. Assuming that locally measured wind conditions do represent the wind conditions at the measured range-azimuth cell[a], a comparison of the measured spectra with values given in the radar literature leads to the following observations:

1. The spectral shape compares favorably with the

[a]It is recognized that local wind conditions do not, in general, describe the wind conditions several miles away.

Photo 20

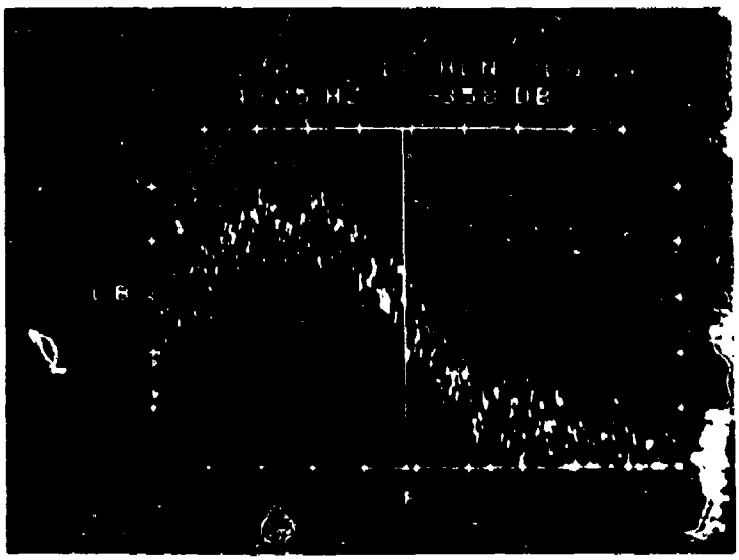

Photo 21

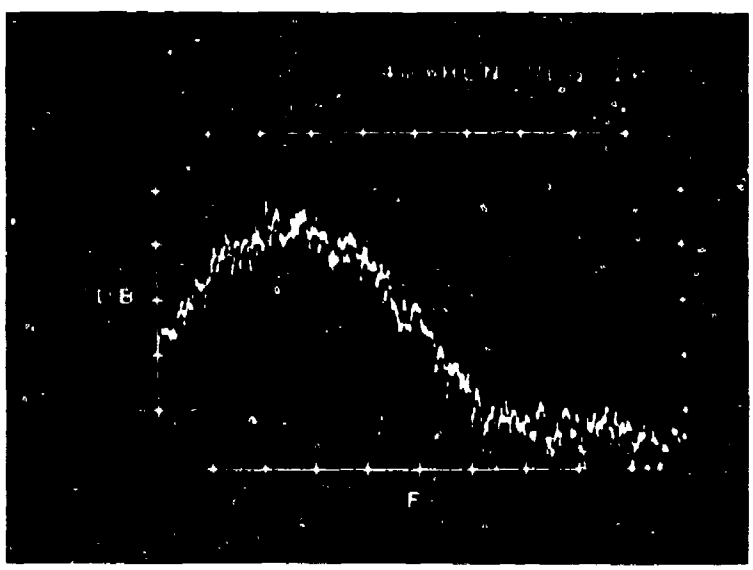

SEA CLUTTER

Photo 22

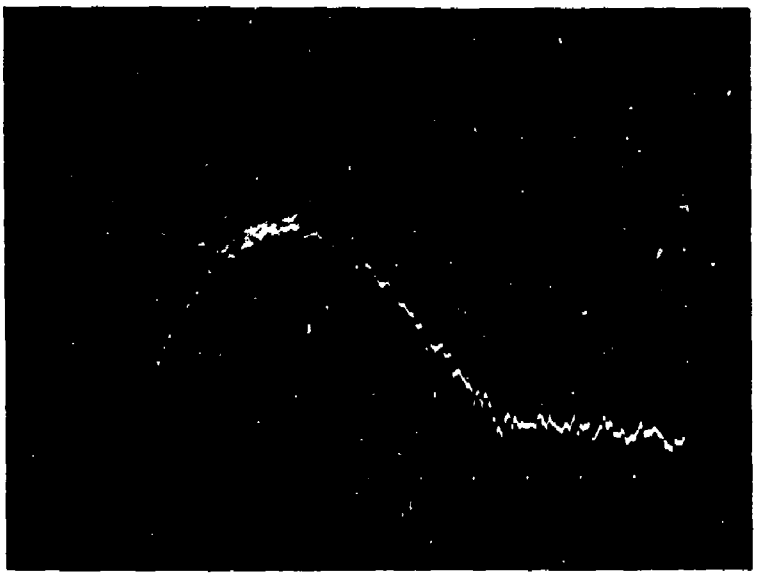

SEA CLUTTER WITHIN 20 NM (WORST CASE)

Photo 23

SEA CLUTTER BEYOND 20 NM (TYP)

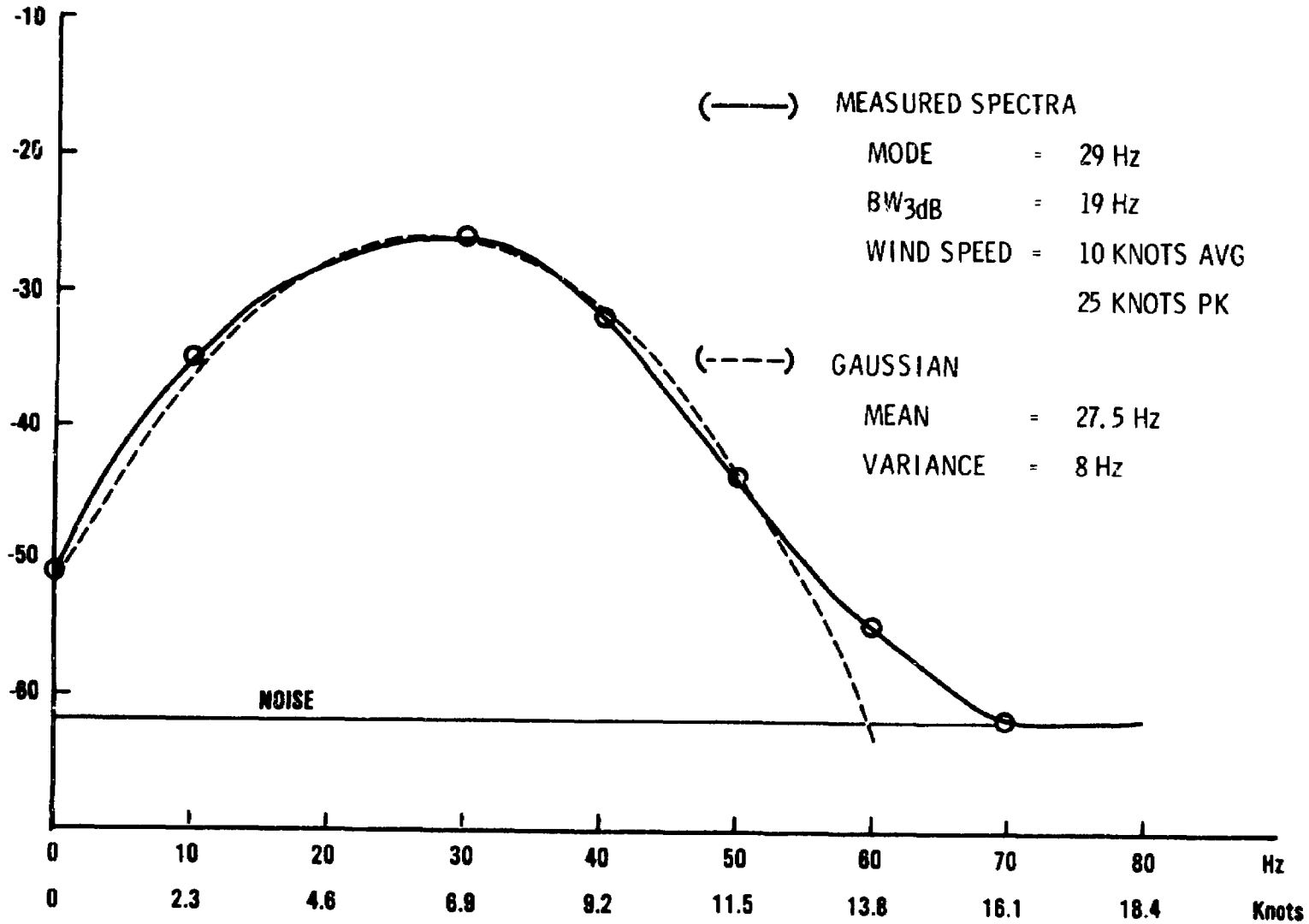

FIGURE 38: Sea Clutter Power Spectral Density

Gaussian shape often suggested (Figure 38).

2. The spectral width compares favorably with other experiment results taken under similar wind conditions.

3. The mean doppler was 1 - 2 knots higher than other published measurements and corresponded to wind speeds of over 40 knots.[6]

4. The measurement intervals of Photos 20 - 22 are 4, 10, and 34 seconds respectively, showing little change in spectral shape over these integration intervals.

Beyond approximately 20 nautical miles from the shore, an additional spectral component was noticed (Photo 23). Less than 5 Hz wide but having a maximum doppler of at least 70 Hz (16 knots), this component may have been generated by large ocean swells or gravity waves.

C. Weather Clutter:

Measured precipitation doppler spectra are given in Photos 24 thru 37. Most of the precipitation doppler spectra recorded in the clutter study were taken at Cold Bay during a gale. Surface observations taken during the measurements indicated rainfall rates of up to 8 mm/hour at Cold Bay and over 28 mm/hour at Fort Yukon. Radiosonde data taken within 48 hours of the measurement period at Cold Bay indicated cloud decks (relative humidity >60%) of 10,000

to 16,000 ft and average wind speeds of up to 42 knots within the cloud deck (see Table IV). Surface measurements indicated average wind speeds up to 36 knots with gusts to 44 knots.

TABLE IV: Measured Wind Velocities and Directions For Cold Bay Measurements

9 HOURS BEFORE MEASUREMENTS

HEIGHT (FT)	DEGREES	KNOTS
3700	165	42
8777	190	28
17154	235	36
22435	230	46

3 HOURS AFTER MEASUREMENTS

HEIGHT (FT)	DEGREES	KNOTS
3402	200	18
8396	205	30
16601	205	18
21753	215	30

Photos 24 thru 30 were taken at Fort Yukon during rainy and windy conditions. Photos 28 - 30 were taken within 5 minutes

of each other and show the relative backscatter of rain versus polarization. Rain backscatter using vertical polarization and circular polarization on transmit and receive were less than backscatter using horizontal polarization by approximately 8 and 13 dB respectively. (Observation of horizontal polarization of several minutes before and after this series was taken revealed little amplitude or frequency change of the spectra. Therefore, the difference in the three spectra is assumed to be due to polarization.)

Photos 31 - 37 were taken at Cold Bay[a]. Photos 36 and 37 give a good example of the spectral environment within 30 nautical miles of Cold Bay during the measurement period. Photo 36 is an averaged spectrum, taken over 3.6 second interval[b], of the backscatter from a range-azimuth cell over land at a range of 25 NM. Photo 37 is an instantaneous spectrum, taken over a 2 second interval[b], of the backscatter from a range-azimuth cell over the Bering Sea at a range of 20 NM.

[a]In reading the Cold Bay precipitation spectra photos, note that the radar pulse repetition frequency (PRF) was 244 Hz causing spectral foldover at 122 Hz.

[b]For "instantaneous" spectra, the analyzer requires a time interval T_i which can be given by $T_i(\text{secs})$ = 1024 samples/spectrum ÷ $(2.56)f_D$ where f_D = maximum display frequency.
For "averaged" spectra, the time interval T_A can be given by

$$T_A(\text{secs}) = T_i \times \left[1 + \frac{N - 1}{2} \right]$$

where N = number of spectra to be averaged.

Note that successive 50% redundant spectra are averaged.

Table V gives a comparison of several photos with values given by Nathanson[4]. Since some pictures were not symmetrical or Gaussian, a BW_{-3dB} and a BW_{-10dB} is given. Despite the long averaging time, a Gaussian function centered at the measured median values with a maximum equal to the mode values and having the standard deviations given by Nathanson bound all measured values.

D. False Alarms:

A table of false alarms for each site is given in Table VI. The three-pulse MTI canceller of the FPS-93A was calibrated with respect to velocity shape factor and cancellation by the ADC/AAC team. Then, using a PPI, the false alarms thru the MTI channel (without STC) were studied. Nearly all the studied false alarms were tracked several scans and moved measurable distances, thereby having the characteristics of targets rather than noise. These false alarms have been defined as angels. The number of false alarms were obtained by counting the number of false alarms in an average populated sector of 45° and multiplying by 8.

[4]Nathanson, F. E., Radar Design Principles, McGraw-Hill Book Co., Inc., New York, NY, 1969.

Avg. Time (sec)	Range (nm)	θ (deg)	$BW_{(-3dB)}$ (Knots)	$BW_{(-10dB)}$ (Knots)	Estimated Median (Knots)	Mode (Knots)	Wind Shear (Knots)
9	76	126	7	11	21	21	16.8
9	34	126	4	8	18	18	7.5
9	58	126	1.4	10	21	25	12.8
66	15	32	1.6	7	10.5	9	4.8
66	15	48	2	3.7	4	4	3.8

θ = degrees between wind direction and radar beam

Wind Shear = $|8.6R \not\varepsilon \cos\theta|$ Knots

$\not\varepsilon$ = maximum elevation angle intercepted by precipitation

TABLE V: Measured Precipitation Spectra

Photo 24

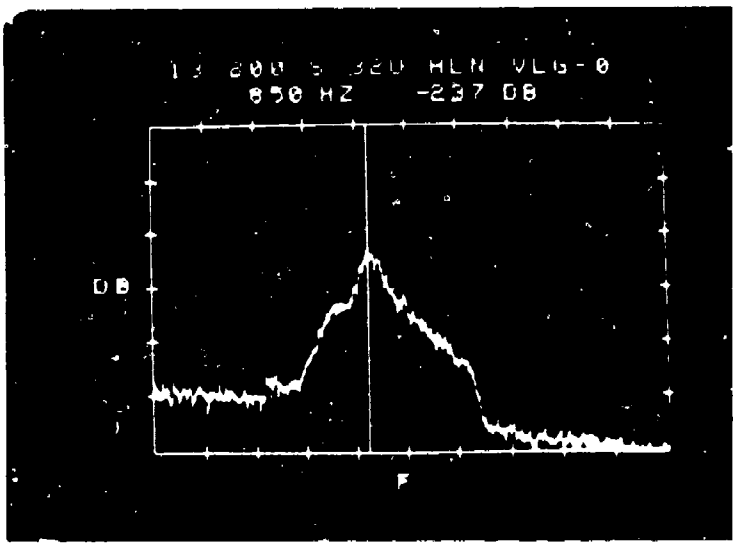

Photo 25

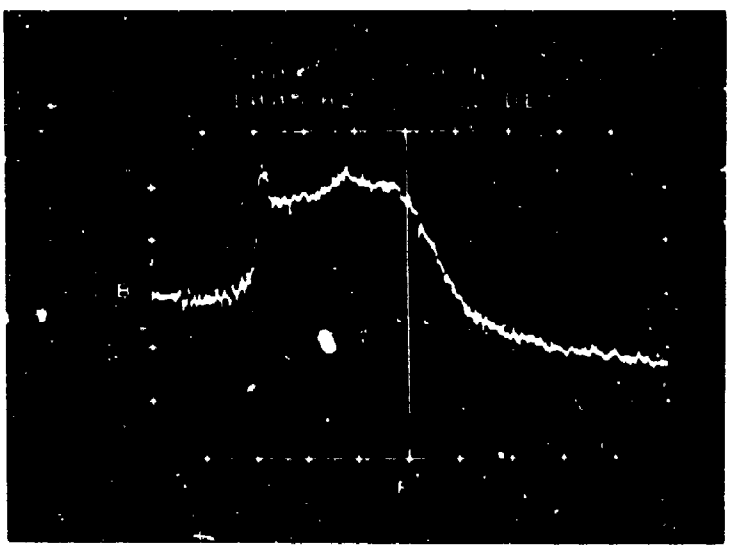

WEATHER CLUTTER

Photo 26

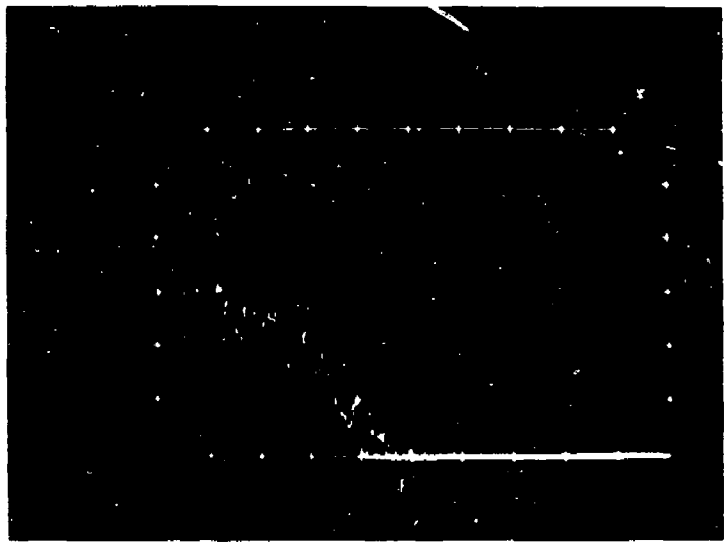

Photo 27

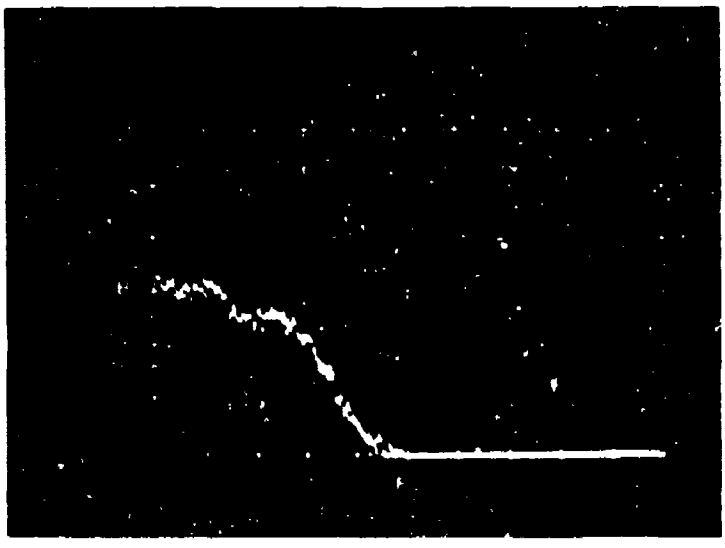

WEATHER

Photo 28

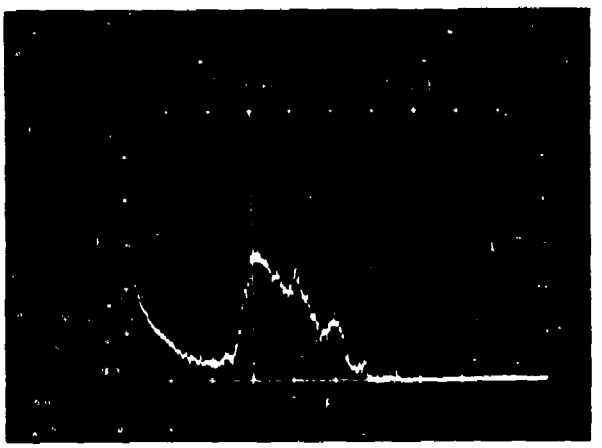

HORIZONTAL POLARIZATION

Photo 29

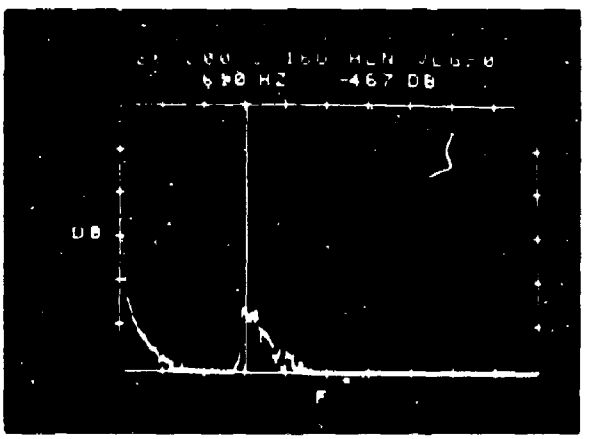

CIRCULAR POLARIZATION

Photo 30

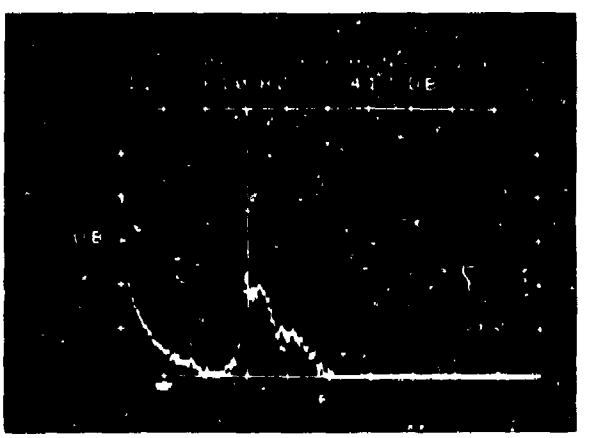

VERTICAL POLARIZATION

Photo 31

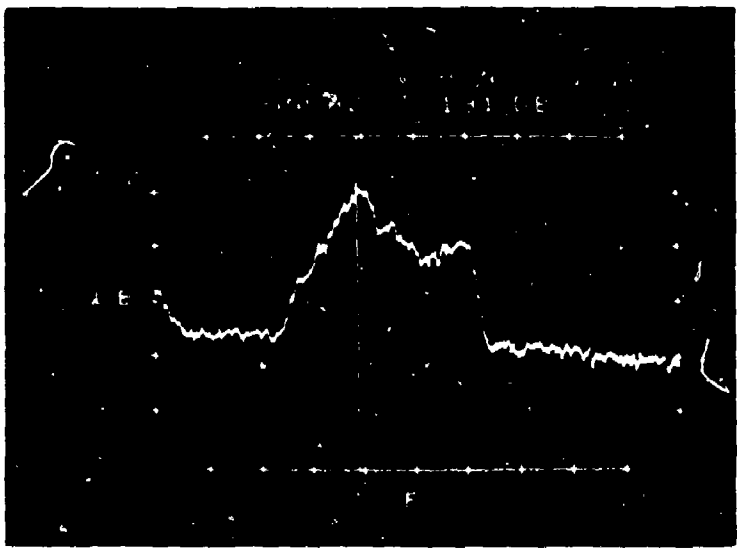

Photo 32

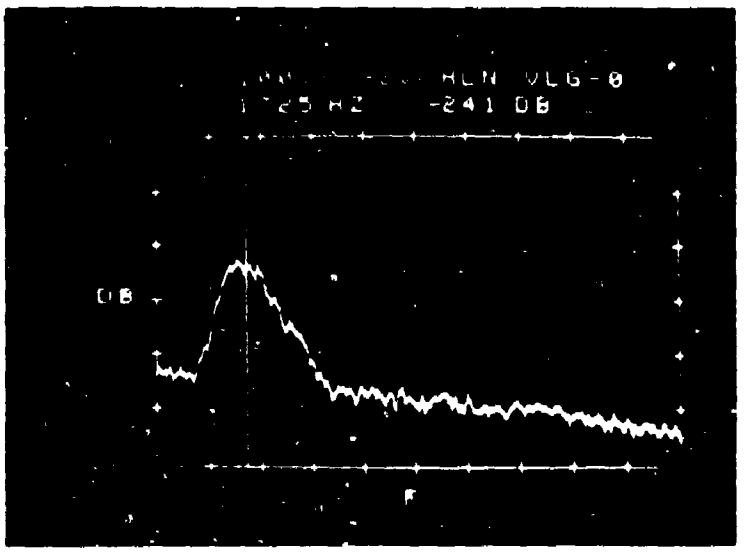

WEATHER CLUTTER

Photo 33

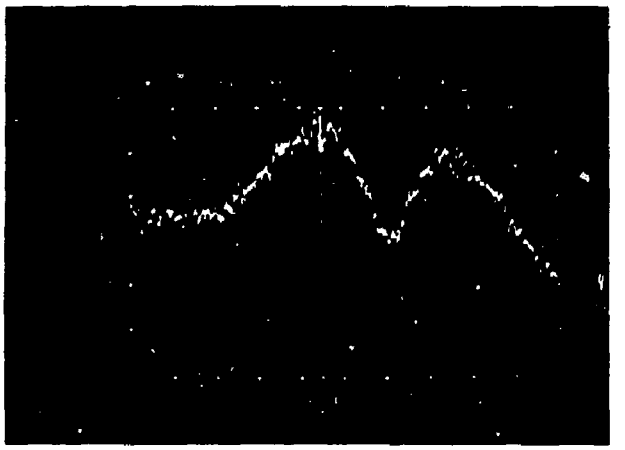

76 NAUTICAL MILES

Photo 34

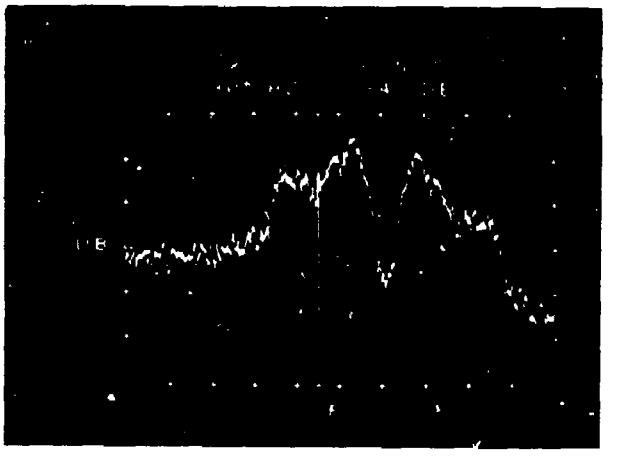

58 NAUTICAL MILES

Photo 35

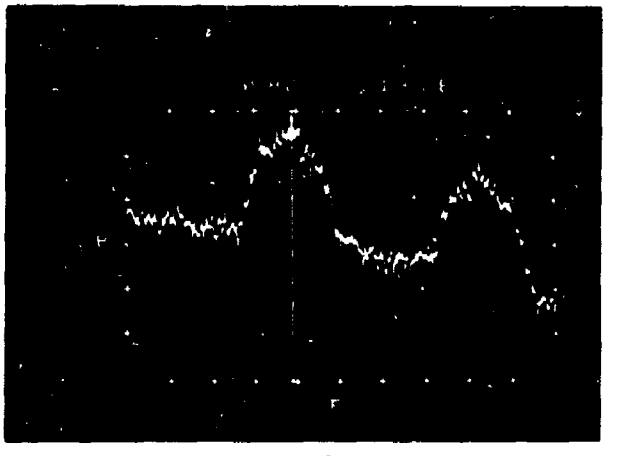

34 NAUTICAL MILES

Photo 36

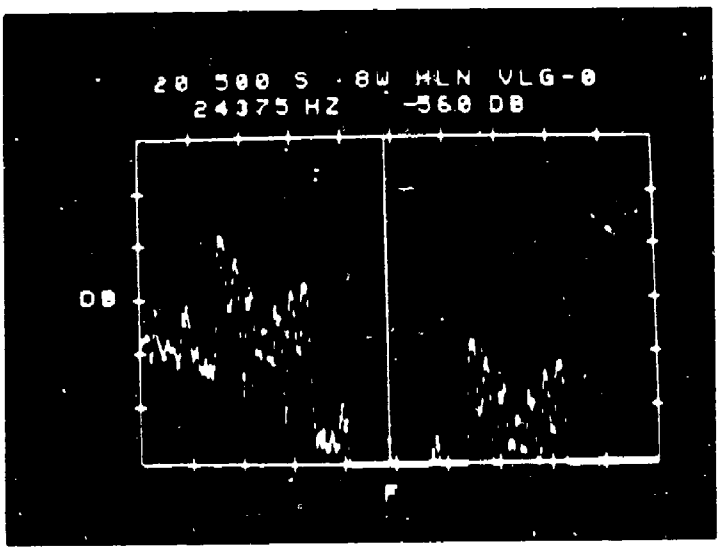

Photo 37

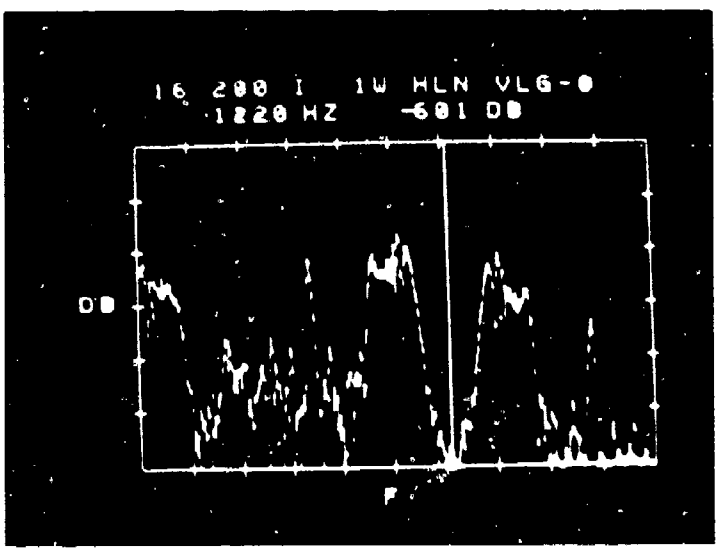

WEATHER

SITE	PRF	NO. OF FALSE ALARMS	CATEGORY	WEATHER CONDITIONS	MAX RANGE	ATTENUATION TO CLEAR SCOPE
Fort Yukon	360	over 1000	DOT ANGELS	Clear Lt Breeze	50 NM	20 dB
Indian Mt	365	< 100	DOT ANGELS	Hazy No precipitation	50 NM	10 dB
Tatalina	350	< 10	DOT ANGELS	Clear Windy	50 NM	5 dB
Cape Newenham	241	< 20 (land) over 1000	DOT ANGELS Sea Clutter	Clear Windy	50 NM 50 NM*	35 dB 35 dB
Cold Bay	244	over 1000	Weather Sea Clutter DOT ANGELS	Rainy	80 NM	75 dB

*False Alarms to 150 NM were noted due to anomalous propagation. The position of the false alarms could often be correlated to mountains or islands.

TABLE VI: False Alarms Recorded in the 3-Pulse MTI Output of FPS-93A Search Radar (Horizontal Polarization)

Photos 38 thru 55 show the spectra of the two angel categories measured. The angels in one category are called dot or point angels because they occupy only one range cell and resemble small targets.

The dot angels were observed to have the following characteristics:

a. Direct measurement of the amplitudes of the dot angels was not possible due to ground clutter. The attenuation required to clear the MTI channel PPI display of all dot angels is given in Table VI. Analysis of spectral photos of some of the returns reveal signal-to-noise ratios up to 30 dB in a 200 KHz video bandwidth.

b. Distributions of measured doppler velocity typically ranged between $\pm$ 25 knots. The highest doppler measured was 42 knots. The spectrum of dot angels always resolved to one or more approximations to line spectrum at some time during the period of observation.

Attempts to associate the dot angels with visual observations of targets were unsuccessful. However, areas with many radar angels per scan were also areas with large bird populations. Therefore, it would not be unreasonable to assume the angel cross-sections to be that of birds, such as ducks, geese, hawks, and sea gulls.

The other category of angels is called distributed angels because they usually occupied more than one range cell. These angels were identified by the following characteristics:

(1) They occur night or day.

(2) They do not seem to move radially or azimuthally over periods of several minutes but have wide noise-like doppler spectra.

(3) The signal strength fluctuated several dB over a period of minutes but usually was very weak. Two exceptions are shown in Photos 48 thru 55.

(4) They occurred during clear weather.

(5) No obvious explanation was evident. However, clear air turbulence, aurora, and covies of birds or insects are possible candidates.

(6) Less than 1% of the angels observed were classified under the category of distributed angels.

Other false alarms noted during the study were those due to anomalous propagation. These returns were correlated with mountains or islands up to 150 NM away but had post-MTI signal-to-noise ratios of over 30 dB. Unfortunately, the anomalous propagation conditions did not occur during the spectral analysis intervals and therefore no spectral data could be taken.

Photo 38

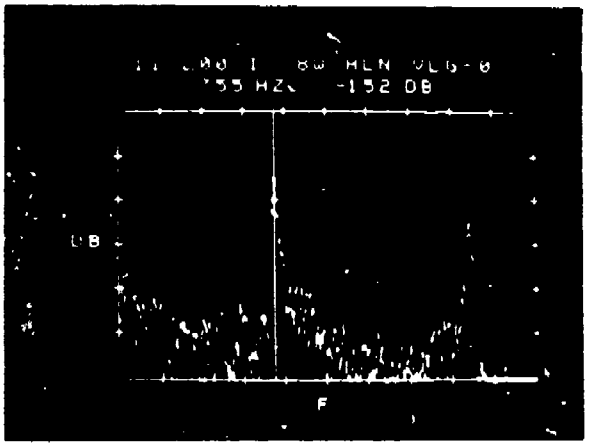

DOT ANGEL (INSTANTANEOUS SPECTRUM)

Photo 39

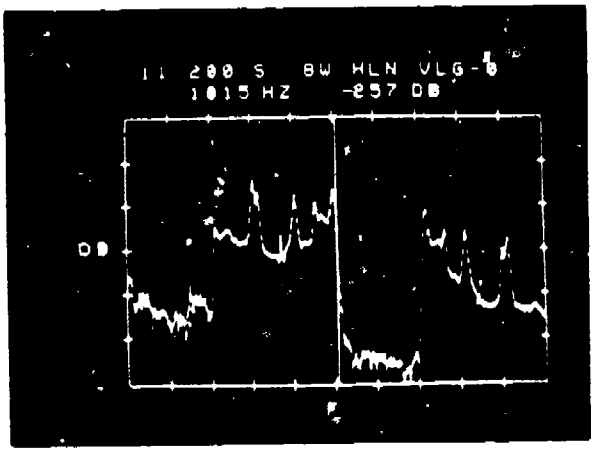

DOT ANGEL (AVERAGE OF 8 SPECTRA)

Photo 40

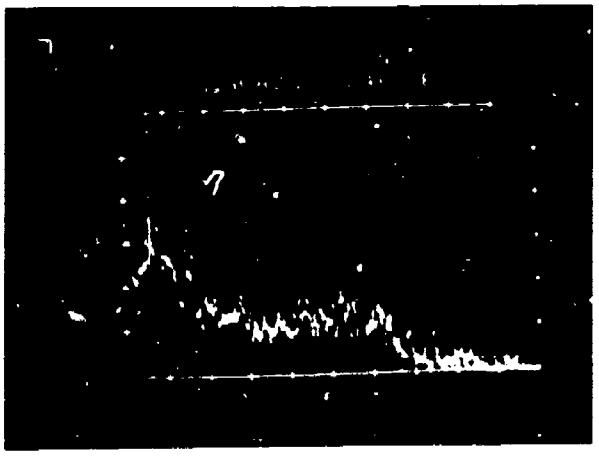

DISTRIBUTED ANGEL

Photo 41

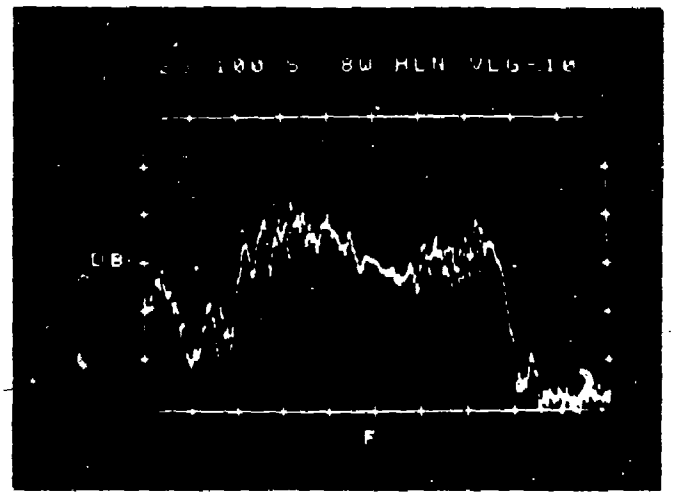

Photo 42

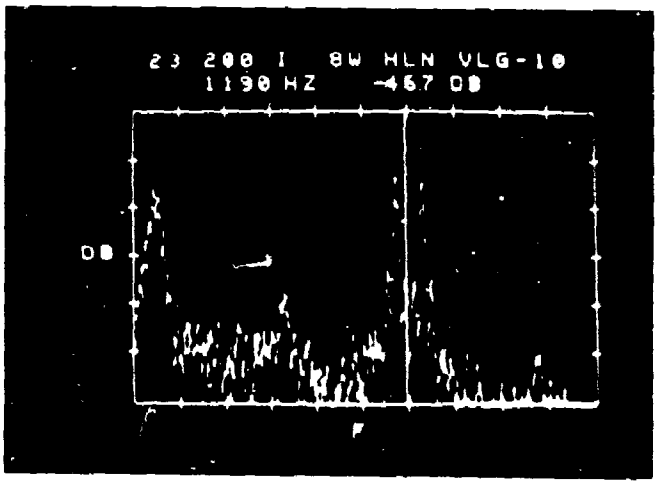

DOT ANGELS

Photo 43

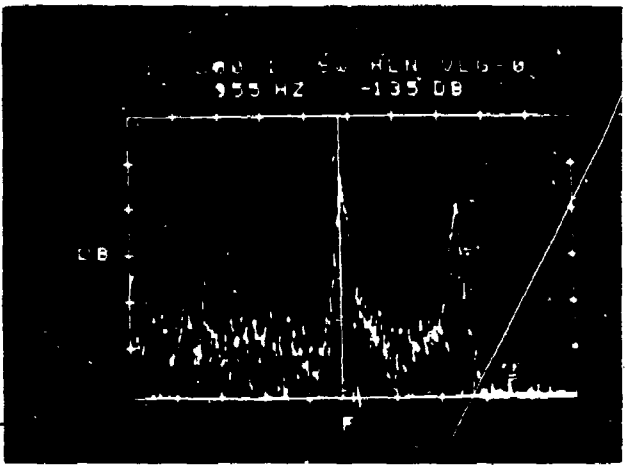

Photo 44

Photo 45

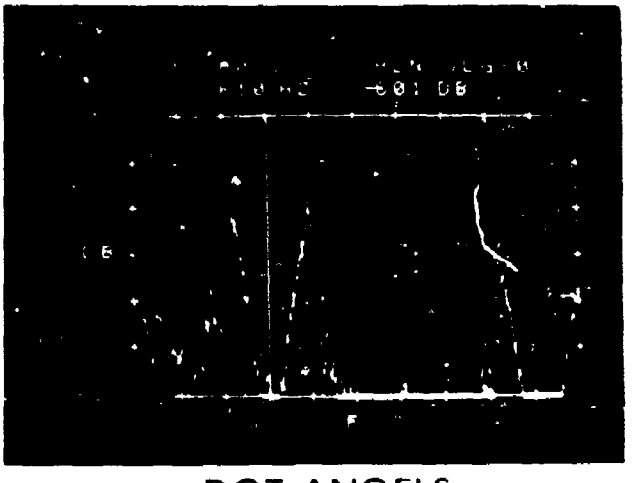

DOT ANGELS

Photo 46

Photo 47

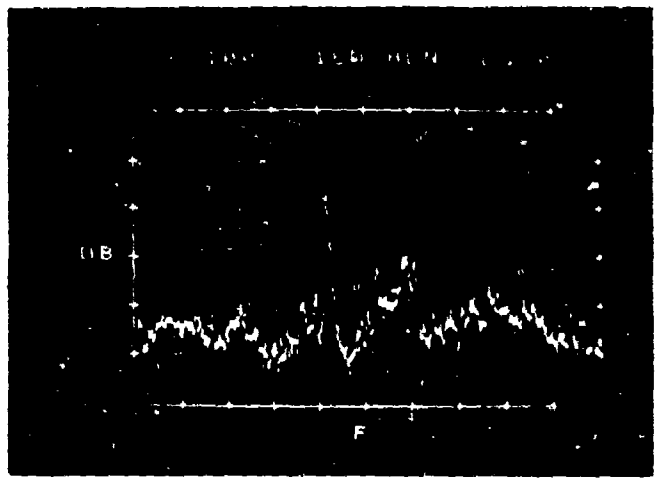

DOT ANGELS

Photo 48

Photo 49

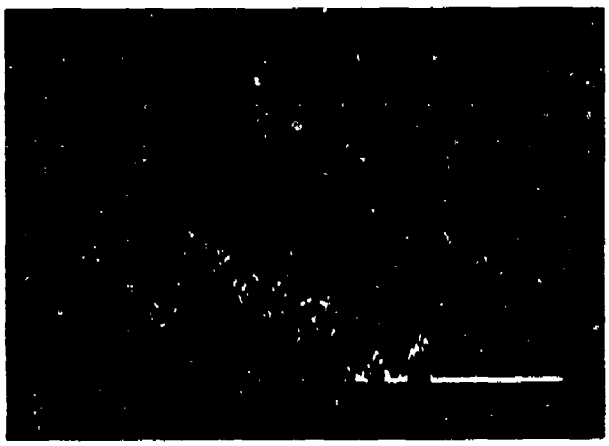

DISTRIBUTED ANGELS

Photo 50

Photo 51

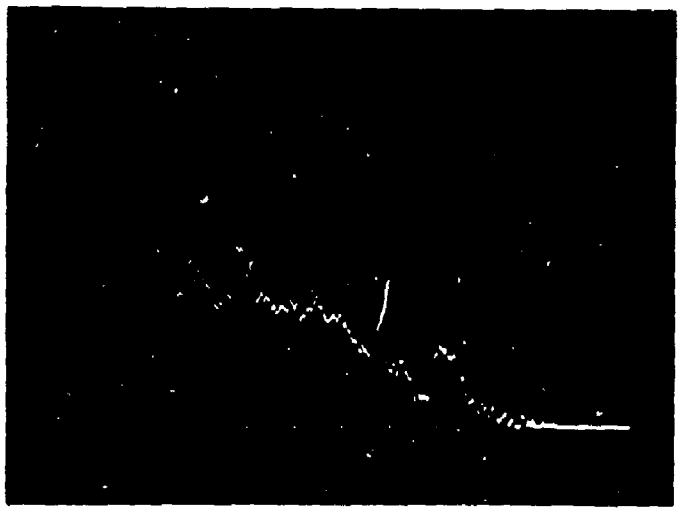

DISTRIBUTED ANGELS

Photo 52

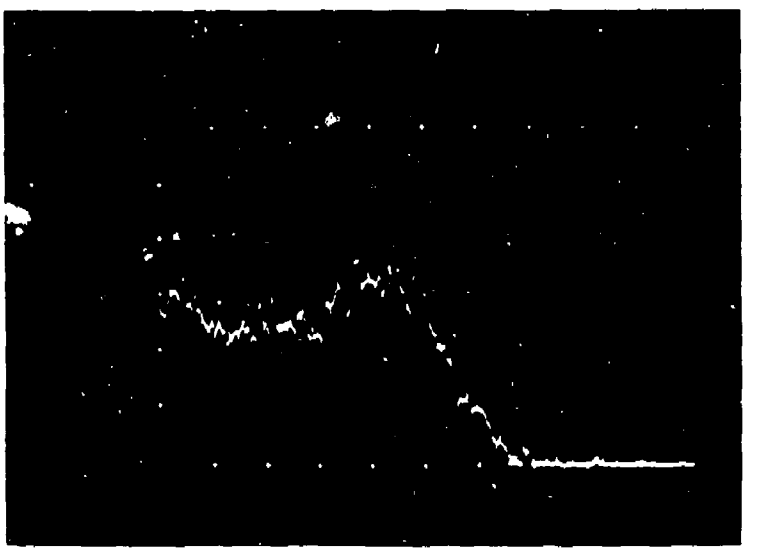

Photo 53

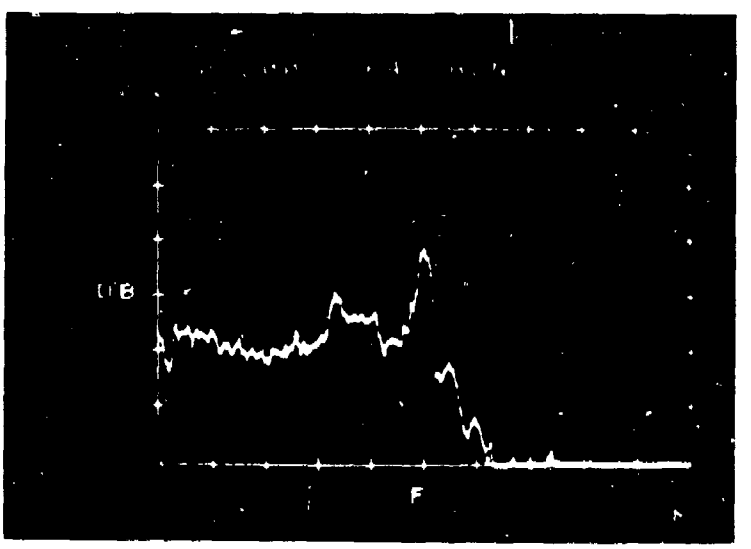

DISTRIBUTED ANGELS

Photo 54

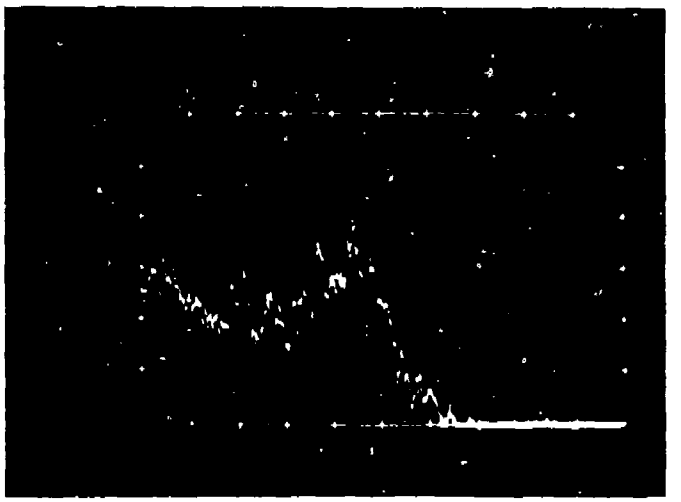

Photo 55

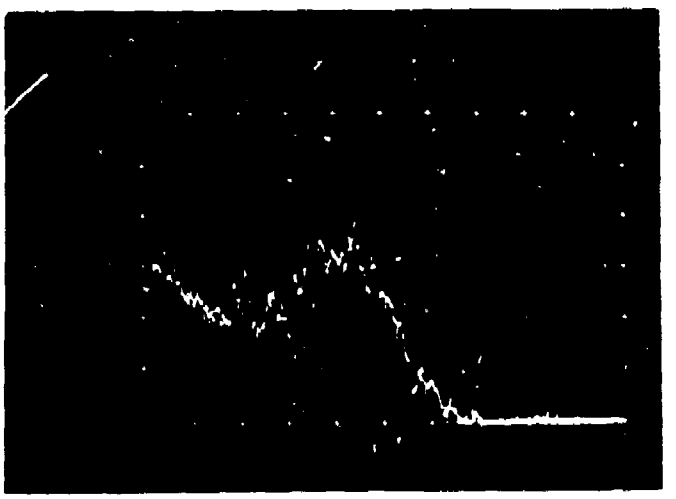

DISTRIBUTED ANGELS

VI. SUMMARY AND CONCLUSIONS:

Clutter measurements of the Alaskan radar environment have been presented in terms of several amplitude cumulative distributions of land and sea clutter effective reflectivity coefficient (σ'_o) and the power spectral density of land, sea, weather and angel clutter. Models have been given for L-Band land clutter for use in radar design.

The discussion on land clutter data presents the following conclusions:

1. Homogeneous clutter whose scatterers are larger than a carrier wavelength and much less than a resolution cell has log-normally distributed reflectivity coefficient. The smaller the grazing angle the larger the spread between the 50 and the 84 percentile.

2. The more heterogeneous the data becomes, where large areas within a sector become shadowed and large exposed areas become prominent, the distribution becomes more like a contaminated-normal with very irregular knees and bends.

3. As the areas of shadowing and exposure become numerous by observing larger and larger sectors, the distribution takes on a smooth transition from a small slope at the 50 percentile to a large slope at the low percentiles.

4. The tails of all distributions approach a log-normal function at the low percentiles.

Measurements of land clutter spectra have shown that the Gaussian function often used in radar design does not adequately describe the high frequency tails of the measured spectral distribution function. A more accurate description is provided by the functions

$$G(f) = \frac{1}{1 + \left(\frac{f}{f_c}\right)^N}$$

where N is typically between 3 and 5 and f_c represents the -3 dB point of the AC curve. The AC -3 dB spectral widths f_c and DC-to-AC ratios (a^2) of terrain clutter returns ranged from $f_c < .25$ Hz and $a^2 = 27$ for mountains to $f_c = 3$ Hz and $a^2 < 1$ for valleys.

The worst case measured sea clutter spectra displayed nearly Gaussian shaped spectral widths close to what is presented in the literature, but much higher mean doppler than locally measured - wind conditions would have inferred. Also, a high mean doppler, narrow spectral component was observed beyond 20 NM and is presumed to be from ocean swells.

The measured weather spectra displayed means of up to at least the unambiguous velocity of the measurement radar (28 knots) and various spectral shapes bounded by the design values given in standard radar texts.

Finally, the false alarms occurring through the MTI channel at each site were presented. Most of the false alarms not caused by weather, sea clutter, land clutter, or noise, were termed angels and were attributed to birds.

VII. REFERENCES:

1. George, S. F., "The Detection of Non-fluctuating Targets In Log Normal Clutter", NRL Report 6796, 1 October 1968.

2. Trunk, G. V. and George, S. F., "Detection of Targets In Non-Gaussian Sea Clutter", IEEE Trans. Aerospace Electronic Systems, Vol AES-6, No. 5, pp 620 - 628, September 1970.

3. Trunk, G. V., "Noncoherent Detection of Nonfluctuating Targets In Contaminated-Normal Clutter", NRL Report 6858, March 21, 1969.

4. Nathanson, Fred E., "Radar Design Principles", Section 7 - 9, 7 - 10; McGraw-Hill, 1969.

5. Fishbein, W., "Clutter Attenuation Analysis", U. S. Army Electronics Command, Technical Report ECOM-2808, March 1967.

6. Pidgeon, V. W., "The Doppler Dependence of Radar Sea Return", J. Geophys. Res., February 15, 1968.

7. Nathanson, F. E., "Radar Design Principles", McGraw-Hill Book Co., Inc., New York, NY 1969.

APPENDIX A

DERIVATION OF REFERENCE THRESHOLDS FOR σ'_c AND σ'_o:

The reference thresholds for the effective radar cross-section σ'_c and the effective normalized radar cross-section σ'_o were derived from the standard radar range equation and the parameters of the calibrated threshold comparator used.

The effective radar cross-section can be defined as:

$$\sigma'_c = P_r R^4 \left[\frac{L_s}{P_t G_t G_r \lambda^2} \right] (4\pi)^3 \qquad \text{(A-1)}$$

$$= \left[\frac{S_r \, L_{ATTN}}{G_{RC}} \right] \left[T^4 \right] \left[\frac{L_s}{P_t G_t G_r \lambda^2} \right] \left[\left(\frac{C}{2} \right)^4 (4\pi)^3 \right]$$

$$\sigma'_c \text{ dBm}^2 = S_r \text{ dBw} + 40 \text{ Log } T - 10 \text{ Log} \left[\frac{P_t G_t G_r \lambda^2}{L_s} \right]$$

$$+ 10 \text{ Log} \left[\left(\frac{C}{2} \right)^4 (4\pi)^3 \right] + L_{ATTN} - G_{rc}$$

$$10 \text{ Log} \left[\left(\frac{C}{2} \right)^4 (4\pi)^3 \right] = 360$$

$$S_{r_{dBw}} = S_{r_{dBm}} - 30 \text{ dB}$$

$$\sigma'_{c_{dBm^2}} = S_{r_{dBm}} + 40 \text{ Log } T - 10 \text{ Log} \left[\frac{P_t G_t G_r \lambda^2}{L_s} \right] \qquad \text{(A-2)}$$

$$+ \quad 330 - G_{rc} + L_{ATTN}$$

The threshold varies as a function of time such that

$$S_{r_{dBm}}(R) + 40 \text{ Log } T = \text{Constant} = K$$

$S_{r_{dBm}}(R)$ = return from a constant radar cross-section as a function of range.

Let reference T_{10} and $S_r(10)$ be given as

$$T_{10} = 124 \ \mu\text{sec}$$

$$S_r(10) = -5 \text{ dBm}$$

therefore

$$K = -5 + 40 \text{ Log } (1.24 \times 10^{-4}) = -5 \quad -156.3 = -161.3 \text{ dB(m-sec}^4\text{)}$$

then

$$\sigma'_{c_{dBm^2}} = K - 10 \text{ Log } \left[\frac{P_t G_t G_r \lambda^2}{L_s} \right] + 330 - G_{rc} + L_{ATTN} \qquad \text{(A-3)}$$

$$= 168.7 - 10 \text{ Log } \left[\frac{P_t G_t G_r \lambda^2}{L_s} \right] - G_{rc} + L_{ATTN}$$

Therefore, the reference threshold is given as

$$\sigma'_{c_{ref}} = 168.7 - 10 \text{ Log } \left[\frac{P_t G_t G_r \lambda^2}{L_s} \right] - G_{rc} \ (\text{dBm}^2) \qquad \text{(A-4)}$$

$(L_{ATTN} = 0 \text{ dB})$

Similarly, the reference threshold for the effective normalized radar cross-section can be defined as

$$\sigma'_o = Pr\ R^3 \left[\frac{L_s}{P_t G_t G_r \lambda^2}\right]\left[\frac{(4\pi)^3\ \sqrt{2}}{\left(\frac{C}{2}\right)\tau\ \text{Sin}\ \theta_\beta\ \text{Sec}\ \phi_g}\right] \qquad \text{(A-5)}$$

$$= \left[\frac{S_r L_{ATTN}}{G_{rc}}\right]\left[T^3\right]\left[\frac{L_s}{P_t G_t G_r \lambda^2}\right]\left[\frac{\left(\frac{C}{2}\right)^2 (4\pi)^3\ \sqrt{2}}{\text{Sec}\ \phi_g}\right]\left[\frac{1}{\tau}\right]\left[\frac{1}{\text{Sin}\ \theta_\beta}\right]$$

$$\sigma'_{odB} = S_{rdBw} + 30\ \text{Log}\ T - 10\ \text{Log}\left[\frac{P_t G_t G_r \lambda^2}{L_s}\right] + 10\text{Log}\left[\frac{\left(\frac{C}{2}\right)^2 (4\pi)^3\ \sqrt{2}}{\text{Sec}\ \phi_g}\right]$$

$$- 10\ \text{Log}\ \tau - 10\ \text{Log Sin}\ \theta_\beta + L_{ATTN} - G_{rc}$$

$$\text{Sec}\ \phi_g \approx 1\ ; \qquad S_{rdBw} = S_{rdBm} - 30$$

$$10\ \text{Log}\left[\frac{\left(\frac{C}{2}\right)^2 (4\pi)^3\ \sqrt{2}}{\text{Sec}\ \phi_g}\right] = +198$$

$$\sigma'_{odB} = S_{rdBm} + 30\ \text{Log}\ T - 10\ \text{Log}\left[\frac{P_t G_t G_r \lambda^2}{L_s}\right] + 168 - 10\ \text{Log}\ \tau \qquad \text{(A-6)}$$

$$- 10\ \text{Log Sin}\ \theta_\beta + L_{ATTN} - G_{rc}$$

The threshold varies as a function of time such that

$$S_{r_{dBm}}(R) + 30 \text{ Log } T = \text{constant} = C$$

where

$S_{r_{dBm}}(R)$ = return from a constant reflectivity as a function of range.

Let references T_{10} and $S_r(10)$ be given as

$$T_{10} = 124 \text{ usec}$$

$$S_r(10) = -15 \text{ dBm}$$

$$C = -15 - 30 \text{ Log}(1.24 \times 10^{-4}) = -15 - 117.2$$

$$= -132.2 \text{ dBm - sec}^3$$

$$\sigma'_{odB} = C - 10 \text{ Log} \left[\frac{P_t G_t G_r \lambda^2}{L_s} \right] + 168 - 10 \text{ Log } \tau - 10 \text{ Log Sin } \theta_\beta \quad \text{(A-7)}$$

$$+ L_{ATTN} - G_{rc}$$

Therefore, the reference threshold is given as

$$\sigma'_{o_{ref}} = 35.8 - 10 \text{ Log} \left[\frac{P_t G_t G_r \lambda^2}{L_s} \right] - 10 \text{ Log } \tau \quad \text{(A-8)}$$

$$- 10 \text{ Log Sin } \theta_\beta - G_{rc} \text{ (dB)}$$

($L_{ATTN} = 0$)

APPENDIX B

I. ERROR ANALYSIS OF MEASUREMENTS:

A. Amplitude Measurements:

The accuracy of the method described depends upon the accuracy to which the radar parameters can be measured or estimated and the extent to which the assumption of the receiver linearity holds true[a].

The assumed accuracy of the radar parameter measurements are given in Table B-I. The receiver gain error is given as .5 dB rms. This was found to be a good approximation up to the 1 dB compression point of the receivers at each site. The dynamic range of the receivers at three of the sites are given in Figure B-1. The other two sites had modifications which allowed attenuation to be placed prior to the first active device, eliminating any dynamic range problems. An approximate relationship between the 1 dB compression point, σ_o' max, and range was used to determine the areas where valid data could be obtained[b].

[a]Due to time and operational restrictions, the use of a calibrated target was not feasible. Therefore, the radar range equation was assumed to exactly describe the measurement problem.

[b]Despite the care taken at each site, a few measurements had returns exceeding the one (1) dB compression point of the receiver. Listed in Tables B-IV - B-VII are the calculated maximum values of effective radar cross-section or normalized radar cross-section (σ_{max}) for which the error analysis applies. Also listed is the region in the tails of the plotted distribution (% min) corresponding to this σ_{max}. Beyond this value, the error increases due to compression and the tails become distorted.

TABLE B-I

Accuracy of Radar Parameter Measurements

PARAMETER	RMS ERROR	RMS ERROR (dB) (E)	ASSUMED ERROR DISTRIBUTION
Average Power (P_{avg})	---	.5 dB	Log Normal
Pulse Width (τ)	.05	.22 dB	----------
Pulse Repetition Rate ($\overline{PRF}$)	.5 Hz	.01 dB max	----------
Wavelength (λ)	.001λ	.004 dB	----------
Transmitter RF Loss (L_t)	---	.5 dB	Log Normal
Receiver RF Loss (L_R)	---	.5 dB	Log Normal
Propagation Loss (L_p)	---	Variable	----------
Radome Loss (L_{RA})	---	.5 dB	Log Normal
$Sin\Theta_\beta$	.001	.18 dB	----------
Threshold Constants			
a. R^4 Threshold (K)	---	Variable	----------
b. R^3 Threshold (C)	---	Variable	----------
Receiver Gain (G_{RC})	---	.5 dB	Log Normal
Attenuator Pad Loss (L_{ATTN})	---	.1 dB	Log Normal
Antenna Gain (G_t, G_r)	---	Variable	Log Normal

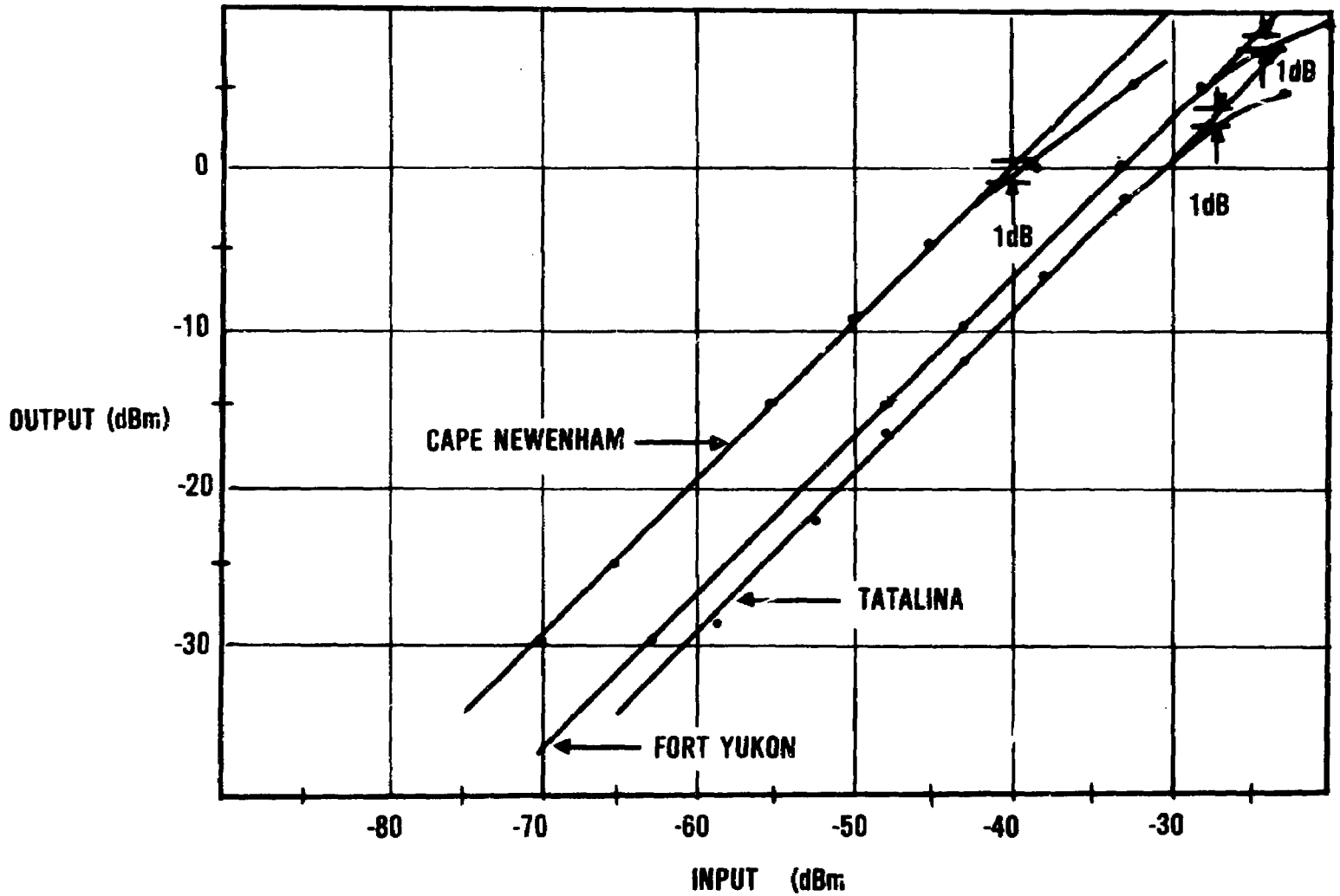

FIGURE B-1: L-Band Mixer - Preamplifier Dynamic Range

The antenna electrical tilt angle at each site could not be changed due to operational considerations. Therefore, a curve of the measured antenna gain function in the vertical plane provided by the antenna manufacturer had to be used (Figure B-2). For the purposes of this exercise, Figure B-2 was assumed to exactly describe the antenna at each of the sites. From the vertical cuts of the horizontal pattern, the azimuthal beamwidth was found to be $1.35° \pm .05$. Therefore, $\text{Sin } \theta_\beta = .024 \pm .001$. If the electrical tilt angle of the antenna and the depression angle of the ray directed toward a clutter patch were known, the antenna gain could be read off the curve. The tilt angles were measured within the tolerance given in Tables B-IV thru B-VIII. The depression angle toward a clutter area can be found by

$$\alpha = \text{Sin}^{-1}\left[\frac{-(h_2^2 - h_1^2)}{2R\left(\frac{4}{3}\right)r_e} - \frac{(h_2 - h_1)}{R} + \frac{R}{\left(\frac{8}{3}\right)r_e}\right]$$

where h_2 = height of clutter area (ft)

h_1 = height of radar (ft)

R = range to clutter area (ft)

r_e = true radius of earth (ft)

The $\frac{4}{3}$ earth-radius approximation to the effects of standard refraction was assumed in the derivation of the above equation.

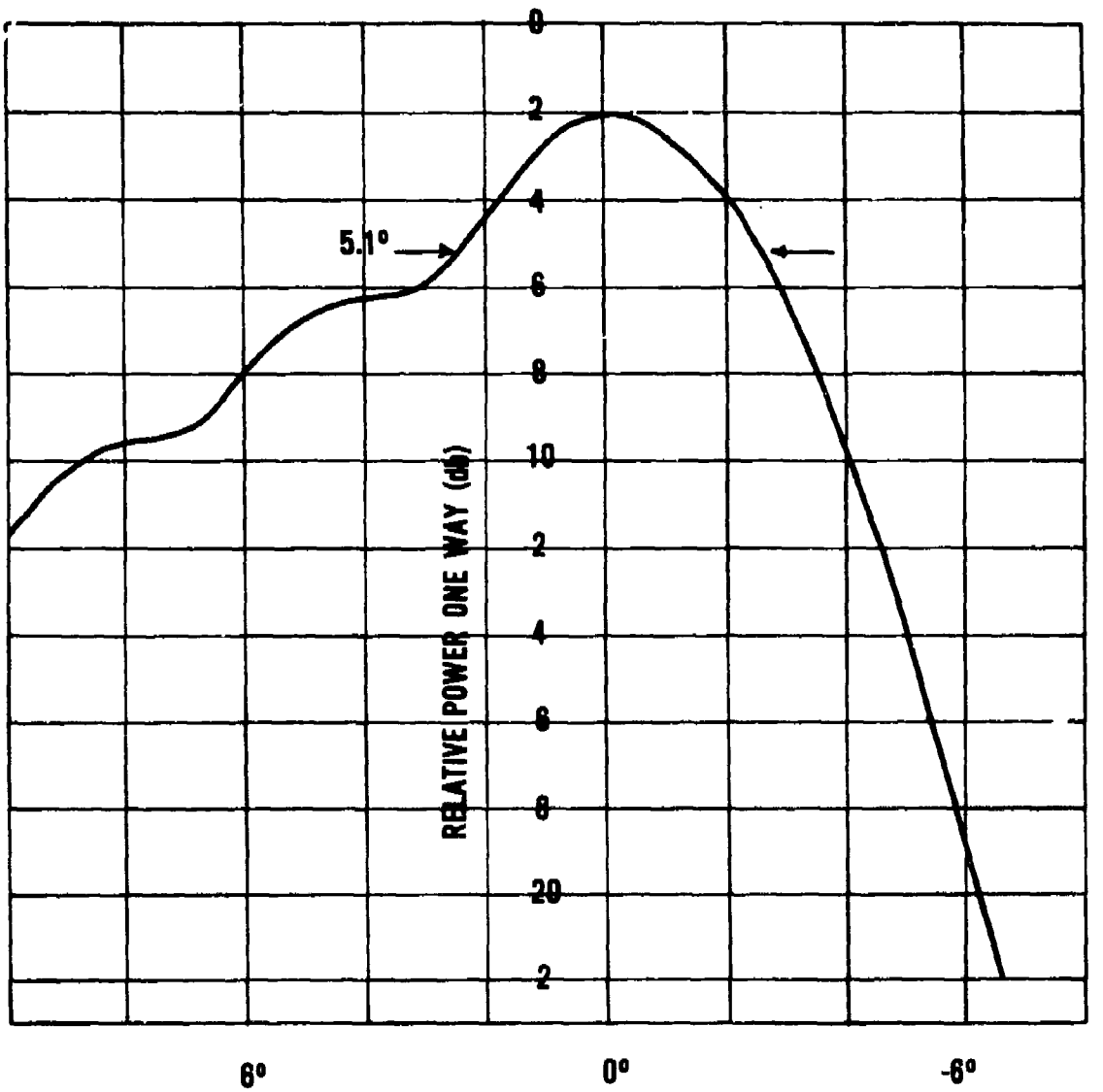

FIGURE B-2: FPS-93 Antenna Pattern Principal Plane Elevation Horizontal Polarization 1300 MHz

Since most areas measured have a range and height extent, minimum and maximum depression angles were determined for each area. After conversion to gain through the use of Figure B-2, an average gain (G), maximum error (Epk), and RMS error (E_{RMS}) (assuming log normal distribution) was associated with each (E_{RMS}) measurement. For convenience, Epk $\triangleq 2\sigma = 2\ E_{RMS}$. The total antenna RMS gain error was determined by

$$E_G = [\ E^2_{RMS} + g^2\ (\text{Tilt Angle})\ ]^{\frac{1}{2}}$$

where g^2 (Tilt Angle) = Squared Error in Gain due to Tilt Error

$$\approx [\ 3.8\ (\text{Tilt Error})\ ]^2$$

The propagation loss error is determined by the range extent of the clutter area being measured and can be found from Figure B-3.

The threshold error was defined as the RMS deviation from the desired constant. The measured error versus range is given in Tables B-II and B-III for the σ_C° threshold and σ_O° threshold, respectively. As one can see, the mean error, which was included into the calculation of reference parameter for each measurement, and the standard deviation of the error about the mean depend on the range and range extent of the clutter area. These are listed for each measurement in Tables B-IV thru B-VIII.

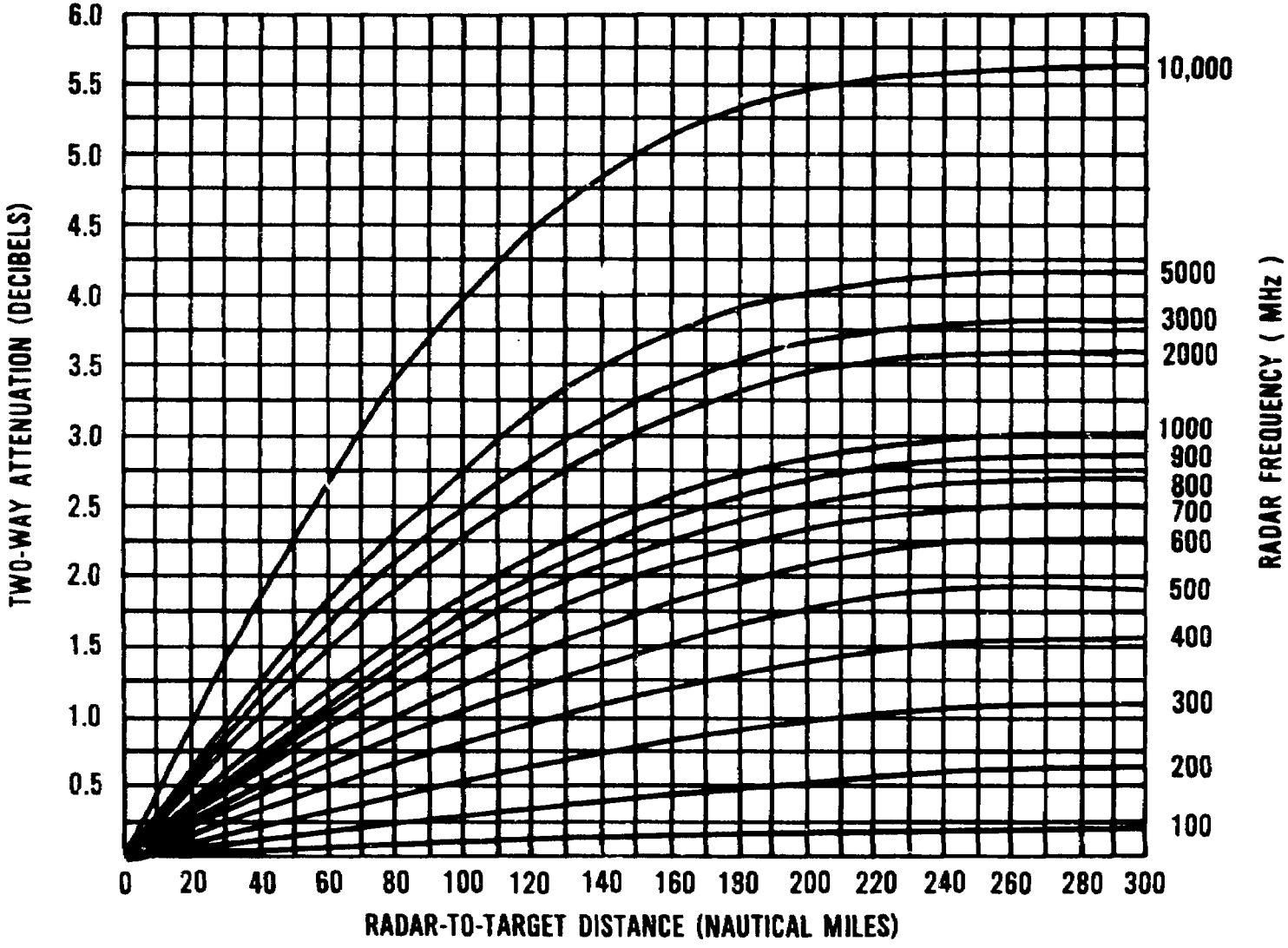

FIGURE B-3: Absorption Loss For Two Way (Radar) Propagation at Zero Elevation Angle (From Blake, L.V.)

Since it is unlikely that all the errors will add linearly, an RMS value was considered more representative. The RMS error of the absolute value for the σ°_{c} and σ°_{o} calculations can be derived from equations (A-3) and (A-7), respectively.

$$E^2_{\sigma^{\circ}_c} = E^2_K + E^2_{P_{AVG}} + E^2_\tau + E^2_{\overline{PRF}} + 4E^2_G + 4E^2_\lambda + E^2_{L_p} + E^2_{G_{rc}}$$
$$+ E^2_{L_{ATTN}} + E^2_{L_t} + E^2_{L_r} + E^2_{L_{RA}}$$

$$E^2_{\sigma^{\circ}_o} = E^2_C + E^2_{P_{AVG}} + E^2_{\overline{PRF}} + 4E^2_G + 4E^2_\lambda + E^2_{L_p} + E^2_{\sin\theta_\beta}$$
$$+ E^2_{L_{ATTN}} + E^2_{G_{RC}} + E^2_{L_t} + E^2_{L_R} + E^2_{L_{RA}}$$

where E = standard deviation in dB

$P_t = P_{AVG} - \tau_{dB_{sec}} - \overline{PRF}_{dBHz}$

$L_S = L_p L_R L_t L_{RA}$

Substituting the values given in Table B-I, the mean squared errors are

$$E^2_{\sigma^{\circ}_c} = 1.3 + E^2_K + 4E^2_G + E^2_{L_p}$$

$$E^2_{\sigma^{\circ}_o} = 1.3 + E^2_C + 4E^2_G + E^2_{L_p}$$

These values for each measurement are given in Tables B-IV thru B-VIII.

TABLE B-II

$\sigma_{\hat{c}}$ Threshold Error

Sr (dBm)	Tcal (usec)	Tmeas (usec)	∂ TdBsec (dB)	∂ K (dB)
- 5.0	123.5	145.7	.72	2.87
-12.0	185.25	197.0	.27	1.07
-17.0	247.0	247.0	0	0
-24.1	370.5	361.5	-.11	-.43
-29.1	494.0	476.1	-.16	-.64
-33.0	617.5	596.6	-.15	-.60
-36.1	741.0	716.1	-.15	-.59
-38.8	864.5	835.6	-.15	-.59
-41.1	998.0	958.1	-.13	-.53
-43.2	1111.5	1094.0	-.07	-.28
-45.0	1235.0	1229.0	-.02	-.08
-52.0	1852.5	1906.0	+.12	+.50
-57.0	2470.0	2581.0	+.19	+.76

TABLE B-III

$\sigma_{\tilde{o}}$ Threshold Error

Sr (dBm)	T cal (usec)	T meas (usec)	∂ TdBsec (dB)	∂ C (dB)
-15.0	123.5	144.5	+.68	2.05
-20.3	185.25	200.8	+.35	1.05
-24.0	247.0	241.7	-.09	-.28
-29.3	370.5	354.1	-.0	-.59
-33.1	494.0	464.1	-.27	-.81
-36.0	617.5	581.7	-.26	-.78
-38.3	741.0	701.1	-.24	-.72
-40.4	864.5	824.6	-.21	-.62
-42.1	988.0	936.3	-.23	-.70
-43.6	1111.5	1074.0	-.15	-.45
-45.0	1235.0	1221.0	-.05	-.15
-50.3	1852.5	1938.0	+.20	+.59
-54.0	2470.0	2549.0	+.14	+.41

TABLE B-IV: Measurement Errors - Fort Yukon

TILT* = ± .13°

G(TILT)AVG = .5

MEASUREMENT	E (2σ)	E_{RMS}	E_G	$E_{c(K)}$	E_{L_P}	E_{σ_c}	E_{σ_o}	τ	σ_{max}	ϕ_{min}
1	0	0	.5	.7	.1	--	1.7	6.2	-13	0
2	0	0	.5	.7	.1	--	1.7	3.0	-10	0
3	0	0	.5	.7	.1	--	1.7	1.0	- 3	0
4	0	0	.5	.7	.1	--	1.7	.5	- 2	0
5	.2	.1	.51	0	.1	--	1.5	3.0	+ 9	0
6	.2	.1	.51	0	.1	--	1.5	1.0	+13	0
7	.2	.1	.51	0	.1	--	1.5	.5	+16	0
8	.2	.1	.51	0	.1	--	1.5	6.2	+ 6	0
9	.3	.15	.52	.1	.1	--	1.5	6.2	+ 4	0
10	.3	.15	.52	.1	.1	--	1.5	6.2	+ 4	0
11	.3	.15	.52	0	0	--	1.5	6.2	+ 2	0
12	.3	.15	.52	0	0	--	1.5	6.2	+ 3	0
13	.2	.1	.51	0	.1	--	1.5	6.2	+ 6	0
14	0	0	.5	.6	.1	1.6	--	6.2	+44	0

*Error in Tilt Angle Measurement

TABLE B-V: Measurement Errors - Indian Mt.

TILT* = ± .2°

G (TILT) AVG = .76

MEASUREMENT	E (2σ)	E_{RMS}	E_G	$E_{c(K)}$	E_{L_P}	E_{σ_c}	E_{σ_o}	τ	σ_{max}	$\$_{min}$
1	3.5	1.75	1.9	.55	1.2	4.2	--	6.1	--	--
2	.65	.33	.8	0	.1	--	2.0	6.1	--	--
3	.5	.25	.8	.54	.3	--	2.1	6.1	--	--
4	.8	.4	.9	.24	.3	--	2.2	6.1	--	--
5	.8	.4	.9	.24	.3	--	2.2	3.0	--	--
6	.8	.4	.9	.24	.3	--	2.2	1.0	--	--
7	.8	.4	.9	.24	.3	--	2.2	.6	--	--
8	.8	.4	.9	0	.1	--	2.1	6.1	--	--
9	.8	.4	.9	.24	.3	--	2.2	6.1	--	--
10	.8	.4	.9	.24	.3	--	2.2	3.0	--	--
11	.8	.4	.9	.1	.1	--	2.1	3.0	--	--

*Error in Tilt Angle Measurement

TABLE B-VI: Measurement Errors - Tatalina

TILT* = ± .21°

G (TILT) AVG = .8

MEASUREMENT	E (2σ)	E_{RMS}	E_G	$E_{C(K)}$	E_{Lp}	E_{σ_c}	E_{σ_o}	τ	σ_{max}	$\dot{\theta}_{min}$
1	3.5	1.8	2.0	.55	1.	4.4	--	6.	+51	.3
2	2.5	1.3	1.5	.7	.4	3.3	--	6.	+50	0
3	2.5	1.3	1.5	.55	.8	---	3.4	6.	- 7	.2
4	2.5	1.3	1.8	.8	.4	---	3.3	6.	- 7	.4
5	2.5	1.3	1.5	.55	.8	---	3.4	3.	- 4	0
6	2.5	1.3	1.5	.55	.8	---	3.4	1.	+ 1	0
7	2.5	1.3	1.5	.55	.8	---	3.4	.5	+ 4	0
8	2.5	1.3	1.5	.5	.8	---	--	.5	+51	0
9	2.5	1.3	1.5	.5	.8	3.4	--	1.	+51	0
10	2.5	1.3	1.5	.5	.8	3.4	--	3.	+51	.5
11	2.5	1.3	1.5	.5	.8	3.4	--	6.	+51	1.
12	1.4	.7	1.1	.2	.1	3.4	2.5	6.	- 5	.2
13	1.3	.7	1.1	.2	.3	---	2.5	6.	+ 2	0
14	2.3	1.2	1.4	.5	.1	---	3.1	6.	+14	0

*Error in Tilt Angle Measurement

TABLE B-VI: Measurement Errors - Tatalina (Continued)

TILT* = ± .21°

G (TILT) AVG = .8

MEASUREMENT	E (2σ)	E_{RMS}	E_G	$E_{C(K)}$	E_{L_p}	E_{σ_c}	E_{σ_o}	τ	σ_{max}	σ_{min}
15	.8	.4	.9	.1	0	---	2.1	6.	+ 6	0
16	1.3	.7	1.1	.2	.3	---	2.5	3.	+ 5	0
17	1.4	.7	1.1	.2	.1	---	2.5	3.	- 2	.3
18	.8	.4	.9	.1	0	---	2.1	3.	+ 9	0
19	.8	.4	.9	.1	0	---	2.1	1.	+14	0
20	1.4	.7	1.1	.2	.1	---	2.5	1.	+ 3	0
21	1.3	.7	1.1	.2	.3	---	2.5	1.	+10	0
22	.8	.4	.9	.1	0	---	2.1	6.	+17	0
23	1.3	.7	1.1	.2	.3	---	2.5	.5	+13	0
24	1.4	.7	1.1	.2	.1	---	2.5	.5	+ 6	0
25	2.3	1.2	1.4	.5	.1	---	3.1	.5	+14	0
26	1.4	.7	1.1	.2	.1	---	2.5	6.	- 5	.7
27	1.3	.7	1.1	.2	.3	---	2.5	6.	+ 2	0
28	.8	.4	.9	.1	0	---	2.1	6.	+ 6	0
29	1.0	.5	.9	.3	.3	---	2.2	6.	+12	0

*Error in Tilt Angle Measurement

TABLE B-VII: Measurement Errors - Cape Newenham

TILT* = ± .2° G (TILT) AVG = .8

MEASUREMENT	E (2σ)	E_{RMS}	E_G	$E_{C(K)}$	E_{L_p}	E_{σ_c}	E_{σ_o}	τ	σ_{max}	σ_{min}
1	.8	.4	.9	.5	.8	2.3	---	6.	+27	.15
2	.8	.4	.9	.8	.1	2.3	---	6.	+30	0
3	.5	.3	.9	.3	.1	---	2.2	6.	-20	0
4	.5	.3	.9	.3	.1	---	2.2	3.	-17	0
5	.5	.3	.9	.3	.1	---	2.2	1.	-12	0
6	--	--	--	--	--	---	---	--	- 9	0
7	0	0	.8	.1	.1	---	2.0	6.	-15	0
8	0	0	.8	.1	.1	---	2.0	3.	-12	0
9	--	--	--	--	--	---	---	--	---	--
10	--	--	--	--	--	---	---	--	---	--
11	.6	.3	.9	.1	0	---	2.2	6.	-19	1.5
12	.6	.3	.9	.1	0	---	2.2	3.	-16	.2
13	.6	.3	.9	.1	0	---	2.2	1.	-11	0

*Error in Tilt Angle Measurement

TABLE B-VIII: Measurement Errors - Cold Bay

TILT* = ± .21°

G (TILT) AVG = .8

MEASUREMENT	E (2σ)	E_{RMS}	E_G	$E_{c(K)}$	E_{L_p}	E_{σ_c}	E_{σ_o}	τ	σ_{max}	ϕ_{min}
1	.7	.4	.9	0	0	---	2.1	5.7	---	---
2	1.	.5	.9	.3	.2	---	2.2	5.7	---	---
3	.7	.4	.9	0	0	---	2.1	5.7	---	---
4	1.	.5	.9	.3	.2	---	2.2	5.7	---	---
5	.7	.4	.9	0	0	---	2.1	3.0	---	---
6	1.	.5	.9	.3	.2	---	2.2	3.0	---	---
7	1.	.5	.9	.3	.2	---	2.2	1.0	---	---
8	.7	.4	.9	0	0	---	2.1	1.0	---	---
9	.7	.4	.9	0	0	---	2.1	0.5	---	---

*Error in Tilt Angle Measurements

TABLE B-VIII: Measurement Errors - Cold Bay (Continued)

TILT* = ± .21°

G (TILT) AVG = .8

MEASUREMENT	E (2σ)	E_{RMS}	E_G	$E_{C(K)}$	E_{L_P}	E_{σ_C}	E_{σ_O}	τ	σ_{max}	ϕ_{min}
10	1.	.5	.9	.3	.2	---	2.2	0.5	---	---
11	.7	.4	.9	0	0	---	2.1	5.7	---	---
12	.7	.4	.9	0	0	---	2.1	3.0	---	---
13	.7	.4	.9	0	0	---	2.1	1.0	---	---
14	.7	.4	.9	0	0	---	2.1	0.5	---	---
15	1.	.5	.9	.3	.2	---	2.2	5.7	---	---
16	1.	.5	.9	.3	.2	---	2.2	3.0	---	---
17	1.	.5	.9	.3	.2	---	2.2	1.0	---	---
18	1.	.5	.9	.3	.2	---	2.2	0.5	---	---

*Error In Tilt Angle Measurement

B. Spectral Measurements:

The errors in the spectral measurements were essentially the spectral contamination contributed by the interface equipment and the radar.

The spectral contamination from the interface equipment (excluding the 30 MHz local oscillator) was essentially the amplitude distortion from the $\frac{\sin x}{x}$ weighting of the sample-and-hold circuitry and a low pass filter as shown previously in Figure 9. Distortion measurements were made to determine the regions of linearity in the video circuitry using two equal amplitude audio tones. Harmonic distortion contributed by the spectrum analyzer was immeasurable (better than -74 dB below the amplitude of one tone) for signal levels below A/D converter saturation. The maximum 2nd harmonic distortion within 0 - 300 Hz contributed by the 200 KHz amplifier and sample-and-hold was better than -48 dB below the fundamental for signal inputs of 250 mV pk-pk or less. Third order distortion for this input was better than -55 dB for frequencies below 100 KHz. Most measurements were performed with inputs less than 250 mV pk - pk. The linear limit amplifier and heterodyne detector contributed inter-modulation distortion less than -50 dB for video outputs of 250 mV pk - pk or less. At sites where attenuation could not be placed ahead of the mixer-preamp, only signals at least 15 dB below the 1 dB compression point were analyzed.

It was assumed that signals at this level or below would contribute negligible spectral distortion.

The spectral contamination caused by the transmitter consisted primarily of spurious frequencies and spreading of observed spectra due to oscillator instability. A spectral analysis of the FPS-65 transmitter at Verona Test Site (closed loop) disclosed a random noise component and discrete frequencies. The random noise component was centered about the carrier and was at least 60 dB down from the carrier at .1 Hz and could be ignored. The discrete frequencies with amplitudes above -60 dB were 60 Hz (-50 dB) and a spurious (-58 dB) which was caused by intermodulation of the PRF with 60 Hz. When observing nearby "stable" clutter returns, the spurious frequencies modulated each return providing a method for identifying this form of contamination. For convenience, this was the method used during the Alaskan measurements to determine transmitter spurious frequencies.

The short-term stability of the radar oscillators and timing system was the limiting factor determining the resolution of the spectral analysis. The changes in oscillator phase between transmission and reception from clutter often resulted in a spectral spreading or smearing of several tenths of a Hertz. For instance, a .25 Hz shift was imposed on a return 300 usec away at one site due presumably to the stalo oven cycling. In many cases, however, the spectral spread was less than .05 Hz. Therefore, the resolution of the measurements varied but was less than 1 Hz in all cases.

The spectrum analyzer computes and displays the one-sided energy spectral density of the input waveform. However, it does not display the zero frequency filter. Therefore, an indirect method was used to determine the DC-to-AC power ratio of land clutter. The spectrum analyzer is peak voltage limited and internally relates all spectral amplitudes to this maximum level. By setting the input signal to just below saturation when the coho was in-phase with the return, the scale was calibrated to the maximum peak energy of the heterodyned return. Then, the relative energy in the zero filter was approximated by

$$V_{DC}^2 \cong \left(1 - \int_{\Delta f}^{\infty} |V(f)| df \right)^2$$

This approximation worked well when the DC energy is much greater than the AC energy and the selected filter bandwidth B_f was larger than the spectral spread due to instability.

Finally, the term actually measured by the equipment was average voltage or average energy spectral density over a specific time interval. The measured process would have to be stationary to have a correlation function and, consequently, a power spectrum. Although radar clutter is, in general, a non-stationary process, it can usually be assumed to be stationary over the observation interval of a long range search radar. This allows a stringent stationary clutter model to be constructed for the purpose of comparing different radar designs. Since the purpose of this

study was to obtain data for such a clutter model, the term power spectral density is used throughout the report to describe the measured data as well as the idealized functions.

APPENDIX C

AVERAGE σ_0' AND DEPRESSION ANGLES FOR LAND CLUTTER MEASUREMENTS:

Table C-I lists the average depression angle and the average effective reflectivity coefficient $\overline{\sigma_0'}$ for the measurement areas presented in Section IV. Unless otherwise noted, the 6 usec measurements were used in the calculations.

In order to obtain $\overline{\sigma_0'}$, a histogram approximation to the density function was obtained from the original data of each measurement. All the range cells in the measurement area, including those range cells with immeasurable returns due to the presence of noise, were included in the sample size to obtain the true average value. Since the actual distribution of the immeasurable returns is unknown, two extreme distributions were considered. In the first case, the immeasurable returns were assigned a σ_0' just below the threshold sensitivity of the measurement equipment with a probability of occurrence equal to the percentage of range cells with an immeasurable return. In the second case, the immeasurable returns were assigned a $\sigma_0' = 0$. These cases provide an upper and lower bound to the true average value.

With one exception, the average values calculated in both extreme cases differed by less than .1 dB. The exception was the measurement of the Fort Yukon swamp where a difference of

.5 dB was calculated. Compared with the accuracies of the measurements, these differences are negligible. Therefore, the actual distribution of the immeasurable returns is irrelevant.

TABLE C-I: Average Reflectivity and Depression Angles

SITE	TERRAIN TYPE	AREA CODE	AVERAGE DEPRESSION ANGLE (Deg)	$\overline{\sigma_o'}$ (dB) (τ = 6 usec)
Fort Yukon	Swamp, Muskeg	1	.15	-60
	High Hills, Mtns.	3	0	-37
	Hills	4	0	-24
	Hills	6	0	-17
Indian Mt.	Hills	2	.6	-22
	Hills	3	.6	-14
	Hills	4	.4	-25
	Hills	5	.7	-16
	Mtns.	6	.6	-28
	Mtns.	7	.6	-21(+)
Tatalina	Everything	2	.7	-20
	Everything	3	.7	-23
	Hills	6	.6	-19
	Muskeg, Swamp	7	1.2	-17
	Mtns.	8	.1	-18
	High Hills, Mtns.	9	.3	-19
Cape Newenham	Hills	3	.5	-41
	Hills	5	.6	-32
Cold Bay	Volcanic Mtns.	1	-.8*	-26
	Volcanic Mtns.	2	-.8*	-30

(+) -3 usec pulse width
* -negative depression angle indicates angle above tangent to surface